Branching fraction measurement for the decay $B_s^0 \to \phi\gamma$ and search for the decay $B_s^0 \to \gamma\gamma$ at high energy e^+e^- collisions at $\Upsilon(5S)$ energy

Deepanwita Dutta

A thesis
submitted for the degree of
Doctor of Philosophy

Department of Physics
Indian Institute of Technology Guwahati
Guwahati 781039, India

December 2014


भारतीय प्रौद्योगिकी संस्थान गुवाहाटी
Indian Institute of Technology Guwahati

Branching fraction measurement for the decay $B_s^0 \to \phi\gamma$ and search for the decay $B_s^0 \to \gamma\gamma$ at high energy e^+e^- collisions at $\Upsilon(5\text{S})$ energy

Deepanwita Dutta

A thesis
submitted for the degree of
Doctor of Philosophy

Supervisor:
Dr. Bipul Bhuyan

Department of Physics
Indian Institute of Technology Guwahati
Guwahati 781039, India

December 2014

Dedicated to my beloved parents
Shri. Debasish Dutta and Smt. Aparna Dutta

"Nothing is accidental in the universe - this is one of the laws of physics - except the entire universe itself, which is pure accident, pure divinity."

Joyce Carol Oates

Declaration

The work in this thesis is based on research carried out at the Department of Physics, Indian Institute of Technology Guwahati, India under the supervision of Dr. Bipul Bhuyan. No part of this thesis has been submitted elsewhere for the award of any other degree or qualification. Work presented in this thesis are entirely my own unless referenced to the contrary in the text.

Ms. Deepanwita Dutta

भारतीय प्रौद्योगिकी संस्थान गुवाहाटी
Indian Institute of Technology Guwahati

Certificate

Dr. Bipul Bhuyan
Associate Professor
Department of Physics, IIT Guwahati
Email: bhuyan@iitg.ac.in

It is certified that the work contained in the thesis entitled " **Branching fraction measurement for the decay $B_s^0 \rightarrow \phi\gamma$ and search for the decay $B_s^0 \rightarrow \gamma\gamma$ at high energy e^+e^- collisions at $\Upsilon(5S)$ energy** " by Ms. Deepanwita Dutta, a Ph.D. student of the Department of Physics, IIT Guwahati was carried out under my supervision and has not been submitted elsewhere for award of any degree.

Dr. Bipul Bhuyan

Acknowledgements

I am thankful to my Ph.D. supervisor Dr. Bipul Bhuyan for introducing me to the world of high energy physics. I thank him for his guidance, help and support and for pointing out my drawbacks which helped me to improve myself. I learnt many things from the discussions that we had while presenting the results of our analysis in the collaboration meetings, discussing the implications of the experimental results, responding to the referees and making thesis corrections. I am also thankful to my doctoral committee members Dr. P. Poulose, Dr. P. K. Padmanabhan and Dr. Anupam Saikia for reviewing my progress and for giving me their frank comments and suggestions. I thank Poulose sir for helping me whenever I approached him for any help. I express my gratitude to the other teachers of high energy physics group as I learnt several things from the discussions in the Journal Club meetings. I am thankful to Dr. Saurabh Basu, the HOD of this department for his friendly and approachable behaviour. I am also thankful to all the faculty members and staff of this department for their friendly behaviour and help and especially to Mr. Basab Purkayastha for helping me in computer related issues. I thank Mr. Pallav Dutta and Mr. J. K. Ghosh of computer center for helping me on many occasions. I am thankful to MHRD for providing me the fellowship to carry out this research work.

After realizing that enough computational job has to be done in my research and me being a complete novice at that time, I spent many sleepless nights at the start of my Ph.D. career having full of doubts whether I have taken a right decision in deciding to join the field of experimental high energy physics. I am thankful to Kay Kinoshita, my group convener for supporting me in the initial days of my association with the Belle collaboration. I am also thankful to Jean Wicht who was the co-convener of the $\Upsilon(5S)$ group for helping me during the most difficult phase of my Ph.D. career. This thesis wouldnot have been complete without his help. I express my sincere thanks to Roman Mizuk who became the co-convener of $\Upsilon(5S)$ group after Jean for his valuable comments and suggestions. I thank Karim Trabelsi for his help and guidance during my stay in Japan and Dr. Gagan Mohanty for being helpful and supportive.

I am thankful to my referees Dr. Thomas Kuhr, Dr. Vladimir Savinov and Dr. Yusa Yosuke for reviewing my analysis and for their valuable suggestions which helped me to complete this analysis in time. I thank Dr. Thomas Kuhr for his patient guidance and help on various analysis related issues. I learnt many things from the discussions I had with him. I am also thankful to Belle colleagues Shohei Nishida, Takanori Hara, Nishimura and Michael Prim whom I have emailed several times for help regarding my analysis and to the TMVA developers Peter Speckmayer and Helge Voss for helping me to clear my doubts related to TMVA. My sincere thanks extend to the people responsible for data taking, maintaining the quality of data and computer maintenance for the Belle collaboration. I am also thankful to other members of the $\Upsilon(5S)$ group as well as to the entire Belle collaboration. I am thankful to the Belle secretaries for helping me in official work during my stay in Japan.

I thank all my teachers whose efforts and blessings have helped me to reach here. I am thankful to my fellow research mates Dr. V. Prasad, Satendra, Kamal Dutta, Kamal Nath, Biswajit and others for their friendly behaviour and cooperation. I am thankful to my friends and labmates Manirupa di, Swarnadweep, Souvik, Apurba, Abhijit, Suresh, Onkar and others for creating a pleasant work environment and for helping me throughout my PhD career. I thank my hostel mates Jhuma, Chitralekha, Namita di, Shyni, Poulami, Tribedi, Deepanjali and others for creating a homely atmosphere. We spent many enjoyable moments together which I will always treasure. I will miss the long discussions and jokes that we used to have at the dinner table. I am thankful to my Belle collaboration friends Minakshi, Vipin, Saurav, Nisar, Anu and others for various analysis related discussions.

Last but not the least, I am extremely grateful to my parents and my elder brother for their love, care, support and encouragement throughout my life. I thank them for staying beside me in my good and bad days. I thank my brother for helping me in computer related issues. I thank my well wishers and all people who have helped me directly or indirectly, whose name I may have inadvertently forgotten. Above all, I thank God for everything.

Abstract

We measure the branching fraction for the decay $B_s^0 \to \phi\gamma$ *and search for the decay* $B_s^0 \to \gamma\gamma$ *using 121.4* fb^{-1} *of data collected at the* $\Upsilon(5\mathrm{S})$ *resonance with the Belle detector at the KEKB asymmetric energy B-factory located at the High Energy Accelerator Research Organization (KEK), Japan.* $B_s^0 \to \phi\gamma$ *branching fraction is computed to be* $(3.7^{+0.6}_{-0.5} \pm 0.7) \times 10^{-5}$ *with a signal significance of 10.6 including the systematic uncertainties. This result is in good agreement with the theoretical predictions and a recent indirect estimate from LHCb. We do not observe any significant signal for the* $B_s^0 \to \gamma\gamma$ *decay and have thus set the* 90% *confidence level upper limit on its branching fraction to be* 3.1×10^{-6}*. This result improves on the previously published* 90% *confidence level upper limit by a factor of about 3 and provides the most stringent limit till date.*

Preface

This thesis reports a measurement of the branching fraction (BF) for the decay $B_s^0 \to \phi\gamma$ and search for the decay $B_s^0 \to \gamma\gamma$ at high energy e^+e^- collisions at $\Upsilon(5S)$ energy. These are flavor changing neutral current (FCNC) processes which involve a b to s quark loop transition. The decay $B_s^0 \to \phi\gamma$ was first observed by the Belle Collaboration with a signal significance of 5.5 and its BF was measured to be $(5.7^{+1.8+1.2}_{-1.5-1.1}) \times 10^{-5}$. Using indirect measurements, LHCb has estimated the $B_s^0 \to \phi\gamma$ BF to be $(3.5 \pm 0.4) \times 10^{-5}$. Theory calculations within the SM framework predict the $B_s^0 \to \phi\gamma$ BF to be in the range $(3.9 - 4.3) \times 10^{-5}$ with around 30% uncertainty. The decay $B_s^0 \to \gamma\gamma$ is yet to be observed and its upper limit at 90% confidence level (CL) is estimated to be 8.7×10^{-6}. This result is still an order of magnitude larger than the Standard Model (SM) expectations which lie in the range $(0.18 - 1.0) \times 10^{-6}$ with over 20% uncertainty.

The results presented in the thesis are based on 121.4 fb^{-1} of data collected at the $\Upsilon(5S)$ resonance with the Belle detector, located at High Energy Accelerator Research Organization (KEK), Japan. At $\Upsilon(5S)$ resonance, the B_s^0 mesons are produced primarily in the decays of B_s^{0*} mesons to the ground state with the emission of a photon. The $b\bar{b}$ production cross-section at $\Upsilon(5S)$ has been measured to be $\sigma_{b\bar{b}}^{\Upsilon(5S)} = (0.340 \pm 0.016)\ nb$ and the fraction of $B_s^{(*)}\bar{B}_s^{(*)}$ events in $b\bar{b}$ events is found to be $f_s = (17.2 \pm 3.0)\%$. The $B_s^{(*)}\bar{B}_s^{(*)}$ events include $B_s^{0*}\bar{B}_s^{0*}$, $B_s^{0*}\bar{B}_s^0$ and $B_s^0\bar{B}_s^0$ events, the fraction of $B_s^{0*}\bar{B}_s^{0*}$ and $B_s^{0*}\bar{B}_s^0$ being $f_{B_s^{0*}\bar{B}_s^{0*}} = (87.0 \pm 1.7)\%$ and $f_{B_s^{0*}\bar{B}_s^0} = (7.3 \pm 1.4)\%$. Various selection criteria are applied to select the $B_s^0 \to \phi\gamma$ and $B_s^0 \to \gamma\gamma$ candidates and for efficient background rejection. For the $B_s^0 \to \phi\gamma$ analysis, we have observed 80^{+12}_{-11} signal events with a signal significance of 10.6 in the $(B_s^0 \to \phi\gamma)_{B_s^{0*}\bar{B}_s^{0*}}$ signal region. No significant signals are observed in the other two signal regions. These signal yields are compatible with the production fractions of $B_s^{0*}\bar{B}_s^{0*}$, $B_s^{0*}\bar{B}_s^0$ and $B_s^0\bar{B}_s^0$ events at $\Upsilon(5S)$. We have measured the branching fraction of $B_s^0 \to \phi\gamma$ to be $(3.7^{+0.6}_{-0.5} \pm 0.7) \times 10^{-5}$. This improved measurement supersedes the previous Belle result that was based on a smaller data sample and is consistent with theoretical predictions and a recent estimate from LHCb.

We donot observe any significant signal for $B_s^0 \to \gamma\gamma$ and have thus estimated the 90% CL upper limit on its BF to be 3.1×10^{-6}. This limit improves on the previously reported value by a factor of about 3 and is the most stringent one till date. This result is consistent with the statistics of our data sample and SM predictions that indicates the possibility of observing this decay mode at Belle II with a dedicated run at $\Upsilon(5S)$ resonance.

This thesis contains the following chapters:

Chapter 1 provides an introduction to the SM of particle physics, the dynamics of electroweak and strong interaction and the associated gauge transformations. It then provides a brief overview of Cabibbo-Kobayashi-Maskawa (CKM) matrix, GIM mechanism and FCNC processes. A brief introduction to renormalization and effective field theory is then presented. Various analysis techniques namely, the exclusive, the inclusive and the semi-inclusive reconstruction method are discussed briefly. This chapter concludes with a brief discussion on the current status of the decays $B_s^0 \to \phi\gamma$ and $B_s^0 \to \gamma\gamma$.

Chapter 2 provides a brief discussion on the Υ(nS) resonances, the KEKB accelerator, the Belle detector, data acquisition and the trigger system. A brief description on the processing of the raw data set and skimming of data samples is also provided.

Chapter 3 provides a description of the analysis strategy, the Belle datasets, Monte Carlo event generation procedure and the blind analysis technique used to study the decays $B_s^0 \to \phi\gamma$ and $B_s^0 \to \gamma\gamma$. The skim, candidate and signal selection criteria for these analyses are then discussed. Possible backgrounds are analyzed, and their suppression studied and discussed in details in this chapter.

Chapter 4 presents the PDF parameterizations of signal and background for both $B_s^0 \to \phi\gamma$ and $B_s^0 \to \gamma\gamma$ analyses. It also discusses the estimation of various calibration factors from $B_s^0 \to D_s\pi$, $B^0 \to K^{0*}\gamma$ control samples and from $B_s^0 \to \phi\gamma$ analysis. It then provides a brief discussion on the fit strategy for both the analyses. Pseudo-experiments are performed to test the stability of the fitters. This chapter presents the results of these pseudo-experiments. The final fit results are then presented.

Chapter 5 provides a brief discussion on systematic uncertainties. Various sources of systematic uncertainties and their estimation procedure are discussed in details in this chapter.

Chapter 6 summarizes the final results for both $B_s^0 \to \phi\gamma$ and $B_s^0 \to \gamma\gamma$ analyses. The estimation of signal significance, BF calculation for $B_s^0 \to \phi\gamma$ and the estimation of 90% CL upper limit for $B_s^0 \to \gamma\gamma$ analysis are explained in details in this chapter. This chapter concludes with a brief discussion on the possible implications of the results of these analysis.

Contents

List of Figures

List of Tables

Chapter 1

Theoretical Framework and Motivations

This chapter provides an introduction to the Standard Model (SM) of particle physics, the dynamics of electroweak and strong interactions and the associated gauge transformations. It then provides a brief overview of Cabibbo-Kobayashi-Maskawa (CKM) matrix, Glashow-Iliopoulos-Maiani (GIM) mechanism and flavor changing neutral current (FCNC) processes. A brief introduction to effective field theory (EFT) and various analysis techniques are then presented. This thesis is devoted to the study of rare decays $B_s^0 \to \phi\gamma$ and $B_s^0 \to \gamma\gamma$. Precision measurements of the rare decays allow us to access new particles produced virtually through loop processes, thus providing a way to search for new physics and test the SM at higher energy scales. This is not possible through direct searches due to limitation of experimentally available center of mass (CM) energy. This chapter concludes with a brief discussion on the current status of these decays.

1.1 The Standard Model of Particle Physics

High energy physics (HEP) seeks to answer questions about the smallest building blocks of matter and the forces with which they interact. Our current understanding, according to the SM [1–4] is that everything in the universe is built up from fundamental spin-1/2 particles called quarks and leptons which interact via the gauge bosons, having integral spins. The SM is a relativistic quantum field theory (QFT) that describes all known interactions except gravitation. It is invariant under transformations of the gauge group $\mathrm{SU(3)_C} \otimes \mathrm{SU(2)}_L \otimes \mathrm{U(1)}_Y$. $\mathrm{SU(3)_C}$ and $\mathrm{SU(2)}_L$ are special unitary groups of color (C) charges and weak isospin, that describe the strong interaction among quarks and the weak interaction among quarks and leptons, respectively. $\mathrm{U(1)}_Y$ is a unitary group of hypercharge (Y) that describes the electromagnetic interaction.

Gauge invariance [1, 3, 4] refers to continuous transformations under a group $\mathcal{G}$, which leaves the Lagrangian (or the system) invariant. The simplest such transformation is $\psi \mapsto \psi' = e^{-i\beta}\psi$, where ψ is a fermion field and β is a constant (this is a transformation belonging to the global U(1) group). The Lagrangian density (of massless fermion fields), given by:

$$\mathcal{L} = \bar{\psi} i \gamma^{\mu} \partial_{\mu} \psi \tag{1.1}$$

is invariant under this transformation (i.e., $\mathcal{L}' = e^{-i\beta}\mathcal{L} = \mathcal{L}$) since the observables depend on $|\psi|^2$. For local U(1) symmetry (for e.g., the electromagnetic field) when we introduce a space-time dependence on ψ ($\psi \mapsto e^{-i\chi(x,t)}\psi$), the Lagrangian is not invariant anymore. The Lagrangian can then be made invariant by replacing the derivative ∂_μ by a covariant derivative D_μ defined by:

$$D_\mu \equiv \partial_\mu - igA_\mu(x) \tag{1.2}$$

where g is a constant (coupling constant) and A_μ is a U(1) gauge field. This formalism can be extended to more complicated groups like SU(2) and SU(3) (non-abelian groups), by introducing the corresponding generators in the transformations and organizing the fermions in multiplets of gauge groups. The full covariant derivative incorporating the electromagnetic, weak and strong interactions [1] can be written as:

$$D_\mu \equiv \partial_\mu - ig_1 \frac{Y}{2} F_\mu(x) - ig_2 \frac{\tau^i}{2} . W_\mu^i - ig_3 \frac{\lambda^a}{2} . G_\mu^a \tag{1.3}$$

where, F_μ, W_μ and G_μ are the spin-1 gauge fields that represent the electromagnetic, weak and strong interaction, respectively. τ^i's (i=1,2,3) and λ^a's (a=1,...,8) are the generators of SU(2) and SU(3) groups representing the weak and strong force respectively. Y (which is just a number) is the U(1) hypercharge generator and g's are the coupling constants for various interactions. For SU(2) and SU(3) symmetry, ψ transforms like $\psi \mapsto \psi' = e^{-i\vec{\epsilon}.\vec{\tau}/2}$ and $\psi \mapsto \psi' = e^{-i\vec{\alpha}.\vec{\lambda}/2}$, where ϵ's and α's denote the rotation parameters of SU(2) and SU(3) space.

The SM Lagrangian [4, 5] can be written as:

$$\boldsymbol{\mathcal{L}^4_{\mathrm{SM}} = \mathcal{L}_{\mathrm{QCD}} + \mathcal{L}_{\mathrm{ew}} + \mathcal{L}_{H} + \mathcal{L}_{\mathrm{Yu}}} \tag{1.4}$$

The superscript (4) indicates that the Lagrangian has mass dimensions 4.

$\mathcal{L}_{\mathrm{QCD}}$ is the quantum chromodynamics (QCD) Lagrangian [1, 4, 5] given as:

$$\boldsymbol{\mathcal{L}_{\mathrm{QCD}} = \sum_j \bar{q}_j i\gamma^{\mu} \left(\partial_{\mu} - i\frac{g_3}{2}\vec{\lambda}.\vec{G}_{\mu} \right) q_j - \frac{1}{4} G^{a}_{\mu\nu} G^{\mu\nu}_{a}} \tag{1.5}$$

which describes the color interaction between quarks (q's)and gluons, with SU(3) symmetry. Each of the quarks appear in 3 colors. So, when quarks appear in the Lagrangian, sum over color is implicit. Here, q_j is a color triplet quark field (the index j runs over the 6 flavors) and $G^{a}_{\mu\nu}$'s are the strength tensors of 8 gluon fields $\vec{G}_{\mu}$, expressed as:

$$G^{a}_{\mu\nu} = \partial_{\mu} G^{a}_{\nu} - \partial_{\nu} G^{a}_{\mu} - g_3 f^{abc} G^{b}_{\mu} G^{c}_{\nu}$$

where, f^{abc} is the structure constant corresponding to SU(3) interaction.

$\mathcal{L}_{\mathrm{ew}}$ represents the electroweak Lagrangian term [1, 4, 5] that describes the interactions between fermions and vector bosons through the symmetry groups $\mathrm{SU}(2)_L \otimes \mathrm{U}(1)_Y$. It is written as:

$$\boldsymbol{\mathcal{L}_{\mathrm{ew}} = \sum_i \bar{\psi}^{i} i\gamma^{\mu} \left(\partial_{\mu} - i\frac{g_1}{2} Y F_{\mu} - i\frac{g_2}{2}\vec{\tau}.\vec{W}_{\mu} \right) \psi_i - \frac{1}{4} F_{\mu\nu} F^{\mu\nu} - \frac{1}{4} W^{j}_{\mu\nu} W_{j}^{\mu\nu}} \tag{1.6}$$

ψ^i represents the fermion wavefunctions and are represented in terms of left-handed SU(2) doublets (ψ_L) and right-handed singlets (ψ_R) as: $\left\{ L_L, Q_L \right\}$ and $\psi_R \in \left\{ e_R, \mu_R, \tau_R, q_R \right\}$ where, $L_L \in \left\{ \begin{pmatrix} \nu_e \\ e^- \end{pmatrix}_L, \begin{pmatrix} \nu_\mu \\ \mu^- \end{pmatrix}_L, \begin{pmatrix} \nu_\tau \\ \tau^- \end{pmatrix}_L \right\}$ and $Q_L \in \left\{ \begin{pmatrix} u' \\ d' \end{pmatrix}_L, \begin{pmatrix} c' \\ s' \end{pmatrix}_L, \begin{pmatrix} t' \\ b' \end{pmatrix}_L \right\}$ are left − handed lepton and quark doublets and $q_R \in \left\{ u'_R, d'_R, c'_R, s'_R, t'_R, b'_R \right\}$ represents the right – handed quarks. Here, the quarks are represented with primed symbols since the electroweak eigenstates donot necessarily coincide with the mass eigenstates. $F_{\mu\nu}$ and $W^i_{\mu\nu}$'s are the strength tensors of the photon field $\overrightarrow{F}_\mu$ and 3 weak boson fields $\overrightarrow{W}_\mu$ given as: $F_{\mu\nu} = \partial_\mu F_\nu - \partial_\nu F_\mu$ and $W^{\ i}_{\mu\nu} = \partial_\mu W_\nu^{\ i} - \partial_\nu W_\mu^{\ i} - g_2 \Sigma^{\ ijk} W_\mu^{\ j} W_\nu^{\ k}$ where, Σ^{ijk} is the structure constant corresponding to the SU(2) interaction. The first term of equation 1.6 is the fermion boson interaction term [1, 5, 6] and is given by:

$$\mathcal{L}_{\text{int,ew}} = \mathcal{L}_{\text{CC}} + \mathcal{L}_{\text{NC}} = \frac{g_2}{\sqrt{2}} \left(j_L^{\mu+} W_\mu^+ + j_L^{\mu-} W_\mu^- \right) + \left(e j_{\text{em}}^{\mu} B_\mu + g_Z j_Z^{\mu} Z_\mu \right) \tag{1.7}$$

where, $e = g_1$ is the electromagnetic coupling constant; $g_Z = \frac{g_2}{2\cos\theta_W}$ is the weak coupling constant corresponding to the Z boson with $\sin\theta_W = \frac{g_1}{\sqrt{{g_1}^2 + {g_2}^2}}$ and $\cos\theta_W = \frac{g_2}{\sqrt{{g_1}^2 + {g_2}^2}}$, θ_W being the Weinberg angle; $j_{\text{em}}^{\mu} = \sum\limits_f Q_f \bar{f} \gamma^{\,\mu} f = \sum\limits_f Q_f \left(\bar{f}_L \gamma^{\,\mu} f_L + \bar{f}_R \gamma^{\,\mu} f_R \right)$ and $j_Z^{\mu} = \sum\limits_f \bar{f}_L \gamma^{\,\mu} f_L \left(I_f^3 - Q_f \sin^2\theta_W \right) + \bar{f}_R \gamma^{\,\mu} f_R \left(-Q_f \sin^2\theta_W \right)$ are the neutral currents carried by the photon field (B_μ[1]) and Z boson, respectively with 'f' representing the fermion states; Q_f and I_f^3 denote the charge and the third component of weak isospin respectively. The terms $j_L^{\mu+} = \left(\bar{u}'_L \gamma^{\,\mu} d'_L + \bar{c}'_L \gamma^{\,\mu} s'_L + \bar{t}'_L \gamma^{\,\mu} b'_L + \sum\limits_l \nu_{lL} \gamma^{\,\mu} l_L \right)$ and $j_L^{\mu^-} = \left(j_L^{\mu^+} \right)^\dagger$ are the left handed (charged) currents carried by the physical bosons $W^\pm$. l_L denotes the left-handed charged leptons (e^-, μ^- and τ^-). The physical bosons $W^\pm$ and Z and the photon field B_μ can be written as:

$$W_\mu^{\,\pm} = \frac{W_\mu^{\ 1} \mp i W_\mu^{\ 2}}{\sqrt{2}}, \quad Z_\mu = \frac{g_1 Y_L F_\mu + g_2 W_\mu^{\ 3}}{\sqrt{g_1^2 Y_L^2 + g_2^2}} \text{ and } B_\mu = \frac{g_2 F_\mu - g_1 Y_L W_\mu^{\ 3}}{\sqrt{g_1^2 Y_L^2 + g_2^2}}.$$

The term $\mathcal{L}_H$ represents the Higgs Lagrangian which is required to account for the masses of the fermions and the gauge bosons. The SM is based on the assumption that the universe is filled with a spin-0 field called the Higgs field ϕ, that is a doublet in the SU(2) space and carries a non-zero U(1) hypercharge, but is a singlet in color space. The gauge bosons and fermions can interact with this field and they get their mass by interacting with this field. The Higgs Lagrangian [1, 5] has the form:

$$\boldsymbol{\mathcal{L}_H = (D_\mu \phi)^\dagger (D^{\,\mu} \phi) - V(\phi) \equiv (D_\mu \phi)^\dagger (D^{\,\mu} \phi) - \mathcal{M}^2 \phi^\dagger \phi - \lambda \left(\phi^\dagger \phi \right)^2} \tag{1.8}$$

---

[1] The original photon field F_μ is transformed to B_μ by the Higgs mechanism. This is explaned later in this chapter.

Here, the first term $(D_\mu\phi)^\dagger(D^{\,\mu}\phi)$ represents the kinetic or dynamical Higgs term and $V(\phi) = \mathcal{M}^2\phi^\dagger\phi + \lambda\,(\phi^\dagger\phi)^2$ denotes the Higgs potential. $\mathcal{M}$ and λ are the parameters of the Higgs potential. The Higgs field ϕ is a SU(2) doublet of complex fields ϕ^+ and ϕ^0 represented by $\phi = \begin{pmatrix}\phi^+\\ \phi^0\end{pmatrix}$ where, $\phi^+ = \dfrac{\phi_1 + i\phi_2}{\sqrt{2}}$ and $\phi^0 = \dfrac{\phi_3 + i\phi_4}{\sqrt{2}}$, ϕ_i's being the components of real and imaginary fields.

The Yukawa term [1] describes the interaction of Higgs field with the matter fields. It is of the form:

$$\boldsymbol{\mathcal{L}_{\mathrm{Yu}} = Y^{\,u}_{i,j}\,(\bar{Q}^{'}_{Li}\tilde{\phi})\,u^{'}_{Rj} + Y^{\,d}_{i,j}\,(\bar{Q}^{'}_{Li}\phi)\,d^{'}_{Rj} + Y^{\,e}_{i,j}\,(\bar{L}^{'}_{Li}\phi)\,e^{'}_{Rj} + h.c.} \tag{1.9}$$

where, $\tilde{\phi} = i\tau_2\phi$. The Yukawa matrices (couplings) $Y^{u,d,e}$ are arbitrary 3×3 complex matrices for the three generations (i, j) of quarks; *h.c.* represents the Hermitian conjugate.

Thus, the SM Lagrangian ($\mathcal{L}^{(4)}_{\mathrm{SM}}$) represented by equation 1.4 can be written as:

$$\begin{aligned}\boldsymbol{\mathcal{L}^{4}_{\mathrm{SM}}} &= \boldsymbol{-\frac{1}{4}\,G^{\,a}_{\mu\nu}G^{\,\mu\nu}_{a} - \frac{1}{4}\,W^{\,j}_{\mu\nu}W^{\,\mu\nu}_{j} - \frac{1}{4}\,F_{\mu\nu}F^{\,\mu\nu} + \Big[(D_\mu\phi)^\dagger(D^{\,\mu}\phi) - \mathcal{M}^2\phi^\dagger\phi -}\\ &\quad \boldsymbol{\lambda\,(\phi^\dagger\phi)^2\Big] + i\,\Big(\bar{L}_L \not{D} L_L + \bar{e}_R \not{D} e_R + \bar{Q}_L \not{D} Q_L + \bar{u}_R \not{D} u_R + \bar{d}_R \not{D} d_R\Big)}\\ &\quad \boldsymbol{-\Big[Y^{\,u}_{i,j}\,(\bar{Q}^{'}_{Li}\tilde{\phi})\,u^{'}_{Rj} + Y^{\,d}_{i,j}\,(\bar{Q}^{'}_{Li}\phi)\,d^{'}_{Rj} + Y^{\,e}_{i,j}\,(\bar{L}^{'}_{Li}\phi)\,e^{'}_{Rj} + h.c.\Big]}\end{aligned} \tag{1.10}$$

The λ term in the Higgs Lagrangian describes quartic self-interactions among the scalar fields. Vacuum stability demands λ to be greater than 0. The lowest energy or the ground state of the system occurs when both the kinetic energy (K.E.) and potential energy (P.E.) is minimum. The K.E. is minimum when $\phi(x)$ is constant. The P.E. of the system is minimum when $\dfrac{\partial V}{\partial\phi} = 0$ i.e., when $\phi^\dagger\phi = -\dfrac{\mu^2}{2\lambda} \equiv \dfrac{\mathfrak{v}}{2}$ and $\mu^2 < 0$. Here, $\mathfrak{v}$ is the vacuum expectation value (VEV) of the field ϕ. Thus, there are infinite number of degenerate states with minimum energy. The symmetry of the vacuum (or ground state) is broken spontaneously by the choice of a particular VEV. We arbitrarily choose $\langle\phi\rangle = \phi_0 = \dfrac{1}{\sqrt{2}}\begin{pmatrix}0\\ \mathfrak{v}\end{pmatrix}$ i.e., $\phi_3 = \mathfrak{v}$. When a symmetry is broken that way i.e., the symmetry is valid in the Lagrangian but not for the ground state of the system, it is said to be a spontaneously broken symmetry and the phenomenon is called spontaneous symmetry breaking (SSB). Owing to the conservation of electric charge, only a neutral scalar field can acquire a VEV. Thus, with this choice ϕ^0 is to be interpreted as the neutral component of the doublet. Since the Higgs field $\phi(x)$ is a doublet, but only one component gets a vacuum expectation value, the SU(2) symmetry is broken. When ϕ gets the vacuum expectation value, the K.E. and the P.E. term of the Higgs Lagrangian becomes:

$$\frac{1}{8}\left|\begin{pmatrix} g_1F_\mu + g_2W_\mu^3 & g_2(W_\mu^1 - iW_\mu^2) \\ g_2(W_\mu^1 - iW_\mu^2) & g_1F_\mu - g_2W_\mu^3 \end{pmatrix}\right| = \frac{1}{8}\mathfrak{v}^2 g_2^2\Big((W_\mu^1)^2 + (W_\mu^2)^2\Big) + \frac{1}{8}\mathfrak{v}^2\Big(g_1F_\mu - g_2W_\mu^3\Big)^2$$

$$\text{and}\quad \frac{\mu^2}{2}\begin{pmatrix}0 & \mathfrak{v}+H(x)\end{pmatrix}\begin{pmatrix}0 \\ \mathfrak{v}+H(x)\end{pmatrix} + \frac{\lambda}{4}\left[\begin{pmatrix}0 & \mathfrak{v}+H(x)\end{pmatrix}\begin{pmatrix}0 \\ \mathfrak{v}+H(x)\end{pmatrix}\right]^2,\ \text{respectively}$$

The term $\frac{1}{8}\mathfrak{v}^2 g_2^2\Big((W_\mu^1)^2 + (W_\mu^2)^2\Big)$ can be written as $\Big(\frac{1}{2}\mathfrak{v}g_2\Big)^2 W_\mu^+ W_\mu^-$, the mass of W boson W_μ being $\frac{1}{2}\mathfrak{v}g_2$. The term $\frac{1}{8}\mathfrak{v}^2\left(g_1F_\mu - g_2W_\mu^3\right)^2$ can be expressed as $\mathrm{m}_B B_\mu + \mathrm{m}_Z Z_\mu$ with, $\mathrm{m}_B = 0$ and $\mathrm{m}_Z = \frac{\mathfrak{v}}{2}\sqrt{g_1^2 + g_2^2}$. Thus, the original photon field F_μ is transformed to the massless gauge boson (photon) field B_μ. The P.E. term of the Higgs Lagrangian gives term having the form $m_H H^2$, where m_H is the Higgs particle mass given as $\mathrm{m}_H = \sqrt{2\lambda\mathfrak{v}^2} = \sqrt{-\mathcal{M}^2}$. The Yukawa couplings, which give rise to the fermion (lepton and quark) masses can now be written as:

$$\mathcal{L}_{Yu} = Y_{i,j}^u\left(\bar{u}_{Li}^{'}\frac{\mathfrak{v}+H}{\sqrt{2}}\right)u_{Rj}^{'} + Y_{i,j}^d\left(\bar{d}_{Li}^{'}\frac{\mathfrak{v}+H}{\sqrt{2}}\right)d_{Rj}^{'} + Y_{i,j}^e\left(\bar{e}_{Li}^{'}\frac{\mathfrak{v}+H}{\sqrt{2}}\right)e_{Rj}^{'} + h.c.$$

Now, $M_{ij}^u = \mathfrak{v}Y_{ij}^u/\sqrt{2}$, $M_{ij}^d = \mathfrak{v}Y_{ij}^d/\sqrt{2}$ and $M_{ij}^e = \mathfrak{v}Y_{ij}^e/\sqrt{2}$ denotes the masses of the *up, down type quarks* and *charged leptons*, respectively. Therefore,

$$\begin{aligned}\mathcal{L}_{Yu} &= \left[\bar{u}_{Li}^{'}\left(M_{ij}^u + \frac{M_{ij}^u}{\mathfrak{v}}H\right)u_{Rj}^{'} + \bar{d}_{Li}^{'}\left(M_{ij}^d + \frac{M_{ij}^d}{\mathfrak{v}}H\right)d_{Rj}^{'} + \bar{e}_{Li}^{'}\left(M_{ij}^e + \frac{M_{ij}^e}{\mathfrak{v}}H\right)e_{Rj}^{'}\right] + h.c.\\ &= \Bigg[\bar{u}_{Li}^{'}(V_L^{u\dagger}V_L^u)\left(M_{ij}^u + \frac{M_{ij}^u}{\mathfrak{v}}H\right)(V_R^{u\dagger}V_R^u)u_{Rj}^{'} + \bar{d}_{Li}^{'}(V_L^{d\dagger}V_L^d)\left(M_{ij}^d + \frac{M_{ij}^d}{\mathfrak{v}}H\right)(V_R^{d\dagger}V_R^d)d_{Rj}^{'}\\ &\qquad + \bar{e}_{Li}^{'}(V_L^{e\dagger}V_L^e)\left(M_{ij}^e + \frac{M_{ij}^e}{\mathfrak{v}}H\right)(V_R^{e\dagger}V_R^e)e_{Rj}^{'}\Bigg] + h.c.\end{aligned}$$

The terms $\frac{M_{ij}^u}{\mathfrak{v}}\bar{u}_{Li}^{'}u_{Rj}^{'}H$, $\frac{M_{ij}^d}{\mathfrak{v}}\bar{d}_{Li}^{'}d_{Rj}^{'}H$ and $\frac{M_{ij}^e}{\mathfrak{v}}\bar{e}_{Li}^{'}e_{Rj}^{'}H$ denotes the Higgs interaction vertices with the *up, down type quarks* and with *charged leptons*. No mass term is generated for neutrinos, since it is assumed that right handed neutrino doesnot exist. The matrices M^u, M^d and M^e should be diagonalized using unitary matrices V^u, V^d and V^e as: $M^u_{\text{diag}} = V^u_L M^u V^{u\dagger}_R$, $M^d_{\text{diag}} = V^d_L M^d V^{d\dagger}_R$ and $M^e_{\text{diag}} = V^e_L M^e V^{e\dagger}_R$ to obtain the proper mass terms. The mass eigenstates $(u,d)_{L,R}$ can thus be written in terms of interaction eigenstates $(u,d)'_{L,R}$ as: $(u,d)_{Li} = (V^{u,d}_L)_{ij}(u,d)'_{Lj}$ and $(u,d)_{Ri} = (V^{u,d}_R)_{ij}(u,d)'_{Rj}$.

Therefore, $\boldsymbol{\mathcal{L}_{\mathbf{Yu}} = \bar{u}_{Li}(M^u_{ij})_{\mathbf{diag}} u_{Rj} + \bar{d}_{Li}(M^d_{ij})_{\mathbf{diag}} d_{Rj} + \bar{e}_{Li}(M^e_{ij})_{\mathbf{diag}} e_{Rj} +}$

$$\boldsymbol{\bar{u}_{Li}\left(\frac{(M^u_{ij})_{\mathbf{diag}}H}{\mathfrak{v}}\right)u_{Rj} + \bar{d}_{Li}\left(\frac{(M^d_{ij})_{\mathbf{diag}}H}{\mathfrak{v}}\right)d_{Rj} + \bar{e}_{Li}\left(\frac{(M^e_{ij})_{\mathbf{diag}}H}{\mathfrak{v}}\right)e_{Rj} + h.c.} \tag{1.11}$$

Unfortunately, when introducing a mass term in the Lagrangian, the SU(2) ⊗ U(1) symmetry is spontaneously broken to electromagnetic $\text{U}(1)_{\text{Q}}$.

$$\mathbf{SU(3)_C \otimes SU(2)}_{\boldsymbol{L}} \mathbf{\otimes U(1)}_{\boldsymbol{Y}} \xrightarrow{\mathbf{SSB}} \mathbf{SU(3)_C \otimes U(1)_Q} \tag{1.12}$$

The SM Lagrangian after SSB, can be obtained by replacing the Yukawa term in equation 1.10 by equation 1.11.

At present, only 3 generations of quarks and leptons have been observed. 4 or more generations of quarks are considered to be unlikely as this will induce slight modifications to various electroweak observables which are strongly disfavored by experimental measurements [7]. Furthermore, the measured width of the Z boson rules out a fourth quark generation with a ‘light’ neutrino (neutrino having mass less than about 45 GeV/c^2) [3, 8, 9].

During the last few decades, many experimental studies have been performed in order to test the validity of the SM and so far no large discrepancies have been found. Also the SM has so far been successful in explaining the vast amount of existing experimental data. However, the SM provides poor explanations for the flavor dependence of particle properties (mass, number of families, etc), hierarchial structure of CKM matrix, matter-antimatter asymmetry [3, 10], existence of dark matter [3, 11] and the presence of symmetries like conservation of baryon and lepton numbers [3]. Further, it couldnot account for the neutrino oscillations [3, 12]. Neutrinos are considered to be massless in the SM. However, the observation of neutrino mixing indicates that they are massive. Whether the SM is an approximation of a more general theory, valid in some scales still needs to be ascertained. Answering these questions requires probing matter upto very small distances, which requires high energies that is possible only through colliders. In this thesis, we search for the rare decays $B_s^0 \to \phi\gamma$ and $B_s^0 \to \gamma\gamma$ at high energy e^+e^- collisions at $\Upsilon(5S)$ energy. Both these decays are FCNC processes [3, 13] involving $b \to s$ transitions. $b \to s$ and $b \to d$ transitions are forbidden at tree level in the SM and can only be generated via the loop diagrams. These processes that change the flavor of a quark without altering its electric charge are called FCNC transitions. They are highly suppressed via the GIM mechanism [14] and the loop factors in the SM. The study of rare decays involving the loop processes provide a good opportunity to search for physics beyond the SM as new particles which can couple with the quarks can appear in the loop.

1.2 Flavor Changing Neutral Current Processes

In this section we discuss about the FCNC processes and explain why these processes are rare in the SM. The charged current term of the electroweak interaction Lagrangian (equation 1.7) is given by:

$$\mathcal{L}_{\mathrm{CC}} = \frac{g_2}{\sqrt{2}}\left(j_L^{\mu+} W_\mu^+\right) + h.c., \text{ where } j_L^{\mu+} = \sum_{ij} \bar{u}'_i \gamma^\mu \left(\frac{1-\gamma^5}{2}\right) d'_j + \sum_i \bar{\nu}_i \gamma^\mu \left(\frac{1-\gamma^5}{2}\right) e_i$$

and the neutral current term (mediated by the Z boson) is given by:

$$(\mathcal{L}_{\mathrm{NC}})_Z = g_z j_Z^\mu Z_\mu, \text{ where } j_Z^\mu = \sum_f g_L^f \bar{f} \gamma^\mu \left(\frac{1-\gamma^5}{2}\right) f + \sum_f g_R^f \bar{f} \gamma^\mu \left(\frac{1+\gamma^5}{2}\right) f$$

Now,

$$\sum_{ij} \bar{u}'_i \gamma^\mu (1-\gamma^5) d'_j = \begin{pmatrix} \bar{u}' & \bar{c}' & \bar{t}' \end{pmatrix} \gamma^\mu (1 - \gamma^5) \begin{pmatrix} d' \\ s' \\ b' \end{pmatrix}$$

$$= V_{\rm CKM}\,(\,\bar{u}\;\;\bar{c}\;\;\bar{t}\,)\,\gamma^{\mu}\,(\,1\;-\;\gamma^{5}\,)\begin{pmatrix} d \\ s \\ b \end{pmatrix}$$

where,

$$\begin{pmatrix} u' \\ c' \\ t' \end{pmatrix} = V^{u}\begin{pmatrix} u \\ c \\ t \end{pmatrix} \text{ and } \begin{pmatrix} d' \\ s' \\ b' \end{pmatrix} = V^{d}\begin{pmatrix} d \\ s \\ b \end{pmatrix}.$$

$V_{\rm CKM} = V^{u\dagger}V^{d}$ is a unitary matrix known as CKM matrix represented in the standard parametrization [15] as:

$$V_{\rm CKM} = \begin{pmatrix} V_{ud} & V_{us} & V_{ub} \\ V_{cd} & V_{cs} & V_{cb} \\ V_{td} & V_{ts} & V_{tb} \end{pmatrix}$$
$$= \begin{pmatrix} c_{12}c_{13} & s_{12}s_{13} & s_{13}e^{-i\delta} \\ -s_{12}c_{23} - c_{12}s_{23}s_{13}e^{i\delta} & c_{12}s_{23} - s_{12}s_{23}s_{23}e^{i\delta} & s_{23}c_{13} \\ s_{12}c_{23} - c_{12}s_{23}s_{13}e^{i\delta} & -s_{23}c_{12} - s_{12}c_{23}s_{13}e^{i\delta} & c_{23}c_{13} \end{pmatrix} \quad (1.13)$$

where, θ_{12}, θ_{23}, and θ_{13} are the three Euler angles and δ is the CP violating phase. The symbols s_{ij}'s and c_{ij}'s denote the sines and cosines of these angles. θ_{12} is the Cabibbo angle.

In Wolfenstein parametrization [16], the CKM matrix can be written as:

$$V_{\rm CKM} = \begin{pmatrix} 1-\frac{\lambda^2}{2} & \lambda & A\lambda^3(\rho - i\eta) \\ \lambda & 1-\frac{\lambda^2}{2} & A\lambda^2 \\ A\lambda^2(1-\rho-i\eta) & -A\lambda^2 & 1 \end{pmatrix} + \mathcal{O}(\lambda^4) \quad (1.14)$$

where A, λ, ρ and η are the four parameters represented as $s_{12} = \lambda$, $s_{23} = A\lambda^2$ and $s_{13}e^{-i\delta} = A\lambda^3(\rho - i\eta)$. Therefore,

$$\rho = \frac{s_{13}}{s_{12}s_{23}}{\rm cos}\delta \quad , \quad \eta = \frac{s_{13}}{s_{12}s_{23}}{\rm sin}\delta.$$

The η parameter is the complex phase parameter that is responsible for the CP violation in the SM. $\mathcal{O}(\lambda^4)$ denotes terms of the order of λ^4.

We observe non-zero off-diagonal elements in the CKM matrix, which indicates that generation changing charged currents are possible in the SM. The same operation for neutral current interaction for the up-sector yields:

$$(\bar{u}' \;\; \bar{c}' \;\; \bar{t}')\, \gamma^{\mu}\, (1 - \gamma^{5}) \begin{pmatrix} u' \\ c' \\ t' \end{pmatrix} = (\bar{u} \;\; \bar{c} \;\; \bar{t})\, \gamma^{\mu}\, (1 - \gamma^{5}) V^{u\dagger} V^{u} \begin{pmatrix} u \\ c \\ t \end{pmatrix}$$

Unitarity of V^u ensures that $V^{u\dagger}V^u = 1$ i.e., there is no generation changing neutral currents in the up-sector. The same holds true for the down-sector (the neutral current terms conserve flavor). FCNC transitions, such as $b \to s$ and $b \to d$ are thus forbidden at tree level in the SM. However, FCNCs are possible at higher orders since, contributions from different quark loops donot cancel exactly due to their different masses. At one loop level, the FCNC transitions can be summarized by a set of basic triple and quartic effective vertices known as penguin diagrams (ΔF = 1, F being the flavor of the quarks) and box diagrams (ΔF = 2) respectively [13, 17]. Penguin processes involve the emission of a neutral boson, either a gluon, photon or Z boson [18]. They can thus be classified into: (i) radiative, in which an external photon is emitted (Figure 1.1(a)), (ii) electroweak, in which the emitted virtual photon or Z boson produce lepton pairs (Figure 1.1(b)), (iii) annihilation penguin processes, in which the loop connects two quarks of the B meson (Figure 1.1(c) and (d)) and (iv) gluonic penguins, in which a gluon is emitted from the loop (Figure 1.1(e)). Figure 1.1(f) represents the box diagram. Since, FCNC processes occur through box or penguin diagrams, they are suppressed by a loop factor of $g_2^2/16\pi^2 \equiv 10^{-2}$. They are further suppressed due to GIM mechanism [14]. Due to the large suppression in the SM, the FCNC decays are ideal places to look for evidences of new physics. Precision measurements of these rare FCNC processes represent a sensitive probe for new-physics, as many new physics processes or extensions of the SM such as, supersymmetry with multi-Higgs doublets, extra quark models, fourth generation models, extra-dimensions, etc., can enhance or suppress FCNC decay rates [13]. This allows the indirect search for new physics. Measurements of FCNCs are model independent tests of any new-physics model that can contribute to change the overall properties (or observables) of the decay.

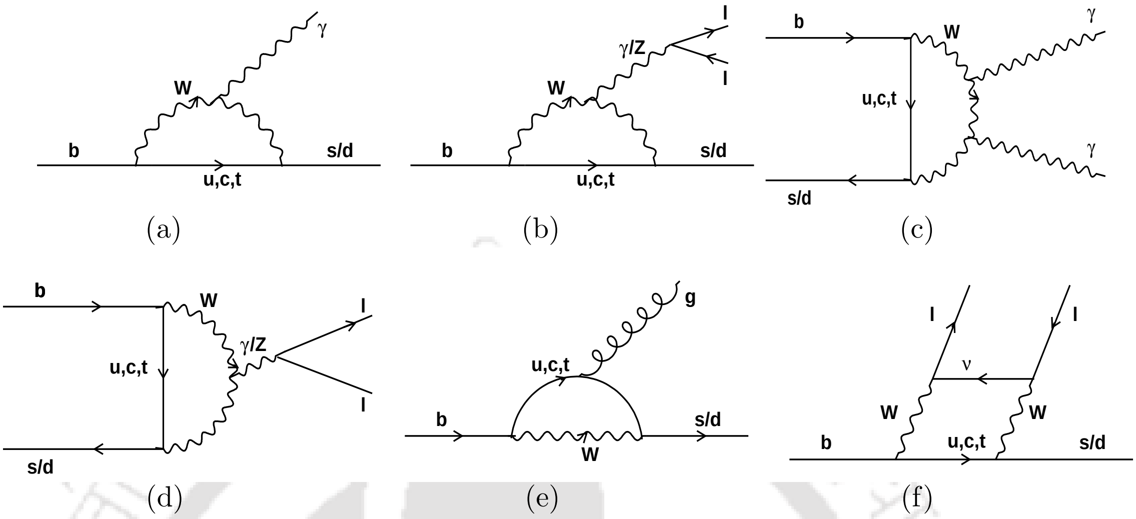

Figure 1.1: *Examples of FCNC processes.*
(a) Radiative penguin processes e.g., $b \to s(d)\gamma$ *(b) electroweak penguins e.g.,* $b \to s(d)l^+l^-$ *(c) annihilation penguins e.g.,* $B_{s(d)} \to \gamma\gamma$ *and (d)* $B_{s(d)} \to l^+l^-$ *(e) gluonic penguins e.g.,* $b \to s(d)g$ *(f) box diagrams e.g.,* $b \to s(d)l^+l^-$or$B_{s(d)} \to l^+l^-$.

1.3 Renormalization and Effective Field Theory

The basic principle of EFT [6, 17, 19–23] is that the dynamics of elementary particles at low energy doesnot depend on the details of the dynamics at high energies. As a result, physics at low energy scales can be described using an effective Lagrangian that contains only a few degrees of freedom, ignoring the additional degrees of freedom present at higher energies. For e.g., we do not need to know about the bottom quarks to describe the hydrogen atom. The process of integrating out the (irrelevant) heavy degrees of freedom from 'explicitly' appearing in the theory is called renormalization [6, 24]. The SM is also an EFT. In the absence of knowledge about the full theory, the observables for any decay process can be calculated using EFT. Information about physics beyond the SM can be obtained by comparing the experimental and the EFT result for rare decays. In the framework of an EFT, the Lagrangian can be written as an infinite expansion:

$$\mathcal{L}_{\Lambda}^{eff} = \sum_i \frac{\mathcal{C}_i(\mathcal{R})}{\Lambda^{d_i-4}} \mathcal{Q}_i \tag{1.15}$$

where, $\mathcal{C}_i$'s are dimensionless coefficients called the Wilson coefficients, which are related to the couplings of the full theory. $\mathcal{Q}_i$'s are the operators having dimension d_i's, built out of fields appearing in the theory. Λ is the characteristic energy scale of theory and $\mathscr{R}$ is the cutoff scale chosen just below Λ. Since the mass dimension of Lagrangian is 4, operators having mass dimension greater than 4 are numerically suppressed by powers of fundamental scale (i.e., Λ) of the theory. The higher the dimension of the operator, the more it will be suppressed. Thus, the lower dimensional operators are the important ones and the higher dimensional ones can be neglected. Physics from distances smaller than $\mathscr{R}^{-1}$ (i.e., contributions from scales higher than $\mathscr{R}$ or the high energy interactions) is contained in the Wilson coefficients $\mathcal{C}_i$ and that from distances greater than that (i.e., the low energy interactions) are accounted for by the operators. This approach of expressing the Lagrangian in this form is called operator product expansion (OPE) [6, 17–23]. The Wilson coefficients and the local operators, both depend on the renormalization scale $\mathscr{R}$ and renormalization scheme. The scale and scheme dependence of $\mathcal{C}_i$'s must be cancelled by the similar dependence of operators making the physical observables independent of them. The cutoff ($\mathscr{R}$) is generally chosen to be of the order of the mass of the decaying hadron (i.e., $\mathcal{O}(m_b)$, $\mathcal{O}(m_c)$ and $\mathcal{O}(1-2\text{ GeV})$ for B, D and K mesons). Depending on the precision goal one can truncate the series and thus, only a finite number of operators and couplings need to be retained.

The similarity of FCNC processes, in decays and mixing, allows us to describe almost all of them in terms of four fermion local operators. At tree level, the leading order effective Lagrangian for the four fermion process can be written as:

$$\mathcal{L}_{4f}^{eff} = \frac{G_F}{\sqrt{2}} J^{-}_{L\mu} J^{\mu+}_{L} \equiv \frac{G_F}{\sqrt{2}} \sum_i \mathcal{C}_i \mathcal{Q}_i \tag{1.16}$$

where, $\frac{G_F}{\sqrt{2}} \equiv \frac{g_2^2}{8M_W^2}$, G_F being the Fermi constant.

For four-fermion interaction, since each fermion line has a mass dimension of 3/2, so the operators involved in this case should have at least dimension 6. So, a M_W^{-2} scaling law for Wilson coefficients at leading order is needed. Thus, the non-local product of two charged current interactions can be expanded into a series of local operators, whose contributions are weighted by the effective coupling constants. In the SM, the dimension-6 operators can be classified in 6 categories. In the notation of [17], the ones which play a dominant role in the phenomenology of weak decays of B mesons are given as follows:

Current-Current Operators (Figure 1.2(a))

$$\mathcal{Q}_1 = (\bar{s}_{\alpha L}\gamma_\mu c_{\beta L})\,(\bar{c}_{\beta L}\gamma^\mu b_{\alpha L}) \tag{1.17}$$

$$\mathcal{Q}_2 = (\bar{s}_L\gamma_\mu c_L)\,(\bar{c}_L\gamma^\mu b_L) \tag{1.18}$$

QCD-Penguin Operators (Figure 1.2(b))

$$\mathcal{Q}_3 = (\bar{s}_L\gamma_\mu b_L)\sum_{q=u,d,s,c,b}(\bar{q}_L\gamma^\mu q_L) \tag{1.19}$$

$$\mathcal{Q}_4 = (\bar{s}_{\alpha L}\gamma_\mu b_{\beta L})\sum_{q=u,d,s,c,b}(\bar{q}_{\beta L}\gamma^\mu q_{\alpha L}) \tag{1.20}$$

$$\mathcal{Q}_5 = (\bar{s}_L\gamma_\mu b_L)\sum_{q=u,d,s,c,b}(\bar{q}_R\gamma^\mu q_R) \tag{1.21}$$

$$\mathcal{Q}_6 = (\bar{s}_{\alpha L}\gamma_\mu b_{\beta L})\sum_{q=u,d,s,c,b}(\bar{q}_{\beta R}\gamma^\mu q_{\alpha R}) \tag{1.22}$$

Electroweak-Penguin Operators (Figure 1.2(c))

$$\mathcal{Q}_{3Q} = \frac{3}{2}\,(\bar{s}_L\gamma_\mu b_L)\sum_{q=u,d,s,c,b} e_q\,(\bar{q}_R\gamma^\mu q_R) \tag{1.23}$$

$$\mathcal{Q}_{4Q} = \frac{3}{2}\,(\bar{s}_{L\alpha}\gamma_\mu b_{L\beta})\sum_{q=u,d,s,c,b} e_q\,(\bar{q}_{R\beta}\gamma^\mu q_{R\alpha}) \tag{1.24}$$

$$\mathcal{Q}_{5Q} = \frac{3}{2}\,(\bar{s}_L\gamma_\mu b_L)\sum_{q=u,d,s,c,b} e_q\,(\bar{q}_L\gamma^\mu q_L) \tag{1.25}$$

$$\mathcal{Q}_{6Q} = \frac{3}{2}\,(\bar{s}_{L\alpha}\gamma_\mu b_{L\beta})\sum_{q=u,d,s,c,b} e_q\,(\bar{q}_{L\beta}\gamma^\mu q_{L\alpha}) \tag{1.26}$$

Magnetic-Penguin Operators (Figure 1.2(d))

$$\mathcal{Q}_7 = \frac{e}{16\pi^2} m_b \bar{s}_{\alpha L}\sigma^{\mu\nu} b_{\alpha R} F_{\mu\nu} \tag{1.27}$$

$$\mathcal{Q}_8 = \frac{g}{16\pi^2} m_b \bar{s}_{\alpha L}\sigma^{\mu\nu} T^a_{\alpha\beta}\, b_{\beta R}\, G^a_{\mu\nu} \tag{1.28}$$

ΔF = 2 (ΔS = 2 or ΔB = 2) Operators (Figure 1.2(e))

$$\mathcal{Q}(\Delta S = 2) = (\bar{s}_L\gamma_\mu d_L)\,(\bar{s}_L\gamma^\mu d_L) \tag{1.29}$$

$$\mathcal{Q}(\Delta B = 2) = (\bar{b}_L\gamma_\mu d_L)\,(\bar{b}_L\gamma^\mu d_L) \tag{1.30}$$

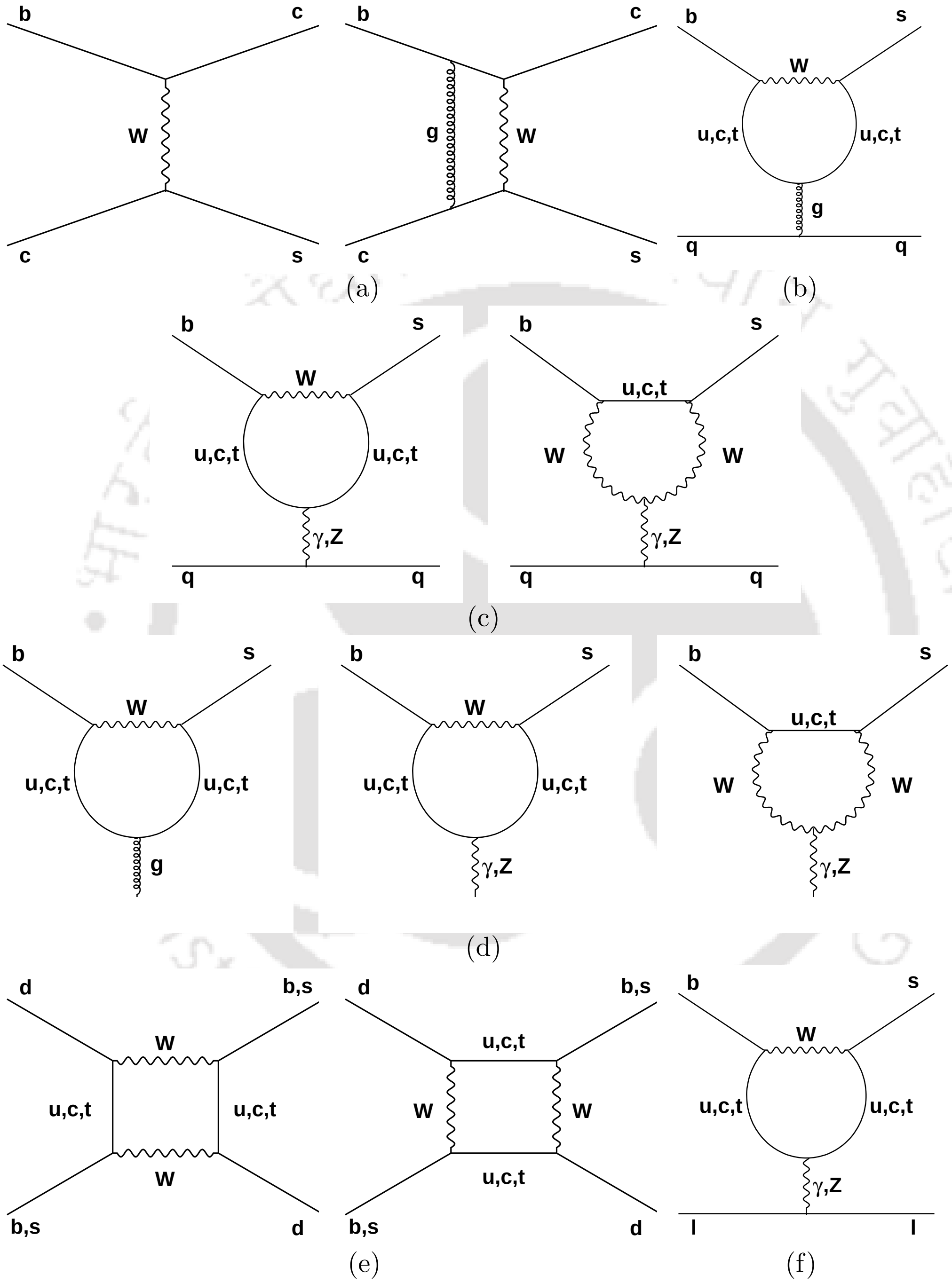

FIGURE 1.2: *Feynman diagram representations of various operators.*
(a) Current-Current (b) QCD Penguins (c) Electroweak Penguins (d) Magnetic Penguins
(e) $\Delta\text{F} = 2$ processes (box processes) and (f) Semi Leptonic Penguin processes.

Semi-Leptonic Operators (Figure 1.2(f))

$$
\begin{aligned}
\mathcal{Q}_9 &= \frac{e^2}{16\pi^2}(\bar{s}_L\gamma_\mu b_L)\,(\bar{l}\gamma^{\mu} l) && (1.31)\\
\mathcal{Q}_{10} &= \frac{e^2}{16\pi^2}(\bar{s}_L\gamma_\mu b_L)\,(\bar{l}\gamma^{\mu}\gamma_5 l) && (1.32)\\
\mathcal{Q}_{\nu\bar{\nu}} &= \frac{\alpha_{em}}{4\pi}(\bar{s}_L\gamma_\mu b_L)\,(\bar{\nu}_L\gamma^{\mu}\nu_L) && (1.33)\\
\mathcal{Q}_{\mu\bar{\mu}} &= \frac{\alpha_{em}}{4\pi}(\bar{s}_L\gamma_\mu b_L)\,(\bar{\mu}_L\gamma^{\mu}\mu_L) && (1.34)
\end{aligned}
$$

where, the subscripts L and R refer to the left and right-handed components of the fermion field given by $q_{L,R} = (1 \mp \gamma_5/2)\,q$. e and g represent the electromagnetic and strong coupling constants (g_1 and g_3), e_q is the electric charge of the relevant quark and $T^a_{\alpha\beta} \equiv \lambda^a_{\alpha\beta}$ (a=1,...8) are the SU(3) color generators, α and β being the color indices. The above set of operators is characteristic for any consideration of the interplay of QCD and electroweak effects. Since the ratio α/α_s ($\equiv 10^{-2}$) of the QED and QCD couplings is very small, electroweak penguins are expected to play a minor role in comparison with QCD penguins.

The effective Hamiltonian arising from this set of operators is usually written as:

$$
\mathcal{H}_{eff} = \frac{G_F}{\sqrt{2}}\sum_i V^i_{\rm CKM}\mathcal{C}_i(\mathcal{R})\mathcal{Q}_i \qquad (1.35)
$$

where the sum runs over all the operators and $V^i_{\rm CKM}$ is the suitable CKM factor (for e.g., $V^*_{ts}V_{tb}$ for the $b \to s$ transitions). The decay amplitude of a process can be written as:

$$
\mathcal{A}(M \to F) = \langle F|\mathcal{H}_{eff}|M\rangle = \frac{G_F}{\sqrt{2}}\sum_i V^i_{\rm CKM}\mathcal{C}_i(\mathcal{R})\,\langle F|\mathcal{Q}_i(\mathcal{R})|M\rangle \qquad (1.36)
$$

where, $\langle F|\mathcal{Q}_i(\mathcal{R})|M\rangle$ is the hadronic matrix element of $\mathcal{Q}_i$ between M and F evaluated at the renormalization scale $\mathcal{R}$.

The Wilson coefficients can be computed by calculating the amplitude for simple processes in both full and effective theories and then comparing them. Since the Wilson coefficients are process independent, the values obtained by matching a specific process can then be used for the calculation of amplitude of other processes. At higher energies, $\mathcal{C}_i$'s can be computed using perturbation theory due to QCD asymptotic freedom. Thus, the Wilson coefficients ($\mathcal{C}_i$'s) at an energy $\mathcal{R}$, can be evaluated by first computing them at a high energy scale (M_W), which can then be evolved through renormalization group (RG) [21–23] equations:

$$\mu\frac{d}{d\mu}\mathcal{C}_k = \gamma_{ki}\mathcal{C}_i \tag{1.37}$$

to low energy scale $\mathcal{R}$. The Wilson coefficients ($\mathcal{C}_i$'s) at energy $\mathcal{R}$, can thus be written as:

$$\mathcal{C}_k(\mathcal{R}) = U_{k,i}(\mathcal{R}, M_W)\mathcal{C}_i(M_W) \tag{1.38}$$

where,

$$U_{k,i}(\mathcal{R}, M_W) = T_g\, exp\left[\int\limits_{g(M_W)}^{g(\mathcal{R})} \frac{\gamma_{ki}(g')}{\beta(g')}\mathrm{d}g'\right] \tag{1.39}$$

is the evolution function which allows to calculate $\mathcal{C}(\mathcal{R})$'s once $\mathcal{C}(M_W)$'s is known. $\mathcal{C}(M_W)$'s are the Wilson coefficients at higher energy scale M_W. T_g is an ordering criterion defined in [21, 24]. $\beta(g) = \mathcal{R}(\mathrm{d}g/\mathrm{d}\mathcal{R}) \equiv \mathrm{d}g/\mathrm{d}(\ln\mathcal{R})$ is the RG function which governs the evolution of g. γ is the anomalous dimension matrix of the operator involved. Keeping the first two terms in the expansions of $\gamma(g)$ and $\beta(g)$, in powers of g, we get:

$$\gamma(g) = \gamma^{(0)}\frac{\alpha_s}{4\pi} + \gamma^{(1)}\frac{\alpha_s^2}{16\pi^2}, \quad \beta(g) = -\beta_0\frac{g^3}{16\pi^2} - \beta_1\frac{g^5}{(16\pi^2)^2}$$

Inserting these expansions in equation 1.39, we obtain:

$$U(\mathcal{R}, M_W) = \left[1 + \frac{\alpha_s(\mathcal{R})}{4\pi}J\right]\left[\frac{\alpha_s(M_W)}{\alpha_s(\mathcal{R})}\right]^P\left[1 - \frac{\alpha_s(M_W)}{4\pi}J\right] \tag{1.40}$$

where,

$$P = \frac{\gamma^{(0)}}{2\beta_0}, \quad J = \frac{P}{\beta_0}\beta_1 - \frac{\gamma^1}{2\beta_0}.$$

The Wilson coefficients will, in general, depend on the masses of the particles, which were integrated out.

The calculation of the operators (and hence the matrix elements) on the other hand require non-perturbative calculations, since they involve long distance contributions. These calculations are mostly done using lattice QCD and some model dependent approaches such as QCD sum rules, hadronic sum rules, $1/N$ expansion (where, N is the number of colors), chiral perturbation theory, large-Nc, etc. All non-perturbative methods have some limitations and hence contribute to large uncertainties in the matrix elements and decay amplitudes. The dominant theoretical uncertainty mostly comes from QCD corrections.

Thus, the decay rate can be written as:

$$\mathcal{A}(M \to F) = \frac{G_F}{\sqrt{2}} \sum_{i,k} V^i_{\text{CKM}} U_{k,i}(\mathcal{R}, M_W) \mathcal{C}_i(M_W) \langle F | \mathcal{Q}_k(\mathcal{R}) | M \rangle \tag{1.41}$$

and its calculation involves three distinct steps:

- Determination of initial conditions of the Wilson coefficients at the electroweak scale.
- Evolution of Wilson coefficients ($\mathcal{C}_i$) by means of RG equations down to $\mathcal{R} = \mathcal{O}(m_b)$.
- Evaluation of hadronic matrix elements of the effective operators at $\mathcal{R} = \mathcal{O}(m_b)$, including both perturbative and non-perturbative QCD corrections.

New physics effects may induce [6]:

- corrections to the Wilson coefficients.
- new operators not present in the SM.
- new sources of mixing not expected in the SM.

Hence, comparison between the experimental and SM predictions can put constraints on them.

1.4 Analysis Methods

For the radiative and electroweak penguin processes, there are 3 approaches to measure the branching fraction (BF). They are: the exclusive reconstruction method [17, 18], the inclusive reconstruction method [17, 18, 25] and the semi-inclusive one [18, 25].

1.4.1 Exclusive Reconstruction Method

A B-meson decaying into an exclusive final state is reconstructed by measuring the energy and momentum of all long lived decay products ($\pi^{\pm}, K^{\pm}, e^{\pm}, \mu^{\pm}$ and γ) and selecting the intermediate states with certain invariant mass. The exclusive reconstruction method has an advantage of having strong kinematic discrimination against the background.

Theoretical calculations of the decay rates for exclusive processes require the calculation of the decay rate into a specific hadronic final state. For semi-leptonic decays, the matrix elements can be factorised into a hadronic and a leptonic current:

$$\mathcal{M} = \langle hl|\mathcal{Q}_j|B\rangle = \left\langle h|\mathcal{Q}_j^H|B\right\rangle . \left\langle l|\mathcal{Q}_j^L|O\right\rangle \tag{1.42}$$

with $\mathcal{Q}_j = \mathcal{Q}_j^H.\mathcal{Q}_j^L$. The matrix element of the leptonic current can be explicitely calculated and the hadronic current is expressed in terms of meson form factors. There are sizeable theoretical (arround 10-20%) uncertainties associated with the hadronic form factors, making the theoretical predictions for exclusive decay rates difficult. As these form factors describe strong interaction effects, they have to be calculated using non-perturbative models like light cone QCD sum rules or vector meson dominance, for each individual configuration of initial and final state. Thus, exclusive decays are more difficult to study than the inclusive ones from theoretical perspective, more so at high energies, when quark and gluon degrees of freedom are more important. The analyses described in this thesis describes exclusive study of $b \to s\gamma$ and $b \to s\gamma\gamma$ modes namely, the $B_s^0 \to \phi\gamma$ and $B_s^0 \to \gamma\gamma$ decays.

1.4.2 Inclusive Reconstruction Method

The $B_{(s)} \to X_s\gamma$ and $B_{(s)} \to X_s l^+ l^-$ decays are distributed over a spectrum, which can be described in terms of photon energy (lepton energy) or recoil hadronic mass (X_s) spectrum. In fully inclusive approach for measuring the $b \to s\gamma$ BF and spectrum, the photon is selected, but the hadronic system (X_s) recoiling against the emitted photon is not reconstructed. X_s includes all accessible final states having a strange quark. Continuum backgrounds are rejected using various event shape varables. Continuum suppression can be improved using laptonic tags, i.e., by reconstructing high energy leptons from the other

B in the event. But this method results in reduced signal statistics. In inclusive method, usually a cut is applied on the E_γ spectrum to exclude the low energy region as this region is populated with large backgrounds. The E_γ spectrum is then divided into bins and binned fits are performed to obtain the values of the BF for each bins. The spectrum can also be used to obtain various observables and theoretical model parameters and for extrapolating the E_γ spectrum. This method introduces model dependence due to the cut on E_γ. Further, it is statistics limited and background rejection is challenging. With large statistics and efficient background rejection techniques, the cut on E_γ can be loosened to reduce the model dependence. To obtain a model independent measurement of BF, full E_γ spectrum is measured with uniform efficiency over the full region.

Theoretically, for calculating the cross-section of an inclusive process, it is usually sufficient to calculate it at the quark-gluon level (by integrating over the full phase-space of quarks and gluons) as they will essentially hadronize to some hadrons and we do not need information about the end-products. Using the principle of quark-hadron duality, optical theorem and perturbation theory, the decay width and amplitude of a $B^0 \to X_s\gamma$ process can be written as:

$$\sum_{F\in X_s} \langle B|\mathcal{Q}|F\rangle \left\langle F|\mathcal{Q}^\dagger|B\right\rangle = \sum_{p} \langle B|\mathcal{Q}|p\rangle \left\langle p|\mathcal{Q}^\dagger|B\right\rangle \tag{1.43}$$

$$\mathcal{A}(B\to X_s) = \frac{G_F}{\sqrt{2}} \sum_{F\in X_s} V^i_{\mathrm{CKM}}\mathcal{C}_i(\mathcal{R}) \langle F|\mathcal{Q}_i(\mathcal{R})|B\rangle \tag{1.44}$$

where, F is any final state having a s quark, where a B meson can decay and the sum over p represents the sum over quarks and gluons. The resulting BF can be written as an expansion in inverse powers of m_b [20] in heavy quark expansion (HQE) as:

$$\mathcal{B}(B\to X_s) = \mathcal{B}(b\to s) + \mathcal{O}(1/m_b^2) \tag{1.45}$$

The leading term in the expansion is modeled by decay of free b quark and corresponds to the matrix element of the free quarks $\langle s|\mathcal{Q}_i|b\rangle$, which can be calculated perturbatively. Corrections due to virtual gluons need to be added. Power corrections ($\mathcal{O}(1/\mathrm{m}_b^2)$) describe the difference between the initial b quarks and B mesons which causes an estimated suppression of the decay rate of the order of 1.5% [26]. There is no correction term linear in $1/\mathrm{m}_b$. This is because there is no dimension-4 gauge-invariant operator that could appear in the HQE [27]. The inclusive measurement method has an advantage of having less theoretical uncertainties than the exclusive one.

1.4.3 Semi-Inclusive Reconstruction Method

In semi-inclusive approach, the photon is selected and a number of exclusive final states (of X_s) are also reconstructed. The aim is to reconstruct as many exclusive modes as possible and then to calculate their sum. Events are required to satisfy the selection criteria of one of the exclusive modes. Due to tighter selection criteria there are less backgrounds as compared to fully inclusive case. Continuum suppression techniques are used to reduce the continuum backgrounds. In semi-inclusive analysis, the recoil hadronic mass spectrum can be measured (instead of the photon spectrum), which can then be converted to an equivalent photon energy spectrum using:

$$E_{\gamma}^{B} = \frac{M_B^2 - M_H^2}{2M_B} \tag{1.46}$$

This allows for a better measurement of the spectrum shape as the hadronic mass (M_H) resolution can be an order of magnitude better than the photon energy spectrum. A binned study of the hadronic mass spectrum can be done (similar to the fully inclusive case) to obtain the values of the partial BF for the reconstructed final states. An estimate of the inclusive $b \to s\gamma$ BFs can then be made by calibrating the spectrum with the fraction (f) of the reconstructed final states. The corrected spectrum can be fitted to obtain various theoretical model parameters by extrapolating over the full range. This method is more model dependent than the fully inclusive case and has large uncertainties due to limited understanding of the distribution of X_s final states. Background suppression is still a problem, but lesser than that in inclusive case. Moreover, this method has lesser theoretical uncertainty than the exclusive reconstruction method.

1.5 The Exclusive Decays $B_s^0 \to \phi\gamma$ and $B_s^0 \to \gamma\gamma$

The primary aim of this thesis is to measure the BF of the decay $B_s^0 \to \phi\gamma$ and to search for the decay $B_s^0 \to \gamma\gamma$. $B_s^0 \to \phi\gamma$ and $B_s^0 \to \gamma\gamma$ are exclusive $b \to s\gamma$ and $b \to s\gamma\gamma$ penguin processes, which are sensitive to physics beyond the SM. The leading order Feynman diagrams for these processes are shown in Figure 1.3. Since these decays proceed via the operator representation $\mathcal{Q}_7$ shown in Figure 1.2(d), so they are sensitive to it [17, 18]. Thus, precise measurements of BF of these decays along with other $b \to s\gamma$ decay processes may help to put stringent constraints on the permitted values of Wilson coefficients $\mathcal{C}_7$ and $\mathcal{C}_7'$, which in turn may constrain various new-physics model parameters. $\mathcal{C}_7$ and $\mathcal{C}_7'$ are Wilson coefficients corresponding to the magnetic penguin operator $\mathcal{Q}_7$ and its chirality flipped counterpart $\mathcal{Q}_7'$. The present constraints on Wilson coefficients $\mathcal{C}_7$ and $\mathcal{C}_7'$ obtained using various decay modes are summarized in Figure 1.4 [28, 29]. Further, a measurement of $B_s^0 \to \gamma\gamma$ could be a useful test of the hadronic dynamics and for λ_B, which plays an important role for other exclusive B-decays [30].

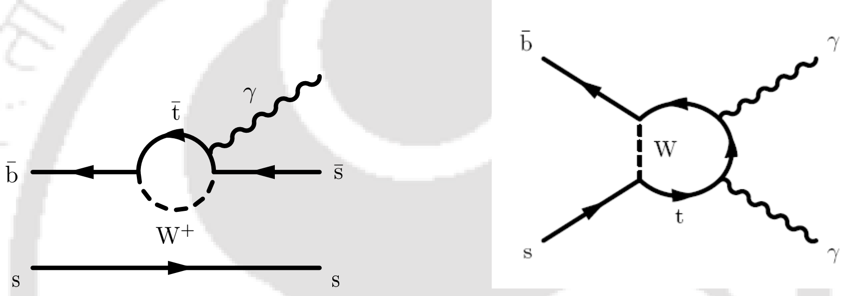

FIGURE 1.3: *Leading order Feynman diagrams for the decays (a)* $B_s^0 \to \phi\gamma$ *and (b)* $B_s^0 \to \gamma\gamma$.

The BF of a decay is the probability of a particle to decay into that particular mode. It can be expressed as:

$$\mathcal{B}(\text{Decay Mode}) = \frac{\Gamma_{\text{Decay Mode}}}{\Gamma_{\text{Total}}} \tag{1.47}$$

where, $\Gamma_{\text{Total}} = \hbar/\tau_{B_s}$ is the total decay width of a B_s meson, τ_{B_s} being the B_s lifetime in seconds.

Theory calculations of $B_s^0 \to \phi\gamma$ BF within the SM framework yields a value between (3.9 - 4.3) $\times 10^{-5}$ with about 30% uncertainty [31, 32]. First observation of this decay was made by the Belle collaboration using 23.6 fb^{-1} of data collected at the $\Upsilon(5S)$ resonance and its BF was measured to be $(5.7^{+2.2}_{-1.9}) \times 10^{-5}$ [33]. Until recently, this result containing large uncertainties was the only experimental result available for $B_s^0 \to \phi\gamma$. Recently the LHCb collaboration has measured $\mathcal{B}(B^0 \to K^{0*}\gamma)/\mathcal{B}(B_s^0 \to \phi\gamma)$ and using the world average value of the BF for $B^0 \to K^{0*}\gamma$ [34], the BF for $B_s^0 \to \phi\gamma$ is estimated to be $(3.5 \pm 0.4) \times 10^{-5}$ [35]. These experimental results are in good agreement with

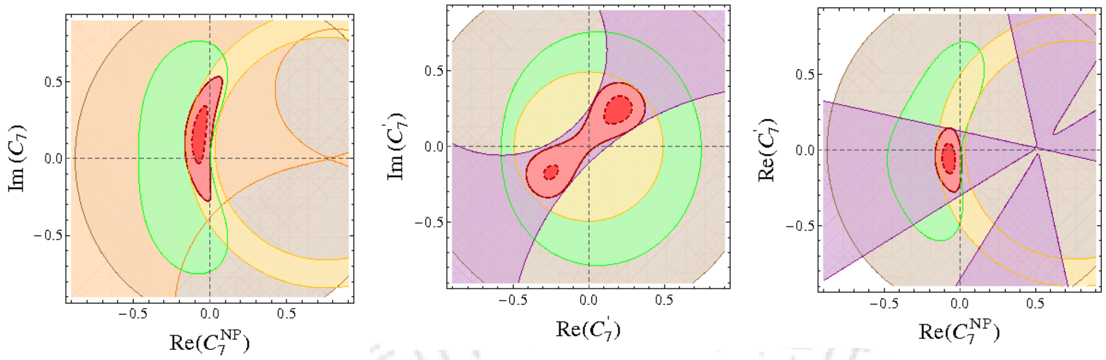

FIGURE 1.4: *Present 2σ constraints on the complex plane of* $\mathcal{C}_7$.
Constraints from $\mathcal{B}(B \to X_s\gamma)$ *is represented with yellow,* $B \to K^*\mu^+\mu^-$ *at high* q^2 *with green,* $B \to X_s l^+ l^-$ *by brown,* $B \to K^*\gamma$ *with purple and combined 1 and 2* σ *constraints with red [28, 29].*

the theory results. Moreover, the BF for $B_s^0 \to \phi\gamma$ is constrained by a good agreement between theory and experimental results on $b \to s\gamma$ rates [31, 32, 34, 36] and on inclusive $B^0 \to X_s\gamma$ rates [34, 37–39]. Studies done in the context of various new physics models indicate small changes in the central value of its BF [40, 41]. So, possible new physics effects will remain hidden within the large uncertainties of this mode. With 5 times more statistics that is available to us compared to the previous Belle analysis [33], our result on $B_s^0 \to \phi\gamma$ will have lesser uncertainties and is expected to complement the LHCb results. Precise theory results are required to rule out the (small) new physics contributions, that are still possible in this channel.

The decay $B_s^0 \to \gamma\gamma$ is yet to be observed and its upper limit (UL) at 90% confidence level (CL) is estimated to be 8.7 $\times 10^{-6}$ [33]. This result is still an order of magnitude larger than the SM expectations, which lie within the range (0.18 - 1.0) $\times 10^{-6}$ [30, 42, 43]. $B_s^0 \to \gamma\gamma$ BF is also constrained by $B^0 \to X_s\gamma$ results in the R-parity conserving scenerio. However, in R-parity violating SUSY case, presence of λ-irreducible diagrams [44] may increase its BF by more than an order of magnitude [40]. These λ irreducible diagrams are irrelevant to $b \to s\gamma$ amplitude at one loop, and thus have a negligible effect on the single photon decay $B^0 \to X_s\gamma$ [40]. Thus, though the small size of Belle data-set makes the observation of $B_s^0 \to \gamma\gamma$ signal unlikely in the SM framework, there is still a possibility to observe an evidence of this decay in the presence of new physics. This decay will possibly be observed in Belle `II` in near future. With sufficient statistics and precise theory results on these channels, several new physics models may be ruled out or further constrained.

1.6 Chapter Summary

In this chapter, we have introduced the SM of particle physics and the associated gauge transformations. The CKM matrix, the GIM mechanism and FCNC processes are then discussed. Renormalization theory, EFT and various analysis techniques are then introduced briefly. A brief summary and discussion on the current experimental and theory status of the decays $B_s^0 \to \phi\gamma$ and $B_s^0 \to \gamma\gamma$ are also presented in this chapter.

Chapter 2

The Belle Experiment at KEKB

The Belle experiment is a high energy e^+e^- collider experiment located at the High Energy Accelerator Research Organization (KEK) in Tsukuba, Japan and run by an international collaboration of more than 400 physicists and engineers from over 16 countries. Belle was designed and optimized for the observation of CP violation in the B meson system [45] by tuning the accelerator to the CM energy of various Υ(nS) resonances [46]. In 2001, Belle (along with BaBar, a B-physics experiment at Stanford Linear Accelerator Center, California) observed large CP asymmetries in B-decays, consistent with the Kobayashi Maskawa mechanism [47]. Study of rare decays was also one of the primary motivations of the Belle experiment. Large solid angle coverage, excellent vertexing and high precision electromagnetic calorimetry allowed the Belle detector to make important contributions in charm physics, tau physics, hadron spectroscopy, searches of exotic particles and two photon physics. In this chapter, we discuss about the Υ(nS) resonances, the KEKB accelerator, the Belle detector, data acquisition system, trigger, processing and skimming of the data sample.

2.1 Υ(nS) Resonances

The Υ(nS) (with n $= 1, 2, 3, \ldots$) resonances are quasi-bound states of a b-quark and its anti-quark having masses in the range 9 GeV/c^2-11 GeV/c^2. The lightest Υ(nS) resonance, the Υ(9460) or Υ(1S), was first observed in proton-nucleon collisions in 1977, by the CFS (Columbia-Fermilab-Stony Brook) E288 collaboration [48] at Fermilab and subsequently confirmed at DESY and Cornell [49]. Later its mass, width and J^{PC} values were determined. Its J^{PC} value is measured to be 1^{--}. Figure 2.1 shows the Υ(nS) resonance production spectrum as a function of the e^+e^- collision energy. A majority of e^+e^- collisions result in lighter $q\bar{q}$ states such as $u\bar{u}$, $d\bar{d}$, $s\bar{s}$, $c\bar{c}$ or lepton pairs. These events are generally known as continuum events. At the first three resonances, the Υ(nS) system can only decay with the annihilation of b and $\bar{b}$ as shown in Figure 2.2.

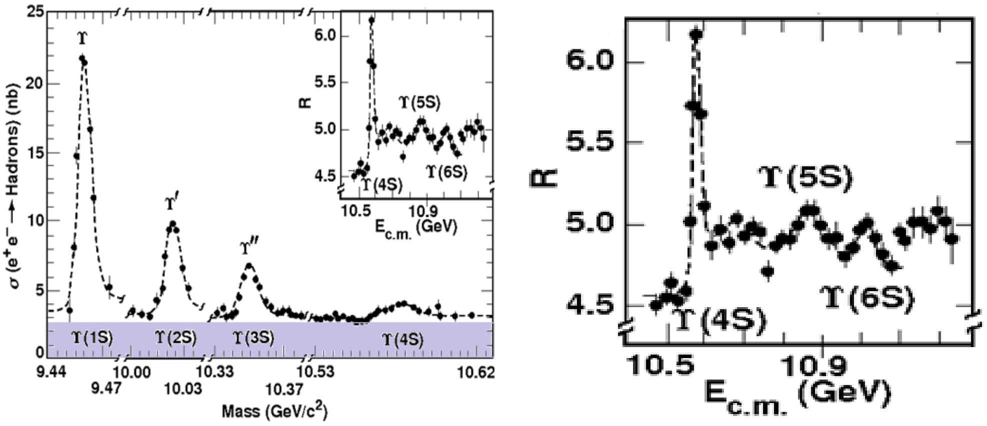

(a) (b)

FIGURE 2.1: *The hadronic cross-section for* Υ(nS) *resonances as a function of* e^+e^- *CM energy: in (a) nb and (b) normalized to theoretical muon-pair cross-section. Results of CUSB Collaboration.*

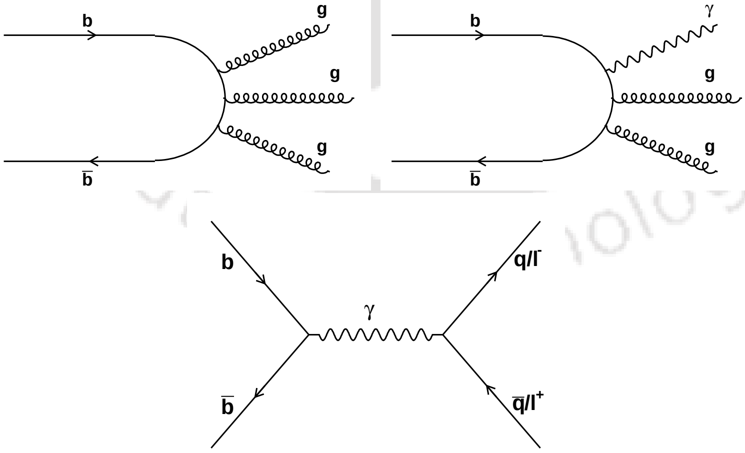

FIGURE 2.2: *Decay processes of* Υ(nS) *system at first 3 resonance states.*

The mass of the fourth resonance, called the $\Upsilon(4\mathrm{S})$ with a mass of 10.56 GeV is just few MeV ($\sim$ 20 MeV) above the mass of two B mesons. Therefore, it is the lightest Υ resonance state that can decay into $B\bar{B}$ pairs. In fact, it decays almost exclusively ($> 96\%$) to $B^+\bar{B}^-$ and $B^0\bar{B}^0$ pairs [50]. The $\Upsilon(4\mathrm{S})$ decay rate to $B^+\bar{B}^-$ is measured to be almost equal to the rate of $B^0\bar{B}^0$ [34]. The $\Upsilon(4\mathrm{S})$ mass is too small to produce excited B^* mesons or to create an extra particle. The B mesons are essentially at rest at the $\Upsilon(4\mathrm{S})$ frame. The $b\bar{b}$ production cross-section at $\Upsilon(4\mathrm{S})$ is about 1.1 nb.

The discovery of $\Upsilon(5\mathrm{S})$ resonance (in 1985) [51] and the production of B_s^0 mesons at this resonance (in 2005) [52] was established by the CLEO collaboration. The $\Upsilon(5\mathrm{S})$ mass is substantially larger than the $B_s^0\bar{B}_s^0$ production threshold. Thus, the variety of hadronic events at $\Upsilon(5\mathrm{S})$ resonance as shown in Figure 2.3 is richer than that at the $\Upsilon(4\mathrm{S})$ CM energy. The $b\bar{b}$ production cross-section $\left(\sigma_{b\bar{b}}^{\Upsilon(5\mathrm{S})} = \sigma(e^+e^- \to b\bar{b})\right)$ at the $\Upsilon(5\mathrm{S})$ resonance is more than three times smaller than that at $\Upsilon(4\mathrm{S})$ resonance [53]. Using 121.4 fb^{-1} of $\Upsilon(5\mathrm{S})$ data its value is estimated to be 0.340 ± 0.016 nb, by subtracting $e^+e^- \to q\bar{q}$ ($q = u, d, s, c$) component obtained just above the $\Upsilon(4\mathrm{S})$ resonance [53, 54]. The $b\bar{b}$ pairs can hadronize to produce three categories of events:

- events containing 2 strange B i.e., B_s mesons ($e^+e^- \to B_s^{(*)}\bar{B}_s^{(*)}$)
- events containing 2 non-strange B mesons ($e^+e^- \to B^{(*)}\bar{B}^{(*)}(X)$)
- events containing no $B_{(s)}$ mesons ($e^+e^- \to \mathrm{non} - B_{(s)}\bar{B}_{(s)}$)

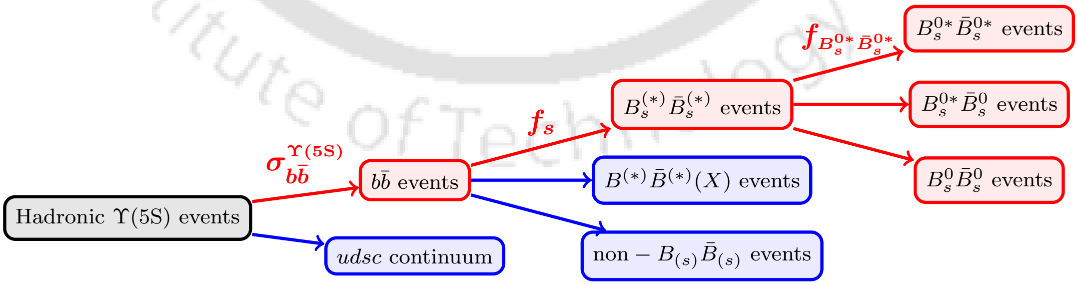

FIGURE 2.3: *Hadronic events at* $\Upsilon(5\mathrm{S})$.

The production fraction of $b\bar{b}$ events that hadronize to $B_s^{(*)}\bar{B}_s^{(*)}$ $\left(f_s = \dfrac{\sigma(e^+e^- \to B_s^{(*)}\bar{B}_s^{(*)})}{\sigma(e^+e^- \to b\bar{b})}\right)$ is determined by the relations:

$$\frac{\mathcal{B}(\Upsilon(5\mathrm{S}) \to D_s X)}{2} = f_s \mathcal{B}(B_s \to D_s X) + (1 - f_s)\mathcal{B}(B \to D_s X) \tag{2.1}$$

$$\frac{\mathcal{B}(\Upsilon(5\mathrm{S}) \to D^0 X)}{2} = f_s \mathcal{B}(B_s \to D^0 X) + (1 - f_s)\mathcal{B}(B \to D^0 X) \tag{2.2}$$

through a measurement of the inclusive rates $\mathcal{B}(\Upsilon(5\mathrm{S}) \to D_s(D^0)X)$ and information of the inclusive BF of the decays $B_s(B) \to D_s(D^0)X$ [53]. The value of f_s is measured to be $(17.2 \pm 3.0)\%$ [54]. $b\bar{b}$ produced at $\Upsilon(5\mathrm{S})$ can hadronize to 3 modes with B_s^0 pairs, $\Upsilon(5\mathrm{S}) \to B_s^{0*}\bar{B}_s^{0*}$, $\Upsilon(5\mathrm{S}) \to B_s^{0*}\bar{B}_s^0$ and $\Upsilon(5\mathrm{S}) \to B_s^0\bar{B}_s^0$. Their relative abundances, measured using $B_s \to D_s\pi$ [54, 55], are found to be:

$$f_{B_s^{0*}\bar{B}_s^{0*}} = \frac{\sigma(e^+e^- \to B_s^{0*}\bar{B}_s^{0*})}{\sigma(e^+e^- \to B_s^{(*)}\bar{B}_s^{(*)})} = (87.0 \pm 1.7)\% \tag{2.3}$$

$$f_{B_s^{0*}\bar{B}_s^{0}} = \frac{\sigma(e^+e^- \to B_s^{0*}\bar{B}_s^{0})}{\sigma(e^+e^- \to B_s^{(*)}\bar{B}_s^{(*)})} = (7.3 \pm 1.4)\% \tag{2.4}$$

$$f_{B_s^{0}\bar{B}_s^{0}} = 1 - f_{B_s^{0*}\bar{B}_s^{0*}} - f_{B_s^{0*}\bar{B}_s^{0}} \tag{2.5}$$

B_s^0-mesons are also produced from excited states of B_s^{0*} with low energy photon de-excitation. Figure 2.4 shows the leading order Feynman diagram governing the creation of a pair of B and B_s mesons at $\Upsilon(5\mathrm{S})$ resonance.

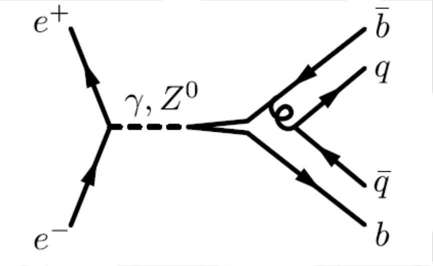

FIGURE 2.4: *Leading order Feynman diagram for an e^+e^- annihilation producing a $B_{(s)}$ meson pair at $\Upsilon(5\mathrm{S})$ resonance.*

2.2 The KEKB Accelerator

The KEKB [56] is an asymmetric energy e^+e^- collider located in a 11 *m* deep and 3 *km* long tunnel that was previously used for the TRISTAN experiment [57]. It was designed for producing large number of B meson pairs with a design luminosity of 1.0×10^{34}

$cm^{-2}sec^{-1}$ (or 10 $nb^{-1}sec^{-1}$). It consists of 2 storage rings: a high energy ring (HER) for electrons and a low energy ring (LER) for positrons, and a linear accelerator (LINAC). Electron beam is generated by evaporating electrons off the filament and the positrons are produced by firing an offshoot of the electron beam onto the target that produces electron-positron pairs. The electron and positron beams are then accelerated to the desired energies before injecting them to the storage rings. The two beams move in the opposite directions and collide at the interaction point (IP) where the Belle detector is located. The energies are tuned such that the CM energy equals the mass of the Υ(nS) resonances. A schematic layout of the accelerator can be seen in Figure 2.5. The two beams do not collide head-on but with a small crossing angle of 22 *mrad*. The non-zero crossing angle reduces the luminosity and also the CM energy by about 1 MeV (0.01%); but it is simpler to achieve than a 0 degree collision angle, and also substantially reduces background from synchrotron radiation. To cope with the luminosity loss, the bunches are tilted since January 2007 by two superconducting radio frequency cavities known as crab cavities [58], installed in each ring to collide the bunches with a maximum overlap as shown in Figure 2.6.

The CM energy ($\mathrm{E_{CM}}$) of the colliding beam is given by

$$\sqrt{s} = 2\sqrt{\mathrm{E_{HER}} \times \mathrm{E_{LER}}} \tag{2.6}$$

At Belle, most of the data is taken at Υ(4S) resonance. To produce Υ(4S) resonance, the electron and positron beams are kept at $\mathrm{E_{HER}}$ = 8.0 GeV and $\mathrm{E_{LER}}$ = 3.5 GeV. Due to asymmetric beam energies, the Υ(4S) quasi-bound state particles are produced with a Lorentz boost of

$$\beta\gamma = \frac{\mathrm{E_{HER}} - \mathrm{E_{LER}}}{\mathrm{E_{CM}}} = 0.425 \tag{2.7}$$

along the electron beam direction (z-axis) with respect to the laboratory frame. The typical B meson decay length of 20 μm $\Big($$B$ mesons are nearly at rest in the Υ(4S) CM frame, since, the mass difference $\mathrm{m}(\Upsilon(4\mathrm{S})) - \mathrm{m}(B\bar{B})$ is small$\Big)$ is dilated to $\beta\gamma c\tau_B \sim$ 200 μm ($\tau_B \sim 1.5psec$) by the Lorentz boost. The distance between the decay vertices of the two B mesons (Δz) can be measured with a vertex detector having a resolution of 100 μm. Thus, the use of asymmetric beam energies at B factories allows us to infer the

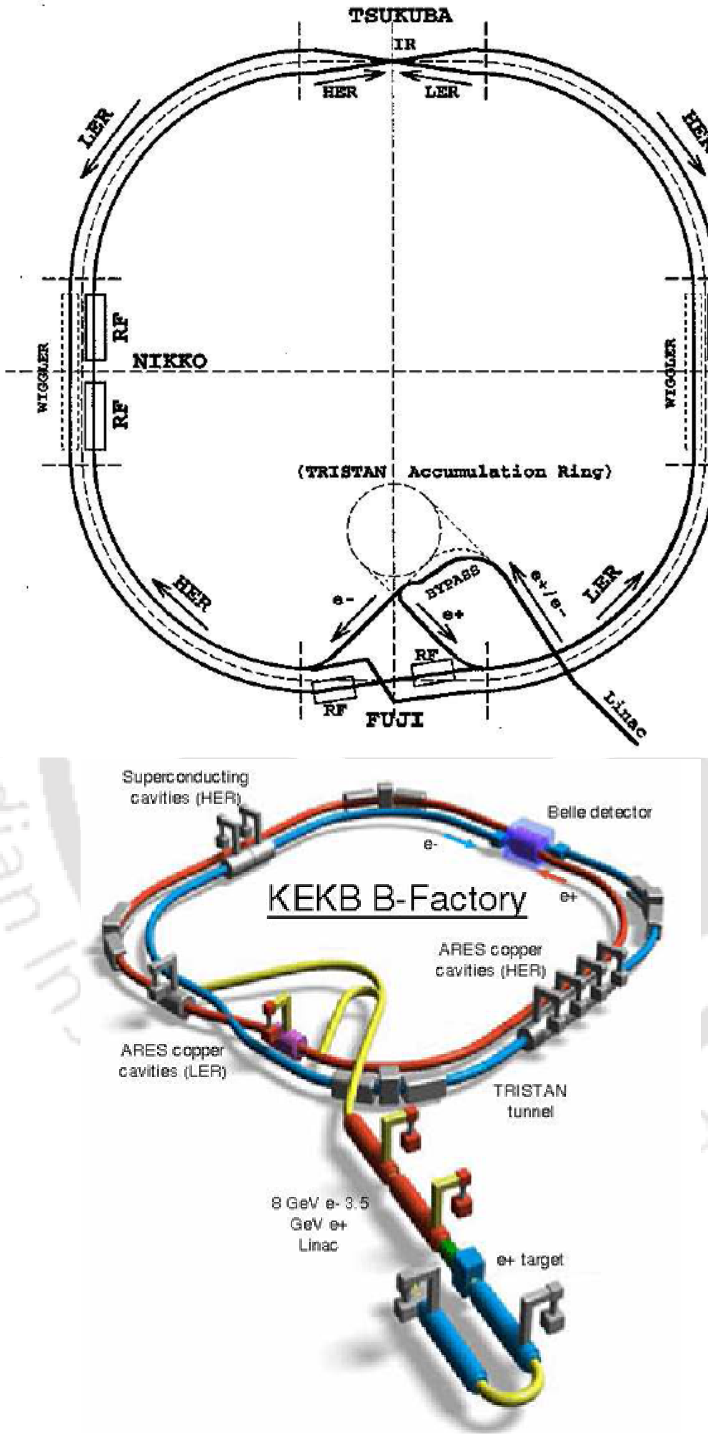

FIGURE 2.5: *The KEKB accelerator.*

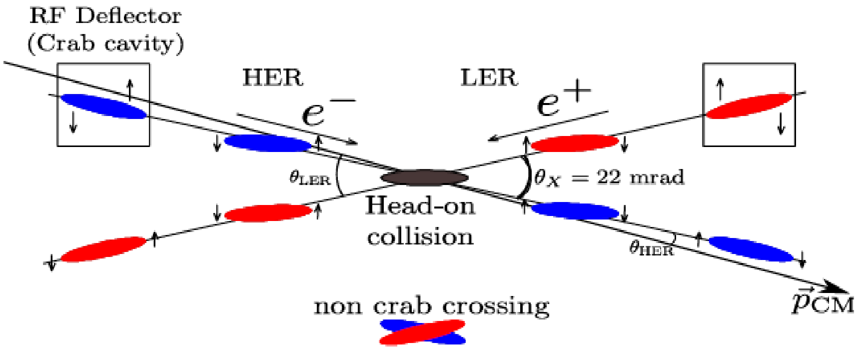

FIGURE 2.6: *Crab crossing of bunches.*

decay time difference between the two B mesons as:

$$\Delta t = \frac{\Delta z}{\beta\gamma c} \tag{2.8}$$

Thus, the boost provides the opportunity to perform time dependent CP violation measurements.

The KEKB accelerator was stopped after 11 years of successful operation from 1999 to 2010. During its operation, the Belle detector had accumulated data with an integrated luminosity (L_{int}) of more than 1 ab^{-1}, which was one of the primary goal set at the inception of the project [45]. About 711 fb^{-1} of data has been taken at the $\Upsilon(4S)$ energy. In addition, the Belle experiment has accumulated about 121 fb^{-1} of data at $\Upsilon(5S)$, 3 fb^{-1} of data at $\Upsilon(3S)$, 24 fb^{-1} of data at $\Upsilon(2S)$ and about 6 fb^{-1} of data at $\Upsilon(1S)$ resonance.

2.3 The Belle Detector

Located at the IP, the Belle detector [59] is a general purpose 4π detector composed of many sub-detectors. It is designed to detect the final state decay products of B meson decays, namely the kaons, pions, muons, photons and electrons. The basic parameters that are measured using the Belle detectors are momentum, energy and particle identity (PID). Position and momentum of the charged particles are measured using the magnetic spectrometer and the energy is measured using the electromagnetic calorimeter. PID information is gained through a combination of measurements of energy loss, mass and penetration depth in several sub-detectors. The sub-detectors that make up the Belle detector are:

- silicon vertex detector (SVD)
- central drift chamber (CDC)
- aerogel Cherenkov counter (ACC)
- time-of-flight scintillation counter (TOF)
- electromagnetic calorimeter (ECL)
- K_L^0 and muon detector (KLM)
- extreme forward calorimeter (EFC)

The entire detector is housed inside a 1.5 *Tesla* solenoidal magnet which causes the charged particles to move in a helical path. The detector is shown in Figure 2.7. Each of the sub-detectors are described in more details in the following subsections.

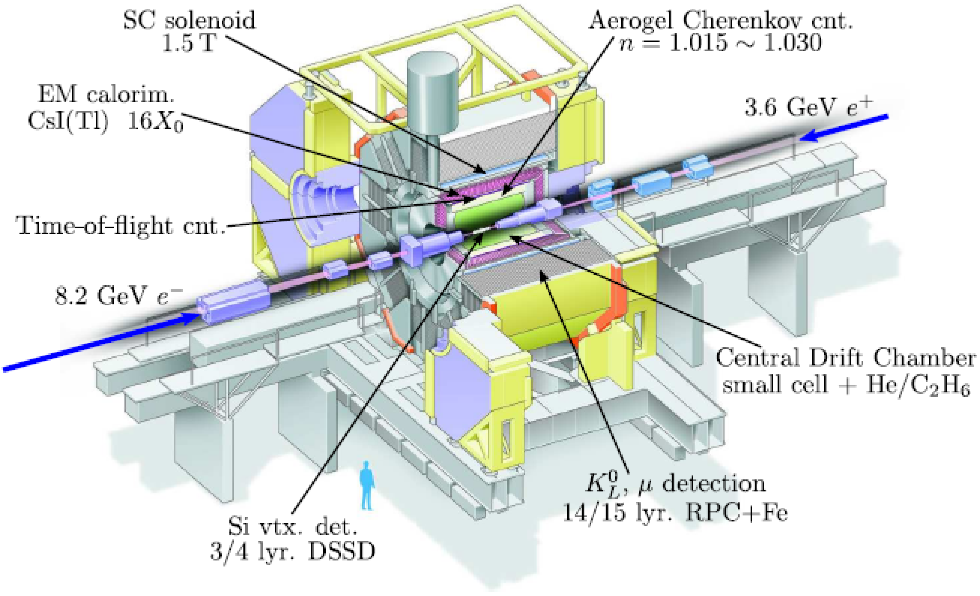

FIGURE 2.7: *The Belle detector.*

Coordinate System Used in the Belle Detector: It is important to define the coordinate system used in the Belle detector to assist in describing each of the sub-detectors. Figure 2.8 defines the coordinate system. The origin is defined as the position of the nominal IP. The positive z-axis is along the direction of the electron beam. The y-axis is vertical to the x-axis. The x-axis is horizontal and points radially outward. The radial distance is defined as $\mathrm{r} = \sqrt{\mathrm{x}^2 + \mathrm{y}^2}$. The polar angle θ is defined with respect to the z-axis and ϕ is the azimuthal angle with respect to the x-axis. The Belle sub-detectors are asymmetric in z. This is best illustrated by the coverage of the polar angle θ, as shown in Table 2.1.

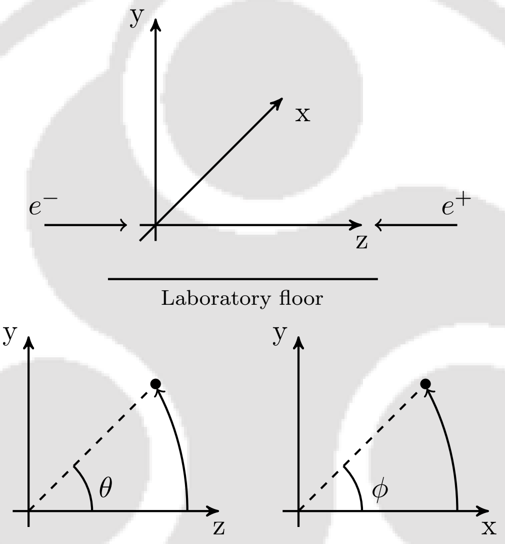

FIGURE 2.8: *Coordinate system used in the Belle detector.*

Region	**Polar angle (θ) coverage**
Barrel	$34^\circ < \theta < 127^\circ$
Forward endcap	$17^\circ < \theta < 34^\circ$
Backward endcap	$150^\circ < \theta < 127^\circ$

TABLE 2.1: *Polar angle coverage of the barrel and endcap regions.*

2.3.1 Beam Pipe and the Silicon Vertex Detector (SVD)

The beam pipe maintains the accelerator vacuum. KEKB has two beam pipes, one for LER and one for HER, which merge at the IP. It is made up of a double walled beryllium cylinder having radii 20 mm and 23 mm as shown in Figure 2.9. Both walls are only 0.5 mm thick and made of low Z material to reduce Coulomb scattering which is the main limiting factor on the z-vertex position resolution. The two walls are separated by a 2.5 mm gap. Helium gas is circulated between the walls to dissipate the heat. Cooling is important to operate the SVD close to the interaction point to improve the vertex resolution. To reduce the low energy X-ray background the beam pipe is surrounded by 20 μm thick gold foil.

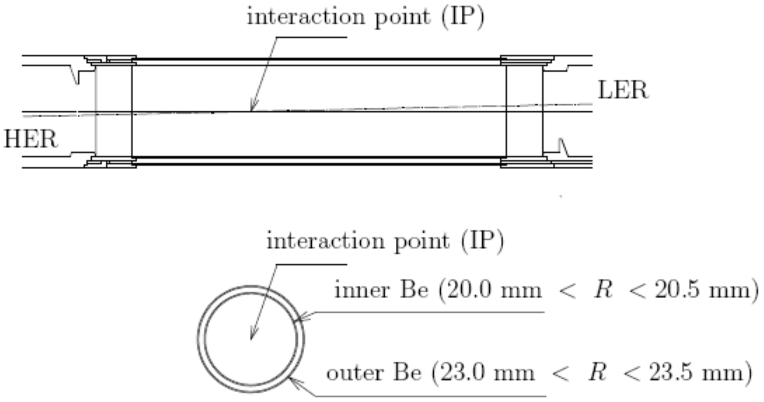

Figure 2.9: *Cross-sectional and side view of the beam pipe.*

The SVD is the innermost sub-detector in the Belle detector and is used to precisely reconstruct the B-decay vertices close to the IP. It can measure z-vertex position of B-decays with a precision of 100 μm. This is vital for time-dependent CP violation study where precise measurement of z position of B meson decays is required. The SVD also helps with tracking for low energy particles. Two different SVD's have been used in Belle. The first version (SVD1) has been used during 1999 to July, 2003 and the second version (SVD2) since October, 2003. During the SVD upgrade process, the beam pipe was replaced by a beam pipe having its inner and outer radii 15 mm and 16.25 mm, respectively. The thickness of the surrounding gold foil was also changed to 10 μm. This replacement allowed the SVD2 to be closer to the IP and therefore provide better vertex resolution. The data used in this analysis was taken using SVD2. Therefore, we describe only SVD2 in this thesis.

The configuration of SVD2 is shown in Figure 2.10. It consists of 4 concentric layers arranged on a cylindrical structure at radii 20 mm, 43.5 mm, 70 mm and 88 mm from the IP. It covers the angular region $17^\circ < \theta < 150^\circ$. SVD2 consists of 138 double sided silicon strip detectors (DSSD) and 110592 readout channels. SVD2 is described in more details in [60]. A DSSD is essentially a depleted p-n junction. A charged particle passing through the junction liberates electrons from the valence band into the conduction band creating electron-hole pairs. These pairs create currents in the p^+ and n^+ strips located on the surface of DSSD. The p^+ strips are aligned along the beam axis and therefore measure the azimuthal angle ϕ. The n^+ strips are aligned perpendicularly to the beam axis and measure z. Each DSSD has 1280 sense strips and 640 read-out pads on each side. The size of the sensor is $57.5 \times 33.5\ mm^2$. A schematic diagram of DSSD is shown in Figure 2.11

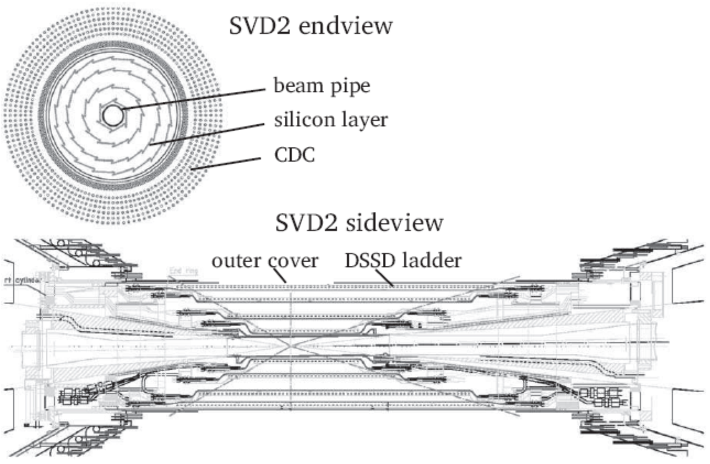

FIGURE 2.10: *Cross-sectional view (top) and side view (bottom) of SVD2.*

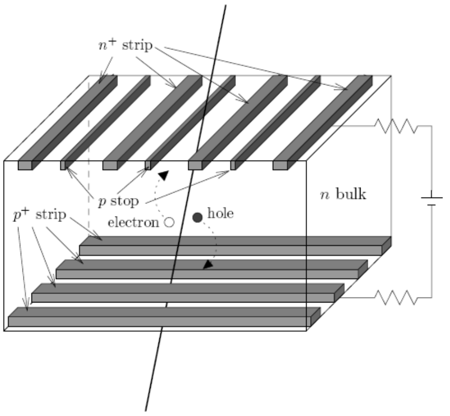

FIGURE 2.11: *Schematic diagram of DSSD.*

2.3.2 Central Drift Chamber (CDC)

The CDC is a tracking detector, used to measure the momenta and energy losses (dE/dx) of charged particles passing through it. It thus helps in particle identification. Figure 2.12 (a) shows the structure of the CDC. It is cylindrical about the beam pipe and asymmetric in the z direction in order to provide the angular coverage of $17^\circ < \theta < 150^\circ$. The CDC has 50 cylindrical layers of anode wires, which consists of 32 axial and 18 stereo wire layers, and three cathode strip layers. In summer of 2003, the inner three layers have been replaced by two small cell layers for making the space for SVD2. The axial wires are parallel to the z-axis and provide transverse momentum ($\mathrm{p_T}$) information, while the stereo wires slant to the z-axis and provides z position information. It consists of 8400 (8464) drift cells for SVD1 (SVD2) configuration. Each cell shown in Figure 2.12(b) consists of eight negatively biased field wires and one positively biased sense wire. It is filled with a low Z gas mixture (equal parts of helium and ethane) to minimise the multiple Coulomb scattering. The large ethane component provides a good dE/dx resolution. A charged particle passing through the CDC ionizes the gas. The electrons accelerate and produce further ionization. Thus, a charge avalanche is caused by the ionized gas which drifts towards the oppositely charged sense wires with a specific drift velocity. The measured signal height and drift time provides information of the energy deposit and distance from the sense wire. The 1.5 *Tesla* magnetic field produced by the solenoidal magnet causes the charged particles to follow in a helical path. A helix is defined by 5 independent parameters [61]:

- the signed curvature of the helix providing charge and $\mathrm{p_T}$ information.
- the pitch of the helix providing information about the longitudinal momentum ($\mathrm{p_z}$).
- the three-dimensional coordinates of the helix reference point called the pivot.

The pivot is chosen as the wire position of the innermost hit in the CDC. Track parameters are improved by combining the CDC track information with that of SVD. Using information from both the detectors, we obtain:

$$\left(\frac{\sigma_{\mathrm{p_T}}}{\mathrm{p_T}}\right)^2 (\%) = (0.19\ \mathrm{p_T})^2 + 0.34^2 \tag{2.9}$$

$$\sigma_{\mathrm{xy}}^{2} = 19^{2} + \left(\frac{50}{\mathrm{p}\beta\sin^{3/2}\theta}\right)^{2}\mu m^{2} \tag{2.10}$$

$$\sigma_{\mathrm{z}}^{2} = 36^{2} + \left(\frac{54}{p\beta\sin^{5/2}\theta}\right)^{2}\mu m^{2} \tag{2.11}$$

where, $\sigma_{\mathrm{p_T}}$, σ_{xy} and σ_{z} are the $\mathrm{p_T}$, xy and z resolutions. Since, the energy loss (dE/dx) depends on β i.e., v/c, particles with same momenta but different masses can be easily distinguished by plotting (dE/dx) as a function of particle momentum as shown in Figure 2.13. The (dE/dx) resolution was measured to be 7.8% in the momentum range from 0.4 to 0.6 GeV/c. It provides K/π separation up to 0.8 GeV/c and also in the region of relativistic rise (above 2.5 GeV/c). CDC is described in more details in [62].

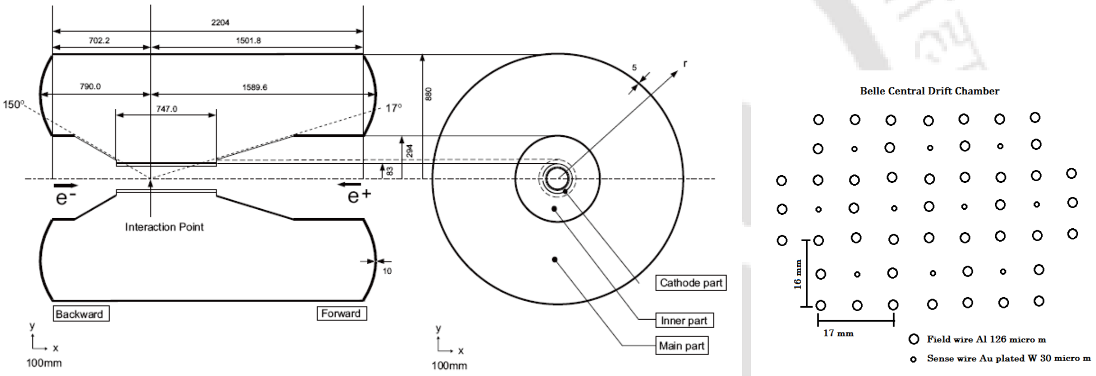

(a) (b)

FIGURE 2.12: *(a) Structure of CDC and (b) its cell structure.*

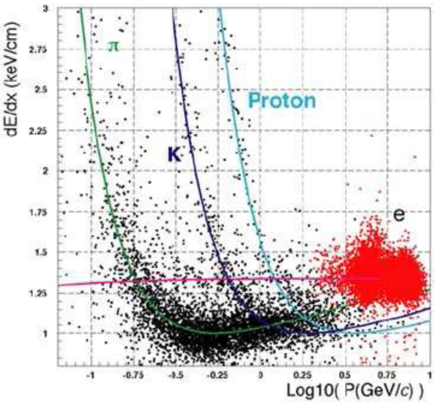

FIGURE 2.13: dE/dx *vs. momentum for pions, kaons, protons and electrons. dE/dx is used in the particle-ID algorithm.*

2.3.3 Aerogel Cherenkov Counter (ACC)

The ACC is used to distinguish particles that have similar momenta but different masses, and hence different velocities, for e.g., pions and kaons produced in B-decays. It is mostly used to distinguish particles in the momentum range of $1.2 < \text{p} < 3.5$ GeV/c. It works on the principle that a particle moving faster than light inside a medium ($\text{v}_{\text{light}} = c/n$) emits Cherenkov light where, n is the refractive index (RI) of the medium. Thus, the threshold energy for a particle to emit Cherenkov radiation in a medium with a fixed RI depends on the particle velocity. Therefore, simultaneous measurements of the momentum of the charged particle in the CDC allows to identify the various charged particles in the ACC.

The ACC is composed of 960 counter modules segmented into 60 cells in ϕ for the barrel part and 228 modules arranged in 5 concentric layers for the forward endcap. All the counters are arranged in a semi-tower geometry, covering a total polar angle range of 17° to 127°. The ACC modules are made of five tiles of silica aerogel stacked in a thin aluminium box of size $12 \times 12 \times 12\ cm^3$. The RI's of the aerogel in the barrel region were chosen based on the polar angles and ranges between 1.010 to 1.028. The aerogel of the endcaps have a RI of 1.030. This is done to optimize the K/π separation as the average momenta varies with polar angle. The Cherenkov light is fed to the light guides and detected by two mesh photomultiplier tubes attached to those boxes. The ACC correctly distinguishes between pions and kaons between 80% to 95% of the time. The

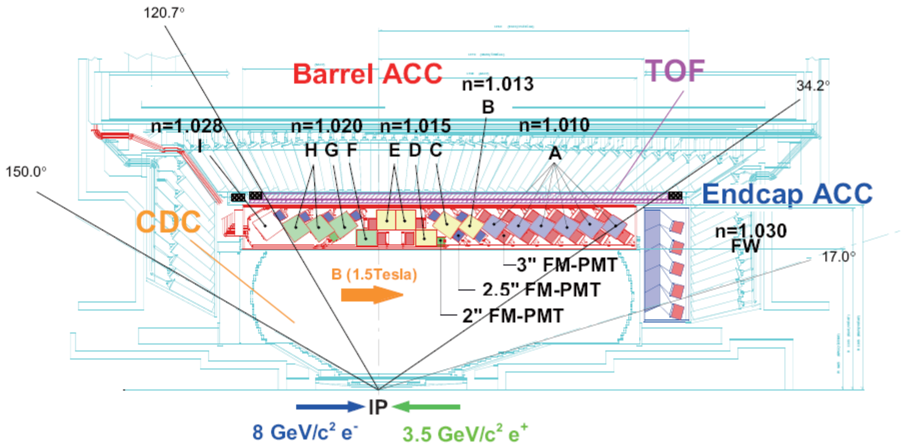

FIGURE 2.14: *Schematic diagram of ACC.*

schematic diagram of the Cherenkov counter and its modules are shown in Figure 2.14 and Figure 2.15 respectively. The ACC is described in more details in [63].

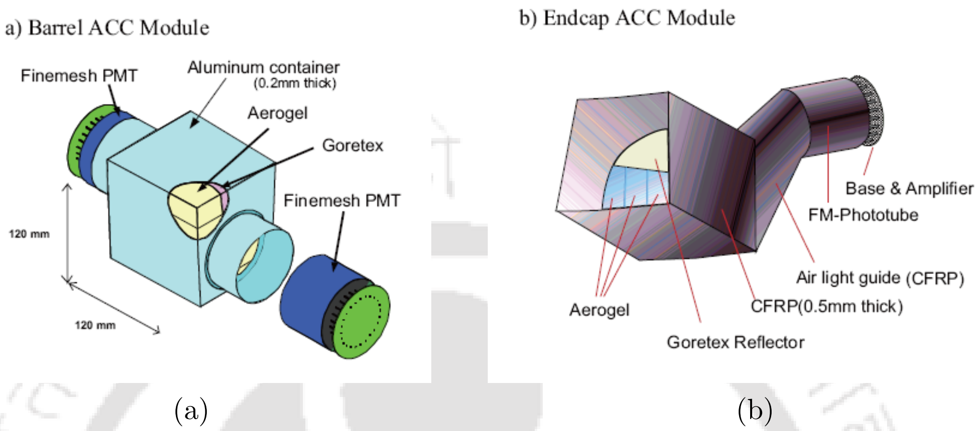

(a) (b)

FIGURE 2.15: *(a) Barrel and (b) endcap ACC module.*

2.3.4 Time of Flight Counters (TOF)

The TOF detector system provides additional particle identification. It is located just outside the ACC at a distance of about 128 *cm* from the IP. It helps to distinguish charged kaons from pions for momentum below 1.2 GeV/c with more than 2 standard deviations. It is composed of 128 TOF counters and 64 trigger scintillation counters (TSC). Two TOF counters and one TSC form one module, as shown in Figure 2.16. The TOF system has an angular coverage of $33^\circ < \theta < 121^\circ$. When a high energy charged particle or a photon passes through the scintillator, Cherenkov radiation is emitted. Each TOF counter is read out by a fine-mesh photomultiplier tube (FM-PMT) at each end. Each TSC counter is read out by only one FM-PMT from the backward end. The TOF counters provide fast timing signals for the trigger system together with the TSCs to generate gate signals for analog-to-digital (ADC) converters and stop signals for time-to-digital (TDC) converters. The signal of a particle crossing the TSC is used in coincidence with the two adjacent TOF counters to create a trigger signal. The TSCs are used for keeping the fast trigger below a reasonable rate (70 KHz). The counters measure the elapsed time between a collision at the IP and the time when the particle hits the TOF layer with a time resolution of 100 *psec*. The information of time of flight (T) measured using the TOF counter and momentum (p) measured using SVD and CDC provides a measure of the mass of the particle as given in equation 2.12 and hence the particle identity.

$$m = \frac{p}{c}\sqrt{\left(\frac{cT}{L}\right)^2 - 1} \tag{2.12}$$

where, L is the flight length. Given the size of the magnetic field, a charged particle needs to have a momentum larger than 0.54 GeV/c to reach the TOF counter. Above that limit, TOF measurement is included in the algorithm for particle identification. Figure 2.17 shows the mass of the tracks including TOF and CDC signals. There is a good agreement between simulation (with 100 *psec* time of flight resolution) and data. TOF system is described in more details in [64]

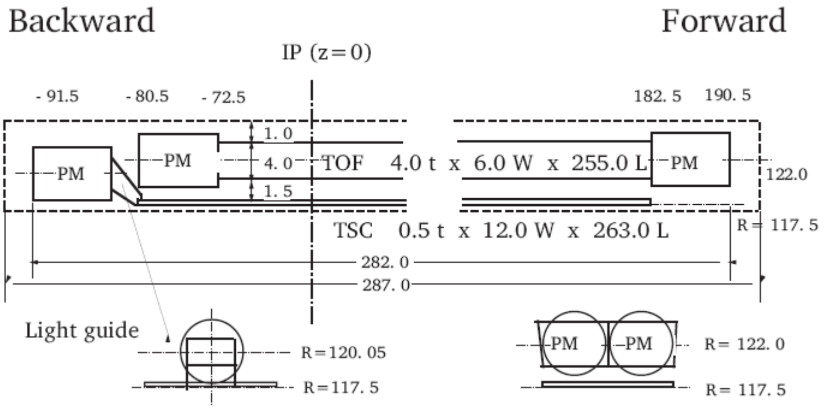

FIGURE 2.16: *Schematic diagram of TOF module.*

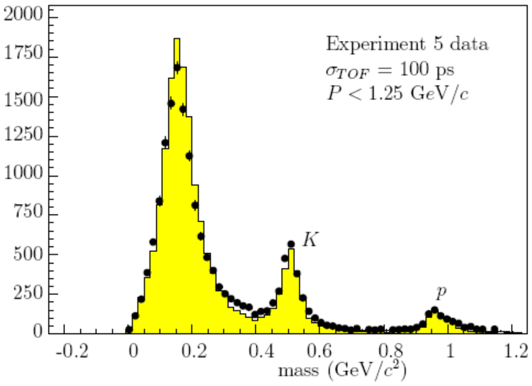

FIGURE 2.17: *Hadron mass distribution calculated from TOF measurements below 1.2 GeV/c. Well-separated clear peaks from pions, kaons and protons are seen.*

2.3.5 Electromagnetic Calorimeter (ECL)

The ECL is used for the efficient detection of electrons and photons from B meson decays over a large energy range, with good resolution in energy and position. The ECL measures the energy deposited by electromagnetic showers. The configuration of the ECL is shown in Figure 2.18. It consists of 8,736 thallium doped CsI crystal counters distributed over three sections: the forward endcap section consisting of 1152 crystals and covering $12.4^\circ < \theta < 31.4^\circ$, the barrel section consisting of 6,624 crystals and covering $32.2^\circ < \theta < 128.7^\circ$ and the backward endcap section consisting of 960 crystals and covering $130.7^\circ < \theta < 155.1^\circ$. The scintillator material is selected on the basis of several properties like large photon yield, crystal transparency to its radiation, short decay constant and mechanical stability. The barrel is 3 m in length having an inner and outer radius of 1.25 m and 1.64 m respectively. The endcaps are 0.4 m thick and are located at z = +2.0 m and z = -1.0 m from the IP. The crystals are tower shaped with a front face of 55 $mm \times 55$ mm, a rear face of 65 $mm \times 65$ mm and a length of 30 cm (approximately 16.2 radiation lengths). The crystal size is a compromise between position determination and energy resolution. Crystals having smaller cross-section would enhance the position resolution at the cost of energy resolution.

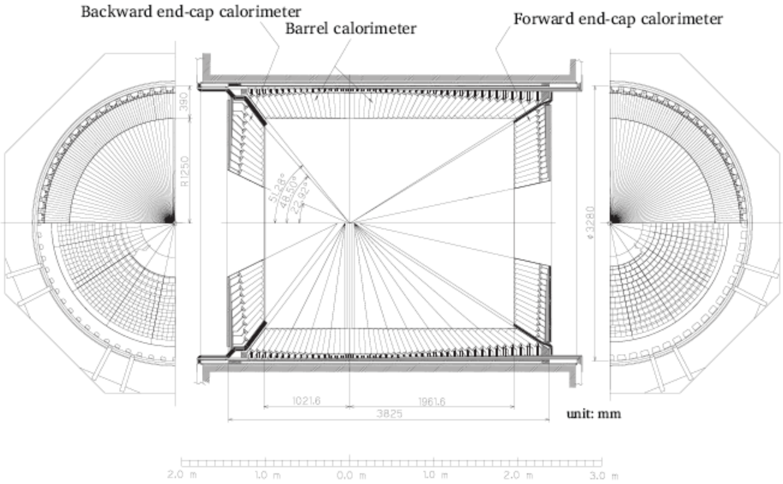

FIGURE 2.18: *Schematic diagram of ECL.*

High energy electrons and photons entering the calorimeter interacts with the CsI(Tl) crystals and deposits energy in the detector. Thus, they initiate an electromagnetic shower through subsequent bremsstrahlung and electron pair production processes followed by

Coulomb scattering. As a result, all the incident energy is absorbed as ionization or excitation in the calorimeter. Other particles only deposit small amounts of energy via dE/dx ionization. The scintillation light of each crystal is readout via a pair of silicon PIN photodiodes and a preamplifier mounted at the end of each crystal.

The angular coverage of the ECL is same as that of CDC, allowing charged tracks to be matched with clusters of hits at CDC. Electrons can be identified by comparing the energy deposited in the crystal with the momentum of a matched track. The difference in energy deposites in the calorimeter is used to distinguish electrons from charged pions and muons. Pions and muons deposit much less energy than electrons having the same momentum in the ECL. Photons can be identified by an ECL shower with no matching track from the CDC and a shower profile consistent with an electromagnetic shower. The position and energy resolution of ECL as a function of the photon energy E (in GeV) are given by:

$$\sigma_{\text{position}} = \left(0.27 + \frac{3.4}{\sqrt{\text{E}}} + \frac{1.8}{\sqrt[4]{\text{E}}}\right) mm \tag{2.13}$$

$$\frac{\sigma_{\text{E}}}{\text{E}}(\%) = \left(\frac{0.066}{\text{E}}\right)^2 + \left(\frac{0.81}{\sqrt[4]{\text{E}}}\right)^2 + 1.34^2 \tag{2.14}$$

where, the first term contains contribution from the electronic noise and the higher order terms mostly arise due to incomplete containment of the electromagnetic shower in the crystals. It also includes systematic effects such as the uncertainty in the calibration of the light output from the crystals. The ECL is described in more details in [65].

2.3.6 Extreme Forward Calorimeter (EFC)

The EFC is used to detect electromagnetic showers in the extreme forward and backward regions: $6.4^\circ < \theta < 11.5^\circ$ and $163.3^\circ < \theta < 171.2^\circ$, respectively. Its solid angle coverage allows it to improve the sensitivity of the processes such as $B^+ \to \tau^+\nu_\tau$ and to provide tagging information for $\gamma\gamma$ physics. It is further used as a beam mask to reduce radiation backgrounds to the CDC, as a beam monitor for KEKB and for luminosity measurements at Belle. The EFC's proximity to the beam pipe and the IP results in its higher backgrounds than the ECL. Bismuth Germanate (Bi4Ge3O12 or BGO) is used as the crystal material for EFC due to its higher radiation tolerance and excellent energy resolution ((0.3-1.0)%/$\sqrt{\text{E}}$ GeV) . The typical cross-section of a crystal is about 2×2 cm^2. The crystals are housed in a bucket shaped stainless steel container. Each part of the detector is segmented into 32 azimuthal and 5 polar sections. The scintillation light is collected by the photodiodes. A three-dimensional view of the EFC is shown in the Figure 2.19. The EFC is described in more details in [66].

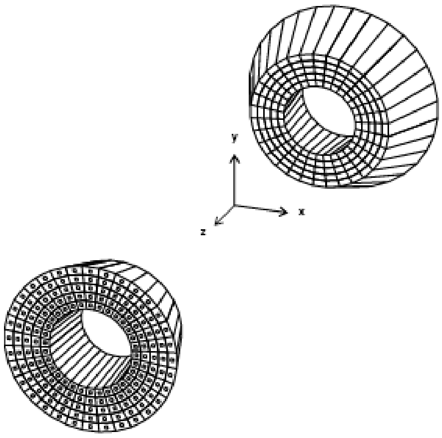

FIGURE 2.19: *Arrangement of crystals composing the EFC.*

2.3.7 K_L^0 and Muon Detector (KLM)

The K_L^0's and muons are long lived particles and deposit very small amount of energy in the previously mentioned subdetectors. The purpose of KLM is to identify them with high efficiency over a broad momentum range greater than 600 MeV/c. The KLM is a very dense and massive detector consisting of alternate layers of charged particle detectors (glass resistive plate counters, RPC [67]) and iron plates (4.7 cm thick) as shown in Figure 2.20. The KLM has 15 detector layers and 14 iron layers in the barrel part ($45° < \theta < 125°$), and 14 detector layers in each of the forward and backward endcaps region ($20° < \theta < 155°$). The iron plates provide 3.9 interaction length of material. The iron layers also serve as a return yoke for the magnetic flux provided by the superconducting solenoid. KLM layers are grouped in superlayers. A superlayer is made up of θ and ϕ cathode strips surrounding two RPCs. The RPCs consist of two parallel-plate electrodes separated by a gas-filled gap. An ionizing particle travelling through the gap creates a local discharge that is read out via external cathode pickup strips, which determines the location and time of ionization. Typical value of spatial resolution of the superlayers is few centimeters.

Hadrons produce hadronic shower when interacting with the iron, thereby allowing for position detection through the RPC's. However, no useful measurement of its energy is possible because of the fluctuations of this shower. The neutral K_L^0 meson can be identified through a hadronic shower with no matching track from the CDC. The muons penetrate through the detector and interact via electromagnetic interaction. The hits in the RPC's allow for its energy and position measurements. Other charged particles, such as pions and kaons are stopped in the system and can easily be separated from muons. Further, muons form narrower clusters than hadrons. Typical muon identification efficiency for muons of momenta above 1.5 GeV/c is 90% with a fake rate of around 2%. The KLM detector is described in more details in [68].

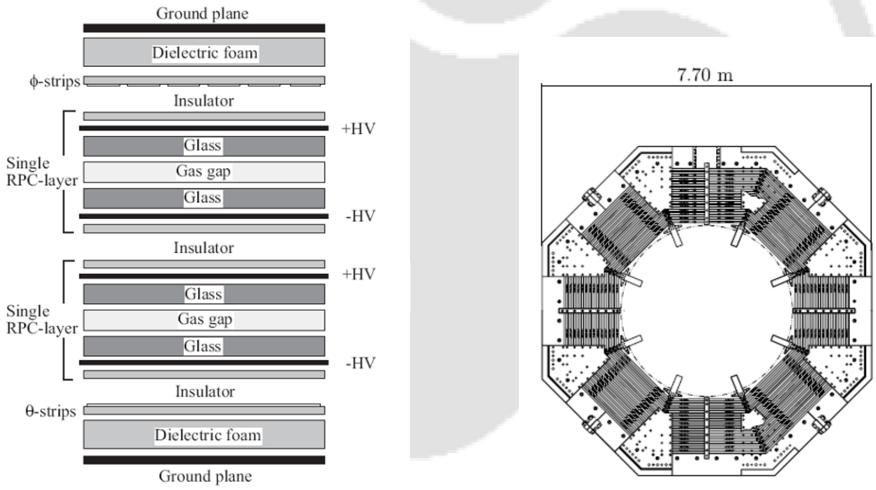

(a) (b)

FIGURE 2.20: *(a) Schematic diagram of KLM detector and (b) an RPC module.*

2.4 Trigger and the Data Acquisition System (DAQ)

An important part of the Belle experiment is the trigger and the data aquisition system (DAQ). A significant number of events that can be detected at the Belle detector are not the result of an e^+e^- collision and are not of interest for physics analysis, for example: e^+e^- scattering, interactions between the beams and the residual gas, interactions with the material of the beam pipe, synchrotron radiation, cosmic ray events, etc. The purpose of the trigger is to reject the uninteresting events and to forward the interesting ones to the DAQ with high efficiency and within a very short decision time. The events of interest at Belle are primarily the hadronic events containing B mesons, photon induced events like Bhabha scattering ($e^+e^- \to e^+e^-$) and μ pair events ($e^+e^- \to \mu^+\mu^-$), which are used for luminosity monitoring and detector calibration. The Belle detector can trigger upto a rate of 500 Hz. The schematic diagram of Belle trigger system is shown in Figure 2.21.

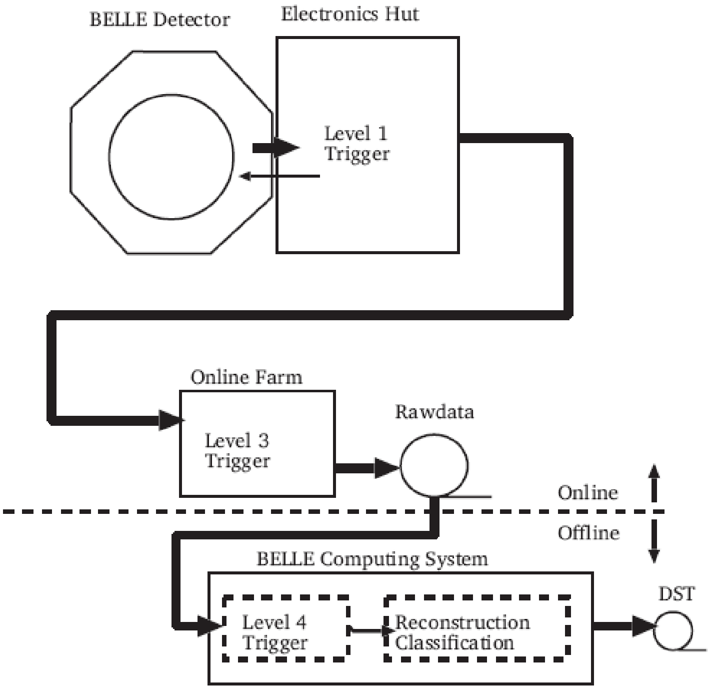

FIGURE 2.21: *Overview of the Belle trigger system.*

The trigger rates for various processes of interaction at the peak luminosity of 10^{34} $cm^{-2}sec^{-1}$ are listed in Table 2.2. The Belle trigger system consists of a Level 0 trigger which is basically a prompt timing signal from the TOF that puts the SVD into the hold state, a Level-1 hardware trigger, a Level-3 software trigger and a Level-4 trigger, which runs offline and performs background reduction. The Belle trigger system is described in more details in [69, 70]. The DAQ collects raw signal data from the sub-detectors and stores them to the data storage system for offline event reconstruction and analysis.

Source	**Rate(Hz)**
$\Upsilon(4S) \to B\bar{B}$	12
Hadron production from continuum	28
$e^+e^- \to \mu^+\mu^-$ and $e^+e^- \to \tau^+\tau^-$	16
$e^+e^- \to e^+e^-$ and $e^+e^- \to \gamma\gamma$ (prescaled by 100)	5
Two photon processes ($p_T > 0.3$ GeV/c)	35
Beam background	O(100)
Cosmic ray background	20

TABLE 2.2: *The trigger rates for various processes at a luminosity* $10^{34} cm^{-2} sec^{-1}$

2.4.1 Level-1 Trigger

A schematic diagram of the Level-1 (L1) hardware trigger system is shown in Figure 2.22. It consists of subdetector trigger systems and a central trigger system called the Global Decision Logic (GDL). The subdetector triggers are based on track or energy information and are grouped into two categories: track triggers and energy triggers. The CDC and the TOF provide trigger signals from charged particles. The CDC provides r-ϕ and r-z trigger signals. The TOF trigger system provides an event timing signal and provides information on the hit multiplicity and back-to-back topology. The ECL provides trigger signals based on the total deposited energy and the number and timing of ECL cluster hits. The KLM provides trigger signals based on the muon hits and the EFC triggers are used for tagging the Bhabha and two photon ($e^+e^- \to \gamma\gamma$) events. A random trigger, which helps to understand the background is also included. Information from the SVD is not used in the L1 trigger system. The GDL receives subdetector triggers within 1.85 μsec after the collision and issues a decision on the event type, 2.2 μsec after the collision. The hardware trigger is described in more details in [69]. The Level-1 trigger is over 99% efficient for hadronic events, such as $B\bar{B}$.

The Level-1.5 trigger is used in conjunction with SVD to reject beam-gas events characterized by vertices far away from the IP. The trigger uses SVD information available 25.6 μsec after the collision, hence too late for the Level-1 decision. The purpose of the trigger is therefore to abort the readout system, which generally takes 50 μsec. The Level-1.5 trigger therefore reduces the dead time significantly. The Level-1.5 trigger is described in details in [70].

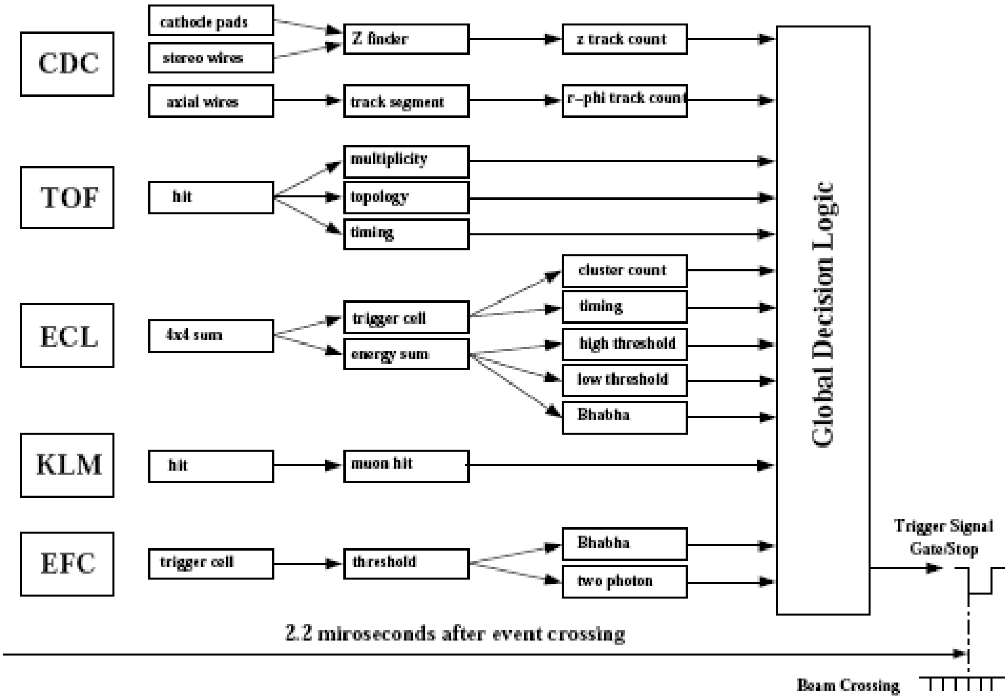

FIGURE 2.22: *Overview of Belle Level-1 trigger system.*

2.4.2 Level-3 Trigger

The Level-3 (L3) trigger is a software trigger which implements a fast track-finding algorithm and rejects events having no tracks with z impact parameter less than 5 *cm* and having total energy deposit in ECL less than 3 GeV. It selects hadronic events with high efficiency ($> 99\%$) and rejects $50\% - 60\%$ of L1 events. Events passing the L3 trigger are saved as raw data.

2.4.3 Data Acquisition System

After the L1 hardware trigger is issued, the DAQ system collects data from the various subdetectors. The DAQ is segmented into 7 subsystems running in parallel, each handling data from a subdetector. This data collection runs in parallel to increase the overall DAQ rate, allowing events to be recorded at up to 500 Hz. The signal from most of the subdetectors go through a charge-to-time (Q-to-T) converter and are finally readout by a TDC. The exceptions are the SVD and KLM, which use flash ADCs and direct TDC readout, respectively. Data from the subsystems is collected and converted to event by event data through an event builder. The event builder output is then sent to the online computing farm, where an event filtering is applied after the fast event reconstruction (L3 trigger). The data transfer rate is about 15 MB/*sec*. The events to be recorded are then written out to the offline storage system via optical fibers. The DAQ is shown in Figure 2.23

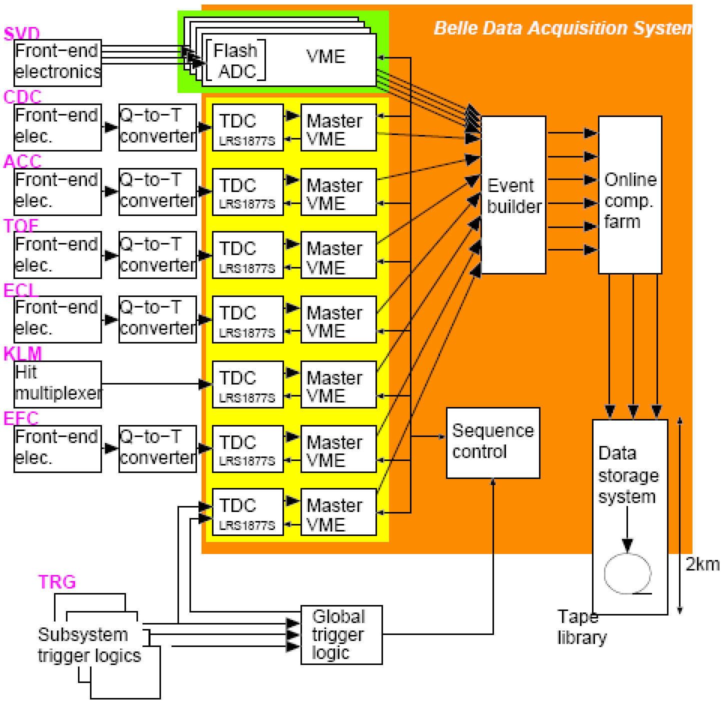

FIGURE 2.23: *Overview of the Belle DAQ.*

2.4.4 Level-4 Trigger and Software for Data Processing

A final, Level-4 (L4) trigger is applied offline on the raw data, further reducing the background by a factor of roughly five and maintaining the hadronic event efficiency. It requires events with more than 4 GeV of energy deposited in the ECL and with at least one track with p_T larger than 300 MeV/c and impact parameters r $<$ 1 *cm* and z $<$ 4 *cm*. It rejects approximately 78% of triggered events while keeping nearly all the hadronic events.

Raw data is then processed and converted into physics data. The tracks of charged particles are reconstructed from the hits measured by CDC. The associated hits to each track are sought in the SVD, ACC, TOF, ECL and KLM. Hits in the ECL and KLM without any associated tracks are assumed to be caused by neutral particles, e.g., photons or K_L mesons. Various software tools are used to determine and apply calibration corrections for each subsystem (e.g., alignment constants, gain variations, etc.) and to measure the momentum or energy of the detected particles. For charged tracks, a helix fit is performed to derive the momentum, and the track is extrapolated to the particle identification (PID) systems to search for associated information. For neutrals, the ECL or KLM can provide information on their energy and/or their direction of flight. Four momentum vectors are then assigned to each charged and neutral particles, and the particle identification likelihoods are determined. All these information related to particle identification is stored in data summary tapes (DST's) in the PANTHER file format [71, 72] suitable for final analysis by collaborators. The data size is further reduced for specific physics processes e.g., hadronic, Bhabha, μ pair, etc in a process called skimming and the skimmed data is stored in Mini-DST (MDST) files [73]. These include only the information needed for physics analysis. The typical size of a hadronic event saved in mini-DST format is 30 KB. The analyses presented in this thesis, involves the study of B mesons and utilises 'Hadron$B(J)$' skim, i.e., events passing the so-called Hadron$B$ [74] requirement or the J/Ψ selections. Data samples are usually further reduced for specific purposes with tighter skimming criteria and the location of the qualified events, saved into index files. This procedure largely reduces the amount of data to be analysed. The analyses are performed in a C++ framework called Belle Analysis Software Framework (BASF).

2.5 Skimming

A set of loose selection criteria are applied to the total data set in order to produce a subset of the data sample, called skimmed dataset that reduces the time required to process and analyze the sample. The skimmed data becomes the working dataset and the subsequent analysis is based on that sample. To minimise the adverse affects on the true events in the total dataset, the selection criteria are usually loose. Furthermore, the set of the skim selection criteria are relatively non-complex so as to minimise the time required to complete a skim, and also to minimise unexpected systematic error contributions.

2.6 Chapter Summary

In this chapter we have described the physics at Υ(nS) resonances, KEKB accelerator, the Belle detector, trigger system and the DAQ used for data collection.

Chapter 3

Signal Reconstruction and Event Selection

This chapter provides a description of the analysis strategy, the Belle datasets, Monte Carlo (MC) event generation procedure and the blind analysis technique used to search for the decays $B_s^0 \to \phi\gamma$ and $B_s^0 \to \gamma\gamma$. The skim, candidate and signal selection criteria are also described in details in this chapter. Event shape variables for both MC signal and background data are fed to an event classifier (NeuroBayes) to reject the dominant backgrounds arising from light quark production ($e^+e^- \to u\bar{u}, d\bar{d}, s\bar{s}, c\bar{c}$) processes. This chapter describes the event shape variables and event classification technique in details. Contribution from possible peaking backgrounds are also studied and discussed in details in this chapter.

3.1 Analysis Strategy

We perform a blind analysis by optimizing the signal selection criteria and parameterizing the signal and background shapes using MC samples of signal and background processes. The steps that we follow in these analyses can be summarized as follows:

- Perform a blind analysis, since the decay modes studied in this thesis are very rare. Very few signal events are expected in the entire dataset used in these analyses.

Blind analysis is a technique in which the physics result is kept hidden by blinding the signal region, until the analysis is fully completed. This is done to avoid experimenter's bias in selecting the selection criteria to select the signal over the background. Blind analysis is described in details in [75, 76].

- Pre-identify all the possible backgrounds.
- Generate signal MC samples for both the modes to optimize the signal selection and to study the signal shape. Study the dedicated background MC samples for parameterizing the background.
- Reconstruct B_s^0 signal candidates with loose pre-selection criteria.
- Validate the analysis tools by reproducing the results of the previous $B_s^0 \to \phi\gamma$ and $B_s^0 \to \gamma\gamma$ analyses. This involves applying the same selection criteria and following the same procedure as the previous one.
- Optimize the selection criteria using MC samples.
- Use event shape variables as inputs to an event classifier to reject the continuum backgrounds.
- Perform an unbinned extended multi-dimensional maximum likelihood fit to extract the signal and background yields.
- Use $B^0 \to K^{0*}\gamma$ as a control sample to correct for possible data-MC differences in $M_{\rm bc}$ and ΔE resolutions.
- Use results from $B_s^0 \to D_s\pi$ analysis done at Belle with the same Υ(5S) sample to make corrections for the B_s^{0*} mass uncertainty in $M_{\rm bc}$. Use mean corrections from $B_s^0 \to \phi\gamma$ to correct the ΔE mean for $B_s^0 \to \gamma\gamma$.
- Estimate the statistical and systematic uncertainties.
- Compute the signal significance both with and without systematics.
- Calculate the BF if a significant signal is observed.
- Estimate its UL, otherwise.

3.2 Datasets

In this section we will describe the datasets that are used to search for both $B_s^0 \to \phi\gamma$ and $B_s^0 \to \gamma\gamma$ decays.

3.2.1 Data Samples

The search for the decays discussed in this thesis are based on 121.4 fb^{-1} Υ(5S) data sample accumulated by the Belle detector, which corresponds to 14.2×10^6 B_s^0 events coming from $B_s^{0*}\bar{B}_s^{0*}$ decays. We have also used 562.2 fb^{-1} Υ(4S) data events to reconstruct the $B^0 \to K^{0*}\gamma$ mode, which is used as a control sample for calibration purposes, described in details in Chapter 4. Control samples are generally created from decays with higher BF and with similar final states. All the modes are studied using the data with SVD2. The data with SVD2 has been reprocessed using improved track finding and photon reconstruction algorithm.

3.2.2 Monte Carlo Samples

MC simulated events are generated to optimize the signal selection criteria, estimate the signal reconstruction and selection efficiencies, study background sources and to parameterize the signal and background shapes. Thus they play a vital role in optimizing and characterizing the physics analyses. MC production proceeds in two steps: event generation and modeling of detector response. Events are generated according to various physics processes using a decay table, which specifies the decay models, modes, BFs, etc for all possible particles involved in the decay chain. The event generation is done using the EvtGen event generator package [77], designed for simulating B meson decays based on particle properties (mass, width, lifetime, charge, etc) and event production rates compiled from many experiments in the form of world averages. The generated particles are then passed through GEANT [78–80] to simulate the detector response, after adding background from track hits and noise and data files are generated for analysis that match the real data formats. The schematic diagram of MC generation procedure is shown in Figure 3.1.

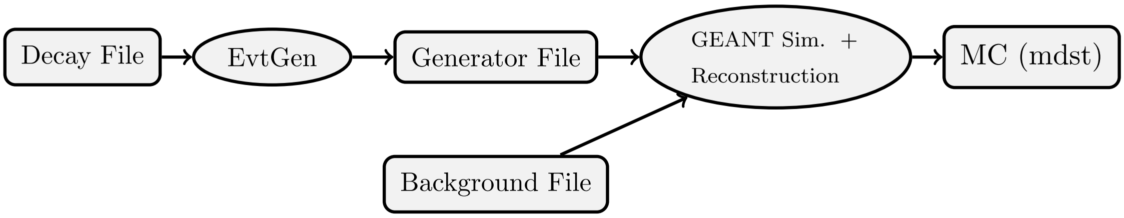

FIGURE 3.1: *Schematic diagram of MC generation procedure.*

3.2.2.1 Signal Monte Carlo

We have generated 100,000 MC events each for $B_s^{0*}\bar{B}_s^{0*}$, $B_s^{0*}\bar{B}_s^0$ and $B_s^0\bar{B}_s^0$ signal components both for $B_s^0 \to \phi\gamma$ and $B_s^0 \to \gamma\gamma$ analyses. We have also generated 500,000 signal MC events for $B^0 \to K^{0*}\gamma$. The decay models used to generate the signal MC events for $B_s^0 \to \phi\gamma$ and $B_s^0 \to \gamma\gamma$ are summarized as follows:

Models used for $B_s^0 \to \phi\gamma$

- N-Body Phase Space (PHSP) to generate $\Upsilon(5S) \to B_s^{0*}\bar{B}_s^{0*}$ and $\Upsilon(5S) \to B_s^{0*}\bar{B}_s^0$ events.
- Vector to Scalar and Scalar (VSS) to generate $\Upsilon(5S) \to B_s^0\bar{B}_s^0$ events.
- Vector to Scalar and Photon (VSP_PWAVE) to generate $B_s^{0*} \to B_s^0\gamma$ events.
- Photos Scalar to Vector and Photon helicity amplitude (PHOTOS SVP_HELAMP) with parameters ‘1.0 0.0 1.0 0.0’, to generate $B_s^0 \to \phi\gamma$ events.
- Vector to Scalar and Scalar (VSS) to generate $\phi \to K^+K^-$ events.

Models used for $B_s^0 \to \gamma\gamma$

- PHSP to generate $\Upsilon(5S) \to B_s^{0*}\bar{B}_s^{0*}$ and $\Upsilon(5S) \to B_s^{0*}\bar{B}_s^0$ events.
- VSS to generate $\Upsilon(5S) \to B_s^0\bar{B}_s^0$ events.
- VSP_PWAVE to generate $B_s^{0*} \to B_s^0\gamma$ events.
- PHSP to generate $B_s^0 \to \gamma\gamma$ events.

SVP_HELAMP model is basically used to describe $b \to s\gamma$ transitions. It is used to describe a 'scalar to vector and photon' process. The parameters used in the model '1.0 0.0 1.0 0.0' are the *magnitudes* and *phases* of the complex amplitudes of the particles which are specified in pairs. The amplitudes are ordered starting by the highest allowed helicity of the first particle. SVP_HELAMP with parameters '1.0 0.0 1.0 0.0' is also used to generate the $B^0 \to K^{0*}\gamma$ decay. The decay files for both $B_s^0 \to \phi\gamma$ and $B_s^0 \to \gamma\gamma$ are given in Appendix A.

3.2.2.2 Background Monte Carlo

The dominant background in these analyses arise from light quark continuum events ($u\bar{u}$, $d\bar{d}$, $s\bar{s}$ and $c\bar{c}$). Generic B_s ($B_s^{(*)}\bar{B}_s^{(*)}$) and non-B_s ($B^*\bar{B}^*\pi, \Upsilon(4S)\gamma$) decays of Υ(5S), QED events and 'two photon' processes resulting from the π^0 and η decays also contribute to the backgrounds. Dedicated MC samples for these processes are generated by MC production team in Belle. Six streams of the following background MC samples are used in these analyses:

- uds continuum ($e^+e^- \to u\bar{u}, d\bar{d}, s\bar{s}$)
- charm continuum ($e^+e^- \to c\bar{c}$)
- generic B_s ($e^+e^- \to \Upsilon(5S) \to B_s^{(*)}\bar{B}_s^{(*)}$)
- generic non-B_s ($e^+e^- \to \Upsilon(5S) \to B^*\bar{B}^*\pi, \Upsilon(4S)\gamma$)

Each stream corresponds to 121.4 fb^{-1} of data, i.e., the luminosity of the Υ(5S) real data sample.

3.3 Event Selection and Reconstruction

We select only those events which pass the L4 trigger and Hadron-B selection criteria. In this section, we describe the Hadron-B selection criteria in details. We further describe the reconstruction of signal candidates for both the decay modes and for the $B^0 \to K^{0*}\gamma$ channel.

3.3.1 Hadron-B Skim Criteria

e^+e^- collisions at $\Upsilon(5S)$ can lead to several $q\bar{q}$ processes, other than $b\bar{b}$. Processes such as Bhabha scattering and two-photon production (QED interactions) are also quite common. Hadron-B selection criteria is used to filter out the non-B events. MC studies have shown that these criteria retains 99% of $B\bar{B}$ events, 84% of continuum events and reject more than 95% of the non-hadronic components. The Hadron-B selection criteria selects B-meson events with following loose requirements:

- **Track Multiplicity**

  An event must have at least three good charged tracks, where a good charged track is required to originate from the IP and satisfy the following momentum and impact parameter conditions:
  $\mathrm{p_T} > 100$ MeV.
  dr $< 2.0\ cm$.
  dz $< 4.0\ cm$.
  where, dr and dz are the distance between the IP and the point of closest approach in the plane perpendicular to the beam axis (r-ϕ plane) and along the beam direction (z), respectively. The impact parameter requirements are used to reject the fake events that arise due to the beam particles striking the beam pipe or beam-residual gas interactions (beam-gas events).

- **Visible Energy of the Tracks and Photons**

  The visible energy ($\mathrm{E_{vis}}$) is the sum of the 'good track momenta' and 'good photon' energies in an event, where a 'good photon' refers to energy depositions in the ECL that donot match with charged tracks in the CDC. $\mathrm{E_{vis}} \geq 0.2\sqrt{s}$ condition is used to reject the 2-photon events.

- **Calorimeter Energy Sum**

  The calorimeter energy sum ($\mathrm{E_{sum}}$), i.e., the sum of energies of 'good clusters' in the ECL is required to satisfy $0.18 < \mathrm{E_{sum}}/\sqrt{s} < 0.8$. 'Good clusters' are clusters having energy deposit $>$ 100 MeV in the ECL. This requirement is used to suppress the Bhabha, 2 photon, beam-gas and τ events.

- **Momentum Balance**
  The total sum of longitudinal momenta of all 'good track' and 'good photon' should be balanced around zero. We require $|\sum \mathrm{p_z}| < 0.5\sqrt{s}$.

- **Event Primary Vertex**
  The beam-gas interaction events (which do not originate at the IP) can be removed by applying following criteria to the primary vertex of each event:
  $|\mathrm{dz}| < 3.5\ cm$, $\mathrm{dr} < 1.5\ cm$.

- **Calorimeter Cluster Multiplicity**
  Clusters produced due to Bhabha events have shallow angles. To remove these events, 2 photon events and beam-gas events, we require the number of clusters in the ECL to be greater than 1 within the fiducial volume of $-0.7 < \cos\theta < 0.9$.

- **Conditional Normalised Heavy Jet Mass**
  The most reliable condition for removing τ-pair events is the heavy jet mass (HJM). HJM is calculated by splitting an event into two hemispheres by a plane perpendicular to the thrust axis (thrust axis is described in section 3.4) of the event. The invariant mass ($\mathrm{M_{inv}} = \sqrt{(\mathrm{E}^{\mathrm{CM}}_{B^0_s})^2 - (\mathrm{p}^{\mathrm{CM}}_{B^0_s})^2}$) of all good tracks in each hemisphere is calculated. The tracks on the hemisphere with the larger invariant mass forms the heavy jet and that invariant mass is HJM. In order to cancel data-MC discrepancies, the ratio $\mathrm{HJM/E_{vis}}$ is used. The selection criteria are: $\mathrm{HJM/E_{vis}} > 0.25$ or $\mathrm{HJM} > 1.8$ GeV. For hadronic events, $\mathrm{HJM/E_{vis}}$ is about 0.4, whereas for τ pair events it is about 0.2.

- **Average Cluster Energy**
  If one of the electrons in a Bhabha event passes through a gap in the ECL, then the remaining detected energy will pass the selection criteria on $\mathrm{E_{sum}}$ described earlier. However, these events can still be removed by applying a condition on the average cluster energy ($\mathrm{E_{sum}/n_{ECL}}$). We require that $\mathrm{E_{sum}/n_{ECL}} < 1$ GeV.

3.3.2 Photon Selection

Photons are identified as energy depositions in the ECL that are not matched to a charged track. Candidate photons are required to have a minimum energy (E_γ) of 100 MeV. The other selection criteria are described below:

- To reject neutral hadrons like K_L^0 mesons and neutrons and merged photons from π^0, we use information about the shower shapes since electromagnetic and hadronic showers have different shapes in both the transverse and the longitudinal directions. Shower shapes in the transverse direction can be evaluated by using the variable $\mathrm{E}_9/\mathrm{E}_{25}$, which is the ratio of the energies summed in 3×3 array of crystals to that of 5×5 array of crystals in the transverse plane around the crystal with the largest energy deposit. ECL calorimeter cells representing the variable $\mathrm{E}_9/\mathrm{E}_{25}$ is shown in Figure 3.2. Showers caused by hadrons grow wider than the electromagnetic showers due to multiple showers caused by hadrons. For each ECL cluster, we require the ratio $\mathrm{E}_9/\mathrm{E}_{25}$ to be greater than 0.95 [81].

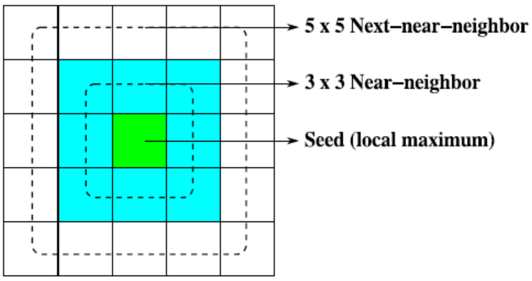

FIGURE 3.2: *ECL calorimeter cells representing the variable* $\mathrm{E}_9/\mathrm{E}_{25}$.

- For rare decay processes involving photons in the final state, high energy photons from π^0 and η can contribute as backgrounds. They are rejected on the basis of likelihood information ($\mathrm{P}_{\pi^0}(\gamma)$ and $\mathrm{P}_\eta(\gamma)$) obtained using energy and polar angle of the photons in the laboratory and diphoton invariant mass [82]. $\mathrm{P}_{\pi^0}(\gamma)$ and $\mathrm{P}_\eta(\gamma)$ denote the maximum probability that a candidate photon can be combined with another photon in the event to form a π^0 or η particle. We select photons only if $\mathrm{P}_{\pi^0}(\gamma) < 0.75$ and $\mathrm{P}_\eta(\gamma) < 0.65$.

- The decay $B_s^0 \to \gamma\gamma$ is characterized by two high-energy photons that are perfectly back to back in the CM system. Due to the long decay time of the CsI crystals, QED processes like Bhabha scattering or $e^+e^- \to \gamma\gamma$ events can leave two perfectly back-to-back clusters in the ECL (due to pile up) and can very well mimic the $B_s^0 \to \gamma\gamma$ events. This off-time QED background observed for the first time in $B^0 \to \gamma\gamma$ analysis [83], can be removed with 100% efficiency by requiring that the photons hit the ECL cluster within 9 to 11 micro-seconds of the collision [84]. As the timing information is not simulated, a selection based on MC truth information is used to remove such background from the simulated samples with an equal efficiency. Figures 3.3 and 3.4 show the $M_{\rm bc}$ distributions before and after applying the MC truth information and timing criteria to background MC and real data, respectively for the $B_s^0 \to \gamma\gamma$ analysis. We observe that these criteria remove the sharp peaks in the signal region of the $M_{\rm bc}$ plots which were arising due to off-time photons. This off-time QED background is not so dominant in $B_s^0 \to \phi\gamma$ case as there is a single photon in $B_s^0 \to \phi\gamma$ case and hence it is topologically distinct.

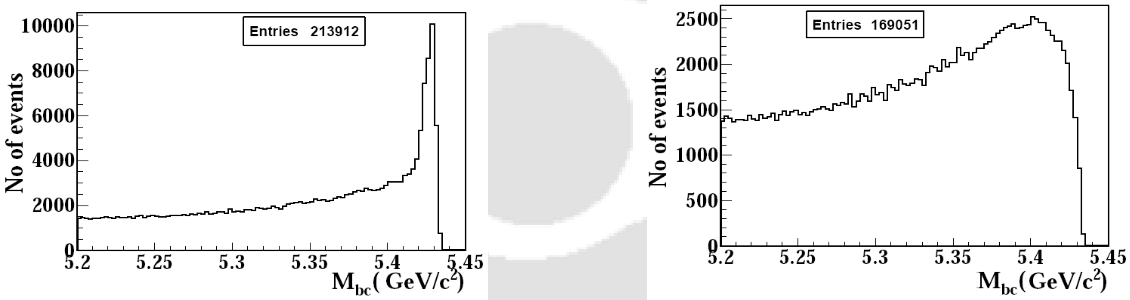

(a) (b)

FIGURE 3.3: *$M_{\rm bc}$ distributions for background MC (a) before and (b) after the photonID criteria for $B_s^0 \to \gamma\gamma$ analysis.*

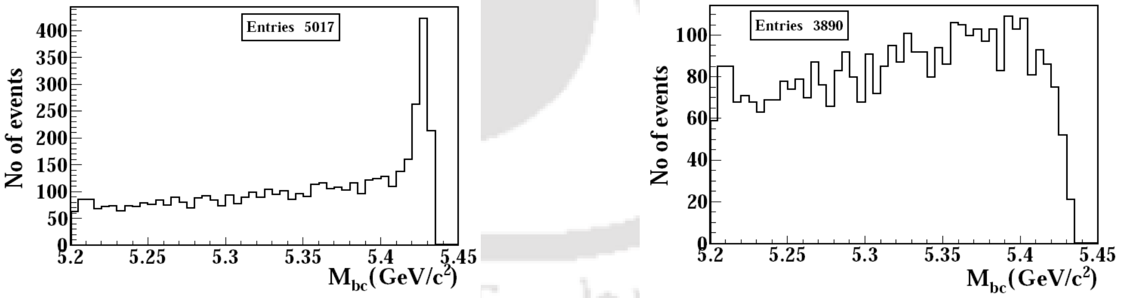

(a) (b)

FIGURE 3.4: *$M_{\rm bc}$ distributions for 1.86 fb^{-1} real data (a) before and (b) after the timing criteria for $B_s^0 \to \gamma\gamma$ analysis.*

- As there is a high level of beam background in the endcaps, we select photons only from the barrel region ($33° < \theta < 128°$) for $B_s^0 \to \gamma\gamma$. Moreover, it is very unlikely that one photon will be in the barrel and the other in the endcaps for a B_s^0 that decays at rest.

3.3.3 K/π Selection

Charged tracks with impact parameters |dr| < 0.5 *cm* and |dz| < 3 *cm* is considered to be a kaon candidate if it satisfies:

$$\mathcal{L}(K/\pi) \equiv \frac{\mathcal{L}_K}{\mathcal{L}_K + \mathcal{L}_\pi} > 0.6$$

Rest of the tracks are considered to be coming from pions. Here, $\mathcal{L}_K$ and $\mathcal{L}_\pi$ are the likelihood of the track to be coming from a kaon and pion, respectively. The likelihoods are calculated on the basis of dE/dx measurement by CDC, the Cherenkov light yield in ACC and the time of flight information from TOF by taking the product of the likelihood functions for three discriminants i.e.,

$$\mathcal{L}_i = \mathcal{L}_i^{\mathrm{CDC}}.\mathcal{L}_i^{\mathrm{ACC}}.\mathcal{L}_i^{\mathrm{TOF}}(i = K, \pi)$$

3.3.4 Reconstruction of ϕ and K^{0*} Candidate

The ϕ meson candidates are reconstructed by combining a pair of opposite charged kaons having an invariant mass $\mathrm{M}(K^+K^-)$ within ± 12 MeV/c^2 of the nominal ϕ mass. No events with multiple ϕ candidates are seen. K^{0*} candidates for the $B^0 \to K^{0*}\gamma$ control sample are reconstructed using oppositely charged kaon and pion candidates by requiring $|\mathrm{M}(K\pi) - \mathrm{M}(K^{0*})| < 75$ MeV/c^2. To remove the multiple K^{0*} candidates, K/π vertex fit is performed and events with the least χ^2 value is chosen as the best K^{0*} candidate.

3.3.5 Reconstruction of B_s^0 and B^0 Mesons

B_s^0 meson candidates are formed by combining a ϕ candidate with a photon candidate for $B_s^0 \to \phi\gamma$ decay or by combining 2 photon candidates for $B_s^0 \to \gamma\gamma$ decay. B_s^0 mesons are selected on the basis of the beam constrained mass (M_{bc}) and energy difference (ΔE) defined as:

$$M_{\mathrm{bc}} = \sqrt{(\mathrm{E}_{\mathrm{beam}}^{\mathrm{CM}})^2 - (\mathrm{p}_{B_s^0}^{\mathrm{CM}})^2}$$

$$\Delta\mathrm{E} = \mathrm{E}_{B_s^0}^{\mathrm{CM}} - \mathrm{E}_{\mathrm{beam}}^{\mathrm{CM}}$$

where, $\mathrm{E}_{\mathrm{beam}}^{\mathrm{CM}}$ is the beam energy, $\mathrm{E}_{B_s^0}$ and $\mathrm{p}_{B_s^0}$ are the energy and momentum of the B_s^0 candidate, all evaluated in the e^+e^- CM frame. Signal candidates are required to satisfy $M_{\mathrm{bc}} > 5.3$ GeV/c^2 and -0.4 < ΔE < 0.1 GeV for $B_s^0 \to \phi\gamma$ and $\mathrm{M}_{\mathrm{bc}} > 5.3$ GeV/c^2 and -0.7 < ΔE < 0.2 GeV for $B_s^0 \to \gamma\gamma$ mode. No events with multiple B_s^0 candidates are seen in signal MC events for $B_s^0 \to \gamma\gamma$ and negligible multiple events ($\sim$ 0.1%) are observed in $B_s^0 \to \phi\gamma$ case. Very few cases (< 1.0%) of multiple B_s^0 are observed for background MC and real data for both $B_s^0 \to \phi\gamma$ and $B_s^0 \to \gamma\gamma$ analyses. Those multiple B_s^0 candidates were removed by selecting the B_s^0 events with the highest energy photons.

K^{0*} candidates are combined with photon candidates to form B^0 candidates by applying $M_{\mathrm{bc}} > 5.0$ GeV/c^2 and -0.4 < ΔE < 0.2 GeV for $B^0 \to K^{0*}\gamma$ control sample. Multiple B^0 candidates coming from a particular event (< 1%) are removed by selecting the highest energy photons. The selection criteria are summarized in Table 3.1 for $B_s^0 \to \phi\gamma$ and $B_s^0 \to \gamma\gamma$ and in Table 3.2 for $B^0 \to K^{0*}\gamma$ mode.

Particle	**Channel**	**Criteria**
Photons	Both	$\mathrm{E}_\gamma > 100$ MeV $\mathrm{E}_9/\mathrm{E}_{25} > 0.95$ $\mathrm{P}_{\pi^0}(\gamma) < 0.75$ $\mathrm{P}_\eta(\gamma) < 0.65$
	$B_s^0 \to \gamma\gamma$	$9\ \mu sec < (\Delta\mathrm{T})_{\mathrm{ECL\ hit-collision}} < 11\ \mu sec$ $33^\circ < \theta < 128^\circ$
***K* Mesons**	$B_s^0 \to \phi\gamma$	$\lvert\mathrm{dr}\rvert < 0.5\ cm$ $\lvert\mathrm{dz}\rvert < 3\ cm$ $\mathcal{L}(K/\pi) > 0.6$ $\lvert\mathrm{M}(K^+K^-) - \mathrm{M}(\phi)\rvert < 12.0$ MeV/c^2
B_s^0 Mesons	Both	$M_{\mathrm{bc}} > 5.3$ GeV/c^2
	$B_s^0 \to \phi\gamma$	-0.4 GeV < ΔE < 0.1 GeV
	$B_s^0 \to \gamma\gamma$	-0.7 GeV < ΔE < 0.2 GeV

TABLE 3.1: *Selection criteria for $B_s^0 \to \phi\gamma$ and $B_s^0 \to \gamma\gamma$.*

Particle	**Criteria**
Photons	$\mathrm{E}_\gamma > 100$ MeV $\mathrm{E}_9/\mathrm{E}_{25} > 0.95$ $\mathrm{P}_{\pi^0}(\gamma) < 0.75$ $\mathrm{P}_\eta(\gamma) < 0.65$ $9\ \mu sec < (\Delta\mathrm{T})_{\mathrm{ECL\ hit-collision}} < 11\ \mu sec$
	$\lvert\mathrm{dr}\rvert < 0.5\ cm$ $\lvert\mathrm{dz}\rvert < 3\ cm$
$\boldsymbol{K/\pi}$	$\mathcal{L}(K/\pi) > 0.6$ for selecting kaons, rest considered pions $\lvert\mathrm{M}(K\pi) - \mathrm{M}(K^{0*})\rvert < 75$ MeV/c^2 Best K^{0*} chosen based on minimum χ^2 of $K\pi$ vertex fit
$\boldsymbol{B^0}$	$M_{\mathrm{bc}} > 5.2$ GeV/c^2 -0.4 GeV $< \Delta\mathrm{E} <$ 0.2 GeV

TABLE 3.2: *Selection criteria for* $B^0 \to K^{0*}\gamma$.

3.4 Continuum Background Suppression Using Multivariate Analysis

The dominating background for both the channels are $e^+e^- \to q\bar{q}$ continuum events where $q = u,\ d,\ s$ or c. The combined mass of a $B_s^{(*)}\bar{B}_s^{(*)}$ pair is less than that of the Υ(5S) resonance by only a few MeVs. So, the B_s^0 produced at Υ(5S) resonance have very low momentum and their decay products have a random direction, i.e., they have a spherical topology. Since for continuum events, a smaller proportion of e^+e^- energy goes towards particle production, these events have higher momentum and hence are topologically quite distinct from $\Upsilon(5\mathrm{S}) \to B_s^{(*)}\bar{B}_s^{(*)}$ events. Their decay products are distributed mostly along the beam direction, i.e., they have jet like topologies. So, we have put the event shape variables in an event classifier (described in the following subsections) to discriminate this type of background. Data is fed into the classifier after applying the selection criteria mentioned in Table 3.1. We have used the following variables for all three modes $B_s^0 \to \phi\gamma$, $B_s^0 \to \gamma\gamma$ and $B^0 \to K^{0*}\gamma$:

- **KSFW moments**: Kakuno Super Fox-Wolfram (KSFW) moments (denoted by R_i^{so}'s and R_i^{oo}'s) are modified Fox-Wolfram moments [85], which are used to quantify the topology of events from e^+e^- collisions.

R_i^{so}'s *are the moments associated with signal B and the other B in the event* and are defined as:

$$(R_i^{so})_j = \left[\frac{1}{(\mathrm{E_{beam}} - \Delta\mathrm{E})} \sum_a \sum_b Q_a Q_b |\mathrm{p}_b| P_i(\cos\theta_{ab})\right]_j$$

where, $Q_a Q_b = 1$ for $i = 0, 2, 4$.

R_i^{so}'s are subdivided into moments due to charged particles, neutral particles and a pseudo particle with a momentum that represents the total missing momentum of the event. The index 'j' runs over different sets of particles (*charged, neutral and missing energy*) denoted by c, n and m or 0, 1 and 2 where,

$$\mathrm{p}^*(\mathrm{missing}) = \sum_n^{N_{\mathrm{trk}}} \mathrm{p}_n^*$$

The index 'a' runs over the signal B daughters and 'b' runs over all the charged, neutral particles or the pseudo particles representing the total missing momentum produced in the event. This results in a total of 15 moments, but only 11 non-zero moments as those involving Q's are relevant only for charged particles.

R_i^{oo}'s *are the moments associated with both particles coming from the other B*, defined as:

$$(R_i^{oo}) = \frac{1}{(\mathrm{E_{beam}} - \Delta\mathrm{E})^2} \sum_a \sum_b Q_a Q_b |\mathrm{p}_a||\mathrm{p}_b| P_i(\cos\theta_{ab}) \quad \text{for } i = 0 - 4.$$

In this case, the indices 'a' and 'b' run over all particles that are not associated with signal B, p's are the three-momenta of each particle, $\mathrm{E_{beam}}$ is the beam energy and ΔE is the energy difference for the signal B, Q's are the charge of the corresponding particle, θ_{ab} is the angle between particles a and b, α's and β's are the coefficients of Fisher Discriminant, which are optimized using signal and background MC and $P_i(\cos\theta_{ab})$ are the Legendre's polynomials. Thus, we have another 5 moments totalling 16 modified moments. In addition to this 16 moments, we have,

$$\sum_n^{N_{\mathrm{trk}}} \mathrm{p_T} : \textit{ the sum of transverse momentum of all visible particles}$$

and '*the apparent mass that is missing from the event*' defined as:

$$\mathfrak{mm}^2 = (\mathrm{E}_\Upsilon - \sum_n^{N_{\mathrm{trk}}} \mathrm{E}_n)^2 - \sum_n^{N_{\mathrm{trk}}} |\mathrm{p}_n|^2$$

The final state particles that 'n' iterates over are generally the $\pi^\pm$, $K^\pm$, $p^\pm$, $e^\pm$, $\mu^\pm$ and γ.

- **$|\cos(\theta_{\mathrm{thrust}})|$**: It is the absolute value of the cosine of the angle between the thrust axis of the decay products of the B_s candidate and the rest of the event. The thrust axis is defined as the direction which maximises the sum of the longitudinal momenta of the particles in the decay.[1]

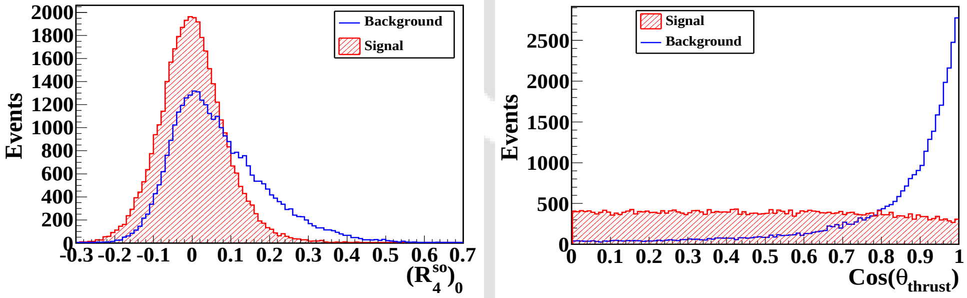

FIGURE 3.5: *Continuum suppression variables for $B_s^0 \to \phi\gamma$ analysis.*

We have thus used the KSFW moments and $\cos(\theta_{\mathrm{thrust}})$ in the pattern classifier. The distributions of one KSFW moment and $\cos(\theta_{\mathrm{thrust}})$ for signal and continuum background are shown in Figure 3.5 for $B_s^0 \to \phi\gamma$ analysis. Refer to Appendix B for the plots of event shape variables for all three modes.

3.4.1 Classification Problems and Multivariate Analysis

The basic aim of any classification problem is to distinguish between various types of events based on a number of discriminating variables. In HEP experiments, generally one wants to distinguish between signal and (continuum) background. In general, the task of a multivariate method [86] is to map an n-dimensional input variable space into a single

---

[1] B_s mesons produced at $\Upsilon(5S)$ resonance have very low momentum. So, the decay products of signal B_s and other B_s will have random directions and the distribution of $|\cos(\theta_{\mathrm{thrust}})|$ will be flat. Continuum events have higher momentum and their behaviour is jet like. So, the decay products will mostly lie along the beam axis and $|\cos(\theta_{\mathrm{thrust}})|$ will peak at 1.

scalar which contains all information including correlations between the input variables. The single variable can then be used as a discriminant instead of using all input variables separately. To use a multivariate classifier, it has to be trained first. For such training, one needs a large set of data for which the truth is known. Using a dataset of signal and continuum background MC events where the truth for every entry is known, the parameters of the classifier are determined in such a way that the classifier output is as close to the known truth as possible. After training unknown samples (i.e., validation samples) are fed to the network and it separates out signal and background events on the basis of the training. If the network is overtrained, the network may learn the statistical fluctuations and the distribution of the network output will be different for the training and validation samples. Care should be taken to avoid overtraining the network. The performance of a classifier is characterized by its efficiency $\mathcal{E}$ and purity $\mathcal{P}$, defined as:

$$\mathcal{E} = \frac{\mathrm{N_{Selected}}}{\mathrm{N_S}}$$

$$\mathcal{P} = \frac{\mathrm{N_{Selected}}}{\mathrm{N_{Total}}}$$

where, $\mathrm{N_{Selected}}$ is the number of selected signal events, $\mathrm{N_S}$ is the total number of signal events and $\mathrm{N_{Total}}$ is the total number of selected signal and background events. Any classifier should ideally have high efficiency as well as high purity. We have used NeuroBayes [87], a Belle standard neural network [88] package, which is based on Bayes theorem [89].

3.4.2 NeuroBayes Analysis

NeuroBayes is a neural network based event classification package, originally developed at the University of Karlsruhe. Now, it is being maintained and further developed by the company <phi-t>® (Physics Information Technologies). We have used a 3 layered feed forward neural network having a single output node with real valued output '$\mathbb{O}$' ranging from 0 to 1. If the network has 'n' input nodes and 'm' nodes in the hidden layer as shown in Figure 3.6, then the network output for an event is given by:

$$\mathbb{O} = \$(\sum_{j=1}^{m} w_j O_j) = \$(\sum_{j=1}^{m} w_j \$(\sum_{i=1}^{n} w_{ij} x_i - \theta_j))$$

where, x_i is the value of the i^{th} input node, O_j is the output of the j^{th} node of the hidden layer having n inputs x_i, often given in terms of the sigmoid function:

$$\mathbb{S}(x) \;=\; \left(\frac{2}{1-e^{-x}}\right) - 1$$

w_j is the weight of the connection of the hidden layer j to the output node, w_{ij} is the weight of the connection between the input node i and the hidden node j, and θ_j is the signal threshold for the hidden node j. There is no signal threshold applied in the output node. We have divided the entire MC sample into 2 parts for both the analysis. We have used $2/3^{rd}$ in training and $1/3^{rd}$ for validation.

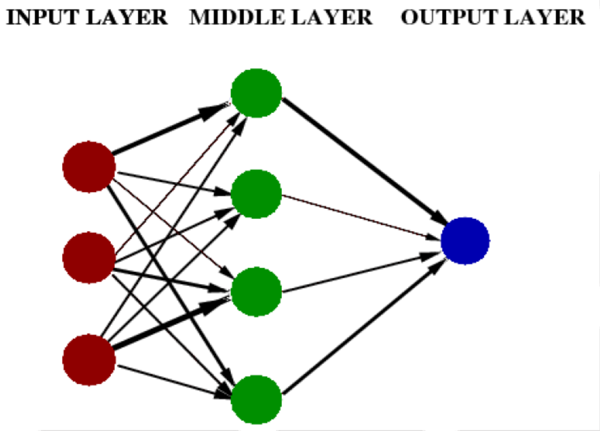

FIGURE 3.6: *3 layered feed forward network. Arrow thickness indicates weights.*

3.4.2.1 NeuroBayes Training

The neural network is trained by calling the NeuroBayes teacher which sets up the network topology and performs the actual training. During training, the weights are adjusted iteratively by comparing the network output with the truth t_i for each event. Training a neural network is basically a minimization of the cost function (some sort of error) by adjusting each weight. We have used entropy function as the cost function represented by:

$$\mathbb{E} \;=\; \sum_{i=1}^{N} \ln\left(\frac{1}{2(1+\mathbb{O}_i(\overrightarrow{w})t_i)}\right)$$

N and $\vec{w}$ being the number of training events and the vector of all weights. We have used BFGS algorithm [90] for finding the minimum of the cost function.

The input variables are preprocessed first so that the network can handle them easily. Various preprocessing options are available in NeuroBayes, which can be chosen individually for each input variable. The preprocessing enables to find the optimal starting point for the subsequent network training. Statistically insignificant network connections and even entire nodes are removed during the training to ensure that the network is not overtrained. At the end of the training, the trained network (called the expertise) is written to a file. The file contains all information needed to run an analysis e.g., the network parameters and all weights. After the training, the NeuroBayes expert is used for analysing unknown events. The training job prints out analysis information such as linear correlation matrix between the input variables and with the target, purity vs. efficiency plot, network architecture, errors vs. iteration for training sample. The errors should go down to indicate that the network is not overtrained. The training job also provides significance of each input variable and ranking of the individual variables. Figure 3.7(a) shows the correlation matrix between the input variables and the NeuroBayes target (referred as NN target in the Figure) for $B_s^0 \to \phi\gamma$ analysis, Figure 3.7(b) shows the error vs. iteration plot, Figure 3.8(a) shows the purity vs. efficiency plot and Figure 3.8(b) shows the purity vs. network output for $B_s^0 \to \phi\gamma$ analysis. For a well trained network, the purity as a

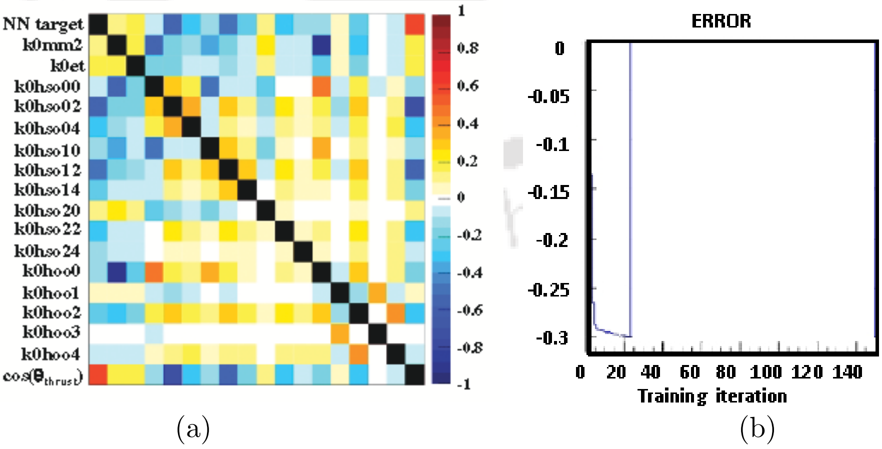

(a) (b)

FIGURE 3.7: *(a) Correlation matrix and (b) error vs. training iteration plot for* $B_s^0 \to \phi\gamma$ *analysis.*

function of NeuroBayes output should be on the diagonal. The purity vs. signal efficiency plot (Figure 3.8(a)) shows 2 curves. For the upper curve, the neural network output is bigger than the cut value and for the lower curve the network output is smaller than the cut value [91]. Refer to Appendix B for the plots of correlation matrices of the input variables and the NeuroBayes target for $B_s^0 \to \gamma\gamma$ and $B^0 \to K^{0*}\gamma$ analysis.

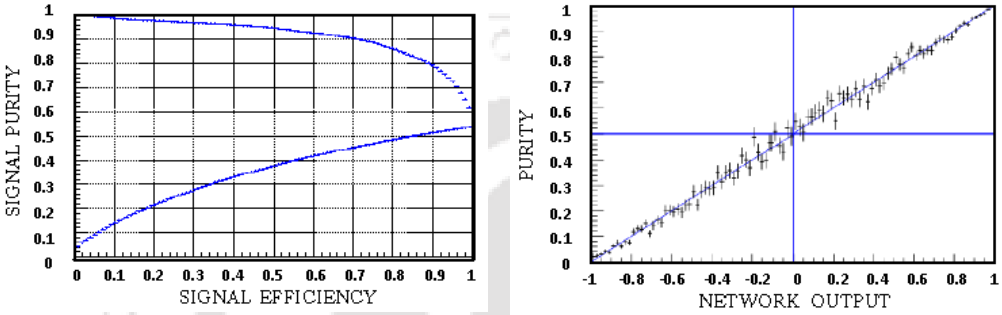

(a) (b)

FIGURE 3.8: *Performance plots of NeuroBayes training for $B_s^0 \to \phi\gamma$ analysis. (a) Purity vs. signal efficiency of the neural network (b) Purity vs. network output.*

3.4.2.2 Validation and Overtraining Check

We have used signal and continuum background MC sample in the NeuroBayes classifier for the training and validation. For training, we have used $2/3^{rd}$ of the available MC sample remaining after applying all the selection criteria. We have used rest of the MC data for validation purpose. To check whether overtraining has occurred or not, we have

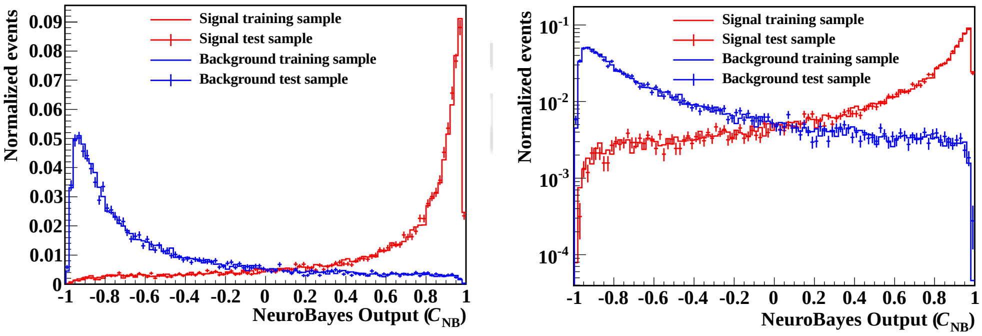

(a) (b)

FIGURE 3.9: *NB output for training and validation samples for $B_s^0 \to \phi\gamma$ analysis superimposed in (a) linear and (b) logarithmic vertical scale.*

superimposed the results for training and validation as shown in Figures 3.9 and 3.10 for $B_s^0 \to \phi\gamma$ and $B_s^0 \to \gamma\gamma$ analysis. Figures 3.9(b) and 3.10(b) shows the NeuroBayes outputs in the log scale. We find acceptable consistency between the training and validation (test) samples which signifies that there is no significant overtraining. Refer to Appendix B for training-validation superimposed plot for $B^0 \to K^{0*}\gamma$ analysis.

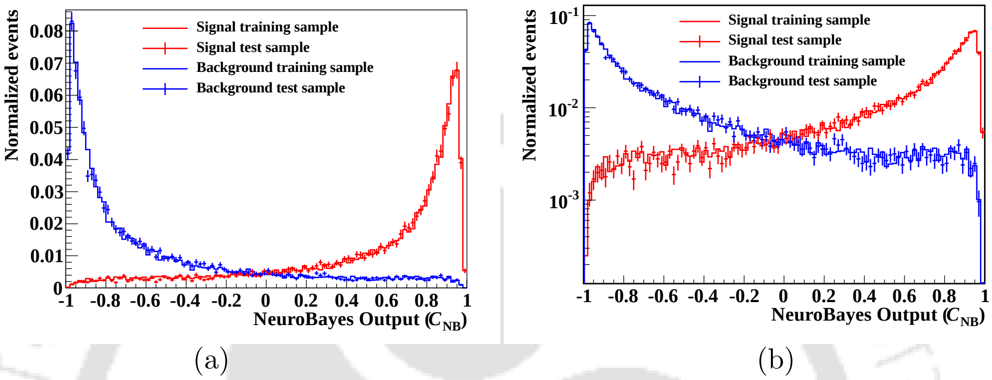

FIGURE 3.10: *NB output for training and validation samples for $B_s^0 \to \gamma\gamma$ analysis superimposed in (a) linear and (b) logarithmic vertical scale.*

3.4.2.3 NeuroBayes Output

The output obtained from the NeuroBayes classifier ($\mathcal{C}_{\rm NB}$) tends to peak at 1 for signal like events and at -1 for background like events, as shown in Figure 3.9. This variable is used as an additional dimension to perform an unbinned extended maximum likelihood fit to extract the signal yield for $B_s^0 \to \phi\gamma$ channel (maximum likelihood fit is described in details in Chapter 4). It is very difficult to model the $\mathcal{C}_{\rm NB}$ distribution with a simple analytic function. Thus to improve the modeling, modified NeuroBayes output is calculated as:

$$\mathcal{C}'_{\rm NB} = \log\left[\frac{(\mathcal{C}_{\rm NB} - \mathcal{C}_{\rm NB_{cut}})}{(\mathcal{C}_{\rm NB_{max}} - \mathcal{C}_{\rm NB})}\right]$$

after rejecting events with $\mathcal{C}_{\rm NB} <$ -0.6 where, $\mathcal{C}_{\rm NB_{cut}} =$ -0.6 and $\mathcal{C}_{\rm NB_{max}} \simeq 1$. For $B_s^0 \to \gamma\gamma$ mode, an optimized cut on $\mathcal{C}_{\rm NB}$ is applied, since considerable correlations are observed between $\mathcal{C}_{\rm NB}$ with $M_{\rm bc}$ and ΔE distributions. The optimized cut position is determined using the signal significance defined as:

$$\text{Signal significance} = \frac{\rm S}{\sqrt{\rm S + B}} \qquad (3.1)$$

after applying different $\mathcal{C}_{\mathrm{NB_{cut}}}$ values over the range -1 to +1. $\mathcal{C}_{\mathrm{NB_{cut}}}$ rejects events having network output $\mathcal{C}_{\mathrm{NB}} < \mathcal{C}_{\mathrm{NB_{cut}}}$. S $= w_s \times s$ and B $= w_s \times b$ are the expected signal and background events, w_s and w_b are the weight factors, determined using the signal and background expectations in data, s and b are the number of signal and background events remaining in the MC sample, after applying a particular $\mathcal{C}_{\mathrm{NB_{cut}}}$. The optimized cut is taken to be the $\mathcal{C}_{\mathrm{NB_{cut}}}$ value for which the signal significance is maximum. The optimized value of $\mathcal{C}_{\mathrm{NB_{cut}}}$ is found to be 0.77 as shown in Figure 3.11.

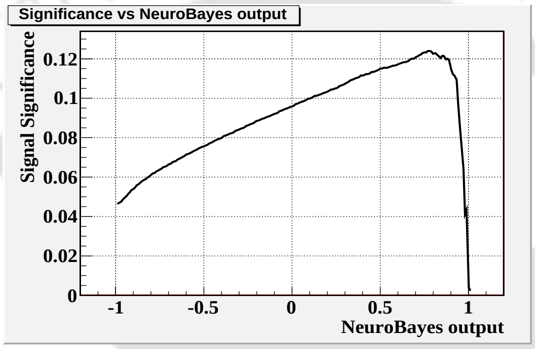

FIGURE 3.11: *Optimised $\mathcal{C}_{\mathrm{NB}}$ cut for $B_s^0 \to \gamma\gamma$ analysis.*

3.5 Signal Selection Efficiency

The signal selection efficiency (ϵ) and its statistical error[2] ($\Delta\epsilon$) are computed as:

$$\epsilon = \left(\frac{\mathrm{N_R}}{\mathrm{N}}\right) \quad \text{and} \quad \Delta\epsilon = \sqrt{\frac{\epsilon \times (1-\epsilon)}{\mathrm{N}}}$$

where, N is the total number of signal MC events generated for each mode. For both the modes, we have generated 100,000 signal MC events each for $B_s^{0*}\bar{B}_s^{0*}$, $B_s^{0*}\bar{B}_s^0$ and $B_s^0\bar{B}_s^0$ signals. $\mathrm{N_R}$ is the number of signal MC events remaining after applying all signal selection criteria, which is 36,125, 36,131 and 36,051 events respectively for the $(B_s^0 \to \phi\gamma)_{B_s^{0*}\bar{B}_s^{0*}}$, $(B_s^0 \to \phi\gamma)_{B_s^{0*}\bar{B}_s^0}$ and $(B_s^0 \to \phi\gamma)_{B_s^0\bar{B}_s^0}$ signals. Thus, the signal efficiencies are computed to be $(36.1 \pm 0.2)\%$ for all three $(B_s^0 \to \phi\gamma)$ signals. For the $B_s^0 \to \gamma\gamma$ mode, we have 14,136, 13,964 and 13,943 events respectively after all the selection cuts for B_s^0 originating from $B_s^{0*}\bar{B}_s^{0*}$, $B_s^{0*}\bar{B}_s^0$ and $B_s^0\bar{B}_s^0$. Thus, the signal efficiencies are computed to be $(14.1 \pm 0.1)\%$,

---

[2] The error on the signal selection efficiency is given by Binomial statistics.

$(14.0 \pm 0.1)\%$ and $(13.9 \pm 0.1)\%$ for $(B_s^0 \to \gamma\gamma)_{B_s^{0*}\bar{B}_s^{0*}}$, $(B_s^0 \to \gamma\gamma)_{B_s^{0*}\bar{B}_s^0}$ and $(B_s^0 \to \gamma\gamma)_{B_s^0\bar{B}_s^0}$ signals.

3.6 Study of Generic B_s and non-B_s Backgrounds

Decay modes similar to $B_s^0 \to \phi\gamma$ and $B_s^0 \to \gamma\gamma$ analyses may arise from generic B_s (i.e., $B_s^{(*)}\bar{B}_s^{(*)}$) and non-B_s (i.e., $B^*\bar{B}^*\pi$, $\Upsilon(4S)\gamma$) decays and can get misidentified as a signal candidate. For e.g., $B_s^0 \to \phi\eta$, $B_s^0 \to \phi\pi^0$ and $B^0 \to K^{0*}\gamma$ decays may contribute as backgrounds for the $B_s^0 \to \phi\gamma$ mode. To study whether these backgrounds are significant, we study a dedicated MC sample of $e^+e^- \to B_s^{0*}\bar{B}_s^{0*}$ and $e^+e^- \to B^*\bar{B}^*\pi$, $\Upsilon(4S)\gamma$ events. After applying all the selection criteria, we see that the background contribution from these decays are less than an event in the $B_s^{0*}\bar{B}_s^{0*}$, $B_s^{0*}\bar{B}_s^0$ and $B_s^0\bar{B}_s^0$ signal regions for $B_s^0 \to \phi\gamma$ analysis, where the $B_s^0 \to \phi\gamma$ signal regions are defined as:

$(B_s^0 \to \phi\gamma)_{B_s^{0*}\bar{B}_s^{0*}}$ Signal Region

- $M_{\rm bc} > 5.4$ GeV/c^2.
- -0.2 < ΔE < 0.02 GeV.
- $|\cos(\theta_{\rm hel})| < 0.8$.[3]
- $\mathcal{C}'_{\rm NB} > 0.0$

$(B_s^0 \to \phi\gamma)_{B_s^{0*}\bar{B}_s^0}$ Signal Region

- $5.38 < M_{\rm bc} < 5.4$ GeV/c^2.
- -0.2 < ΔE < 0.02 GeV.
- $|\cos(\theta_{\rm hel})| < 0.8$
- $\mathcal{C}'_{\rm NB} > 0.0$

---

[3] For the decay $B_s^0 \to \phi\gamma$, $\phi \to K^+K^-$, the helicity angle is defined as the angle between B_s^0 and any of the ϕ daughters (K^+ or K^-) in the ϕ rest frame. For signal events, $\cos(\theta_{\rm hel})$ follows a $1 - \cos^2(\theta_{\rm hel}) \equiv \sin^2(\theta_{\rm hel})$ distribution, due to the longitudinal helicity of the ϕ meson, while for continuum events it has a flat distribution.

$(B_s^0 \to \phi\gamma)_{B_s^0\bar{B}_s^0}$ Signal Region

- $5.35 < M_{\rm bc} < 5.38$ GeV/c^2.
- -0.2 < ΔE < 0.02 GeV.
- $|\cos(\theta_{\rm hel})| < 0.8$
- $\mathcal{C}'_{\rm NB} > 0.0$

The background contribution from these decays in the different signal regions are shown in Figures 3.12, 3.13 and 3.14 for $B_s^0 \to \phi\gamma$ analysis. These plots correspond to 6 streams, each stream having the same luminosity as data. No contribution from these decays are observed (from 6 streams) in the signal regions for $B_s^0 \to \gamma\gamma$ analysis. The $B_s^0 \to \gamma\gamma$ signal regions are defined as:

$(B_s^0 \to \gamma\gamma)_{B_s^{0*}\bar{B}_s^{0*}}$ Signal Region

- $M_{\rm bc} > 5.4$ GeV/c^2.
- -0.3 < ΔE < 0.05 GeV.

$(B_s^0 \to \gamma\gamma)_{B_s^{0*}\bar{B}_s^0}$ Signal Region

- $5.38 < M_{\rm bc} < 5.4$ GeV/c^2.
- -0.3 < ΔE < 0.05 GeV.

$(B_s^0 \to \gamma\gamma)_{B_s^0\bar{B}_s^0}$ Signal Region

- $5.35 < M_{\rm bc} < 5.38$ GeV/c^2.
- -0.3 < ΔE < 0.05 GeV.

The plots of all the fit variables after applying the fit region cuts and the different signal region cuts on other dimensions are presented in Appendix C for both the analyses.

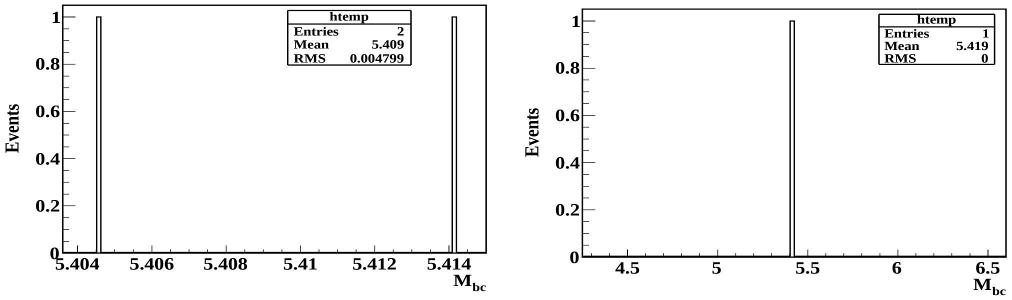

FIGURE 3.12: *Distribution of generic B_s and non-B_s backgrounds for $B_s^0 \to \phi\gamma$ after all $(B_s^0 \to \phi\gamma)_{B_s^{0*}\bar{B}_s^{0*}}$ signal region cuts (6 streams).*

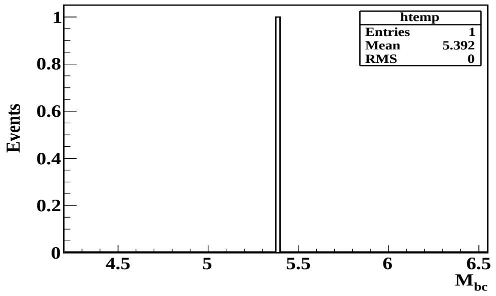

FIGURE 3.13: *Distribution of generic B_s background for $B_s^0 \to \phi\gamma$ after all $(B_s^0 \to \phi\gamma)_{B_s^{0*}\bar{B}_s^{0}}$ signal region cuts (6 streams). No event is seen (from 6 steams) for non-B_s background.*

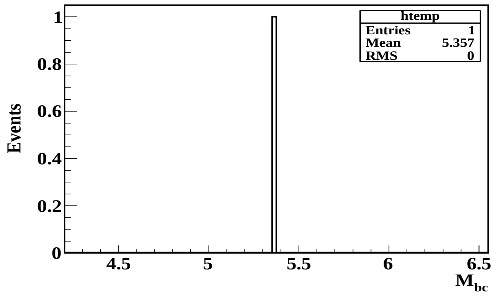

FIGURE 3.14: *Distribution of generic B_s background for $B_s^0 \to \phi\gamma$ after all $(B_s^0 \to \phi\gamma)_{B_s^{0}\bar{B}_s^{0}}$ signal region cuts (6 streams). No event is seen (from 6 steams) for non-B_s background.*

3.7 Chapter Summary

In this chapter, we have discussed the datasets used in these analyses, MC generation procedure and have introduced the concept of blind analysis briefly. We have also described the loose selection criteria applied to generate the skimmed data sample used in these analyses. The event selection and reconstruction of signal events and continuum suppression technique are described in details. Contribution from peaking backgrounds are also studied in this chapter.

Chapter 4

Maximum Likelihood Fit Analysis

In this chapter, we present a brief overview of the maximum likelihood (ML) fit procedure used to extract the signal yield in the real data. We have performed a 4 dimensional (2 dimensional) unbinned extended ML fit involving $M_{\rm bc}$, ΔE, cosine of the helicity angle ($\cos(\theta_{\rm hel})$) and $\mathcal{C}'_{\rm NB}$ ($M_{\rm bc}$ and ΔE) to extract the signal yield for $B_s^0 \to \phi\gamma$ ($B_s^0 \to \gamma\gamma$) analysis. The parametrization of signal and background probability distribution functions (PDFs), estimation of the resolution (sigma) correction factors for $M_{\rm bc}$ and ΔE from $B^0 \to K^{0*}\gamma$ control sample and the fit results of $B_s^0 \to \phi\gamma$ ($B_s^0 \to \gamma\gamma$) analysis are also presented.

4.1 Maximum Likelihood Fit

The ML fit [92–96] is a method of estimating the values of various parameters of a distribution. In statistics, the term ‘estimation’ means a precise and accurate procedure, leading to a result (for e.g., the value of parameter of a distribution) that may be imprecise, but where the extent of imprecision is known [92]. For a data sample $\{x_1, x_2, ..., x_n\}$ of n independent and identically distributed observations, the likelihood $L(\xi|x_1, x_2, \ldots, x_n)$ can be written as:

$$L(\xi|x_1, x_2, \ldots, x_n) = f(x_1, x_2, \ldots, x_n|\xi) = \prod_{i=1}^{n} f(x_i|\xi)$$

where, ξ denotes the vector of parameters of the unknown distribution. The likelihood function represents the probability of observing the sequence of values $x_1, x_2, \ldots, x_n$. The ML estimator $\hat{\xi}_j$ for a parameter ξ_j, is that value of ξ_j for which the likelihood (L) is maximum which can be found by solving the equation:

$$\frac{\mathrm{d}L}{\mathrm{d}\xi_j} = 0. \tag{4.1}$$

In practice, it is easier to maximize the logarithm of the likelihood function i.e., to solve the equation:

$$\frac{\mathrm{d}(\ln L)}{\mathrm{d}\xi_j} = 0 \quad \text{where,} \quad \ln L(\xi_j|x_i, x_2, \ldots, x_n) = \sum_{i=1}^{n} \ln f(x_i|\xi_j). \tag{4.2}$$

The solution $\hat{\xi}_j$ is known as the ML estimator for the parameter ξ_j. The value of the estimator $\hat{\xi}_j$ will be different for different samples and will be described by a probability distribution. The error $(\sigma(\hat{\xi}_j))$ on the estimator distribution is given by:

$$\sigma^2(\hat{\xi}_j) = \int (\xi_j - \hat{\xi}_j)^2 L(\xi_j|x) \mathrm{d}x_1 \mathrm{d}x_2 \ldots \mathrm{d}x_n. \tag{4.3}$$

When more than 1 parameter is involved, 'd' will be replaced by '∂' in equations 4.1 and 4.2 and the error on the parameters can be expressed as:

$$\sigma^2(\hat{\xi}_{jk}) = \int (\xi_j - \hat{\xi}_j)(\xi_k - \hat{\xi}_k) L(\xi|x) \mathrm{d}x_1 \mathrm{d}x_2 \ldots \mathrm{d}x_n. \tag{4.4}$$

Here, j and k run over the set of parameters. In the limit of large numbers this can be approximated to:

$$\sigma^2(\hat{\xi}_{jk}) \simeq -\left(\frac{\partial^2 \ln L}{\partial \xi_j \partial \xi_k}\right)^{-1} \equiv (V_{jk})^{-1}. \tag{4.5}$$

In general, the ML estimators are *consistent, unbiased and efficient* for large samples. An estimator is called *consistent* if the difference between the estimate and true value vanishes for large samples i.e., if:

$$\lim_{N\to\infty} \hat{\xi}_j = \xi_j \quad \text{or} \quad \lim_{N\to\infty} (\hat{\xi}_j - \xi_j) = 0.$$

An estimator is said to be *unbiased*, if its expectation value is equal to the true value i.e.,

$$\left\langle \hat{\xi}_j \right\rangle = \xi_j .$$

An estimator is *efficient* if its variance $\sigma^2(\hat{\xi}_j)$ is small. In this section we have described the unbinned ML fit. In 'unbinned ML' fit the bin size of the fit approaches 0 i.e., individual events (observations) are fitted.

4.1.1 Extended Maximum Likelihood Fit

In the standard method of ML, the probability or probability density of x, $f(x|\xi)$ is normalized to 1 i.e.,

$$\int f(x|\xi)\mathrm{d}x = 1.$$

In extended ML case, this requirement is relaxed. Instead of the function $f(x|\xi)$, a function $g(x|\xi)$ is used for which the normalization is not fixed. Increasing or decreasing $g(x|\xi)$ in some region of x increases or decreases the probability of events occurring in that region and thus increases or decreases the total expected number of events, N, which is given by the total integral of $g(x|\xi)$ i.e.,

$$\int g(x|\xi)\mathrm{d}x = N.$$

This is appropriate in experiments where the number of events is indeed unknown a priori, and in such cases extended ML is an improvement over ML.

The extended ML function $\mathbb{L}$ is formed by multiplying the classical likelihood L with a Poisson distribution [92]. Thus,

$$\begin{aligned}\mathbb{L}(N,\xi) &= \frac{e^{-N}N^n}{n!}\prod_{i=1}^{n} f(x_i|\xi)\\ &= \frac{e^{-N}}{n!}\prod_{i=1}^{n} Nf(x_i|\xi).\end{aligned}$$

When the data sample consists of events of many categories, the extended ML fit can be used to extract the number of events in each category. The likelihood function can then be written as:

$$\begin{aligned}\mathbb{L} &= \frac{e^{-\sum\limits_{l=1}^{m} N_l}}{n!}\prod_{i=1}^{n}\left(\sum_{l=1}^{m} N_l f(x_i|\xi)_l\right)\\ &= \frac{e^{-\sum\limits_{l=1}^{m} N_l}}{n!}\prod_{i=1}^{n}\left(\sum_{l=1}^{m} g(x_i|\xi)_l\right).\end{aligned}$$

where, $N = \sum\limits_{l=1}^{m} N_l$, with l running over all possible event categories $(1,2,\ldots,m)$, N_l's are the expected number of events of each category and $f(x_i|\xi)_l$'s are the PDFs for each category evaluated at the l^{th} event. In HEP, the data mostly consists of signal and background events and an extended ML function is used to determine the number of signal and background events through a fit.

Dropping the constant term $n!$, the log likelihood of an extended ML function can be written as:

$$\ln\mathbb{L} = \sum_{i=1}^{n}\ln\left(\sum_{l=1}^{m} g(x_i|\xi)_l\right) - \sum_{l=1}^{m} N_l.$$

For large statistics cases (i.e., when n is large) the likelihood function is Gaussian and the log-likelihood function is a parabola [92, 97]. The parameter uncertainties are symmetric in such cases.

In the analyses presented in this thesis, the estimation of the parameters of the distribution is done in the ROOT framework using RooFit package [95, 96] which minimizes the equivalent function, the negative log likelihood (NLL). The NLL has the form:

$$\text{NLL (or} -\ln\mathbb{L}) = \sum_{l=1}^{m} N_l - \sum_{i=1}^{n}\ln\left(\sum_{l=1}^{m} g(x_i|\xi)_l\right).$$

There are several algorithms to find the minimum of a function [98–100]. In HEP community, minimization is mostly done through the MIGRAD algorithm [98] of the MINUIT package. The analyses presented in the thesis are done with limited statistics. For such cases the log-likelihood function is not a perfect parabola and hence, the parameter uncertainties are asymmetric. The MIGRAD algorithm fails to provide accurate values of such uncertainties. To estimate these asymmetric uncertainties, the MINOS algorithm [97, 98] (of the MINUIT package) is used. The MINOS algorithm is usually called after MIGRAD minimization.

Extended ML estimators have a bias for finite n, which vanishes in the large n limit. Unbinned extended ML fit is mostly done when the width of the peak is unknown and when the number of data points 'n' is very small.

4.2 Fit Procedure for $B_s^0 \to \phi\gamma$

We have performed a 4D unbinned extended ML fit with $M_{\rm bc}$, ΔE, cos($\theta_{\rm hel}$) and $\mathcal{C}'_{\rm NB}$ to extract the $B_s^0 \to \phi\gamma$ signals in the three ($B_s^{0*}\bar{B}_s^{0*}$, $B_s^{0*}\bar{B}_s^0$ and $B_s^0\bar{B}_s^0$) signal regions. Four components are used in the fitting: $B_s^0 \to \phi\gamma$ signals coming from $B_s^{0*}\bar{B}_s^{0*}$, $B_s^{0*}\bar{B}_s^0$, $B_s^0\bar{B}_s^0$ decays (i.e., $(B_s^0 \to \phi\gamma)_{B_s^{0*}\bar{B}_s^{0*}}$, $(B_s^0 \to \phi\gamma)_{B_s^{0*}\bar{B}_s^0}$ and $(B_s^0 \to \phi\gamma)_{B_s^0\bar{B}_s^0}$ signals) and $q\bar{q}$ background. The variables used in the fit should not have high correlation among themselves. Before performing the fit, we have checked and found no such strong correlations among them as shown in Figures 4.1(a), (b), (c) and (d) for $(B_s^0 \to \phi\gamma)_{B_s^{0*}\bar{B}_s^{0*}}$, $(B_s^0 \to \phi\gamma)_{B_s^{0*}\bar{B}_s^0}$, $(B_s^0 \to \phi\gamma)_{B_s^0\bar{B}_s^0}$ signals and $q\bar{q}$ background, respectively. The values of correlation between different variables are summarized in Table 4.1. The background contribution from generic B_s and non-B_s decays are less than an event in all the signal regions for $B_s^0 \to \phi\gamma$ after we apply all the selection cuts (details in Chapter 3 and Appendix C). Since, these events are very few and they don't have a peaking structure, so they behave like continuum backgrounds. So, they are included in $q\bar{q}$ PDF. For $B_s^0 \to \phi\gamma$ analysis, the fit regions chosen for different variables are listed below:

- $M_{\rm bc}$ $\longrightarrow$ (5.3 - 5.434) GeV/c^2
- ΔE $\longrightarrow$ (-0.4 - 0.1) GeV
- cos($\theta_{\rm hel}$) $\longrightarrow$ (-1.0 - 1.0)
- $\mathcal{C}'_{\rm NB}$ $\longrightarrow$ (-10.0 - 10.0)

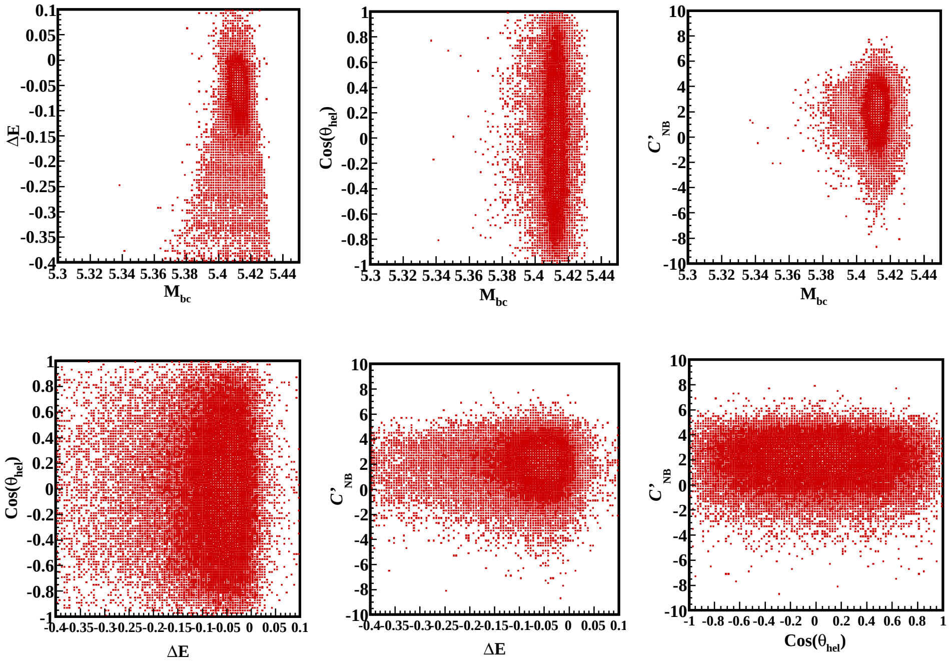

(a) *Correlation between the fit variables for* $B_s^0 \to \phi\gamma$ *signal produced from* $B_s^{0*}\bar{B}_s^{0*}$ *decays.*

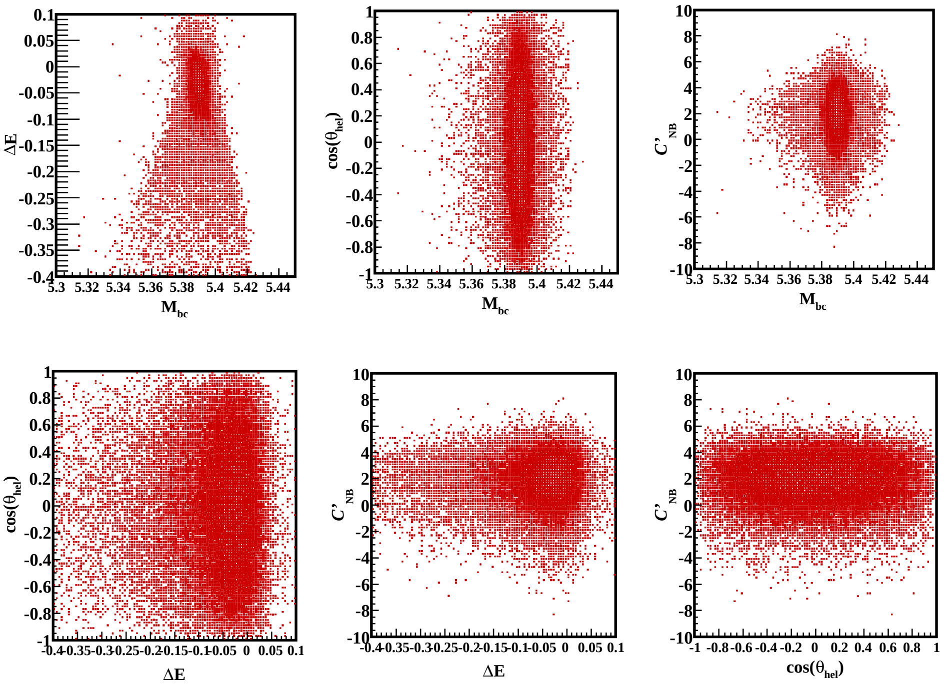

(b) *Correlation between the fit variables for* $B_s^0 \to \phi\gamma$ *signal produced from* $B_s^{0*}\bar{B}_s^0$ *decays.*

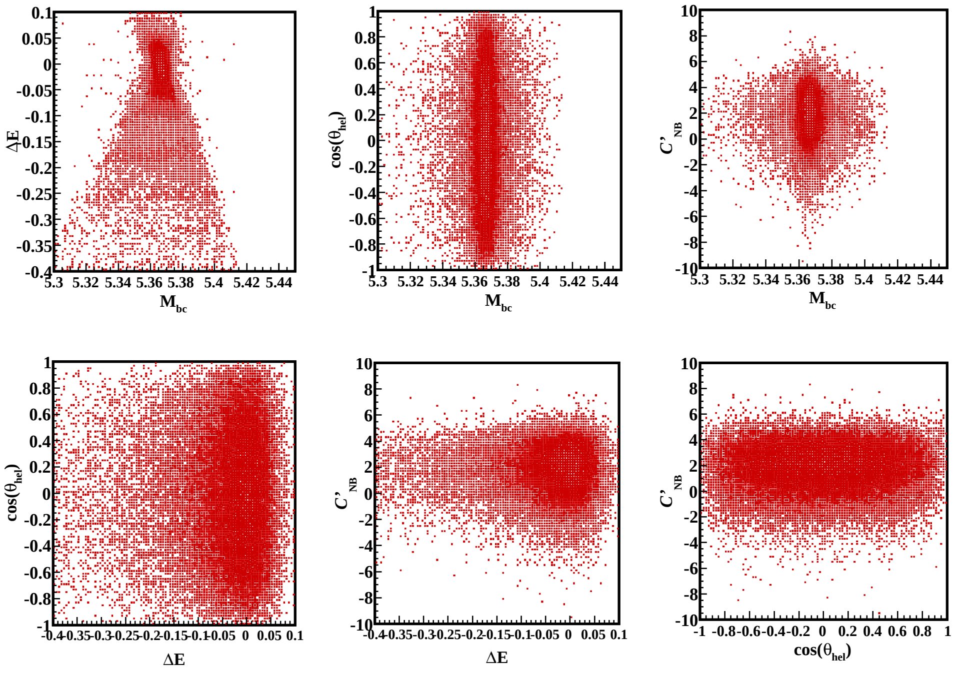

(c) Correlation between the fit variables for $B_s^0 \to \phi\gamma$ signal produced from $B_s^0 \bar{B}_s^0$ decays.

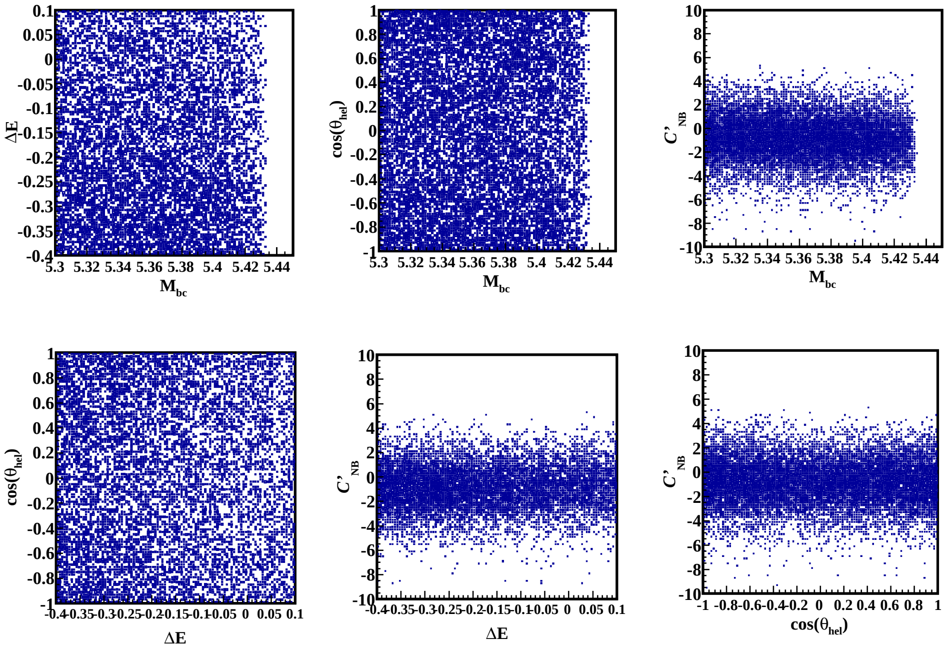

(d) Correlation between the fit variables for continuum ($q\bar{q}$) background.

FIGURE 4.1: *Correlation between different variables for $B_s^0 \to \phi\gamma$ analysis.*

Variables	**Correlation Factor (%)**			
	(Signal)$_{B_s^{0*}\bar{B}_s^{0*}}$	**(Signal)**$_{B_s^{0*}\bar{B}_s^{0}}$	**(Signal)**$_{B_s^{0}\bar{B}_s^{0}}$	**Background**
$\boldsymbol{M_{\rm bc}:\Delta\mathbf{E}}$	9.37	-1.62	-5.70	-1.68
$\boldsymbol{M_{\rm bc}:\cos(\theta_{\rm hel})}$	-1.33	0.93	1.27	0.56
$\boldsymbol{M_{\rm bc}:\mathcal{C}'_{\rm NB}}$	0.67	2.05	0.44	-6.93
$\boldsymbol{\Delta\mathbf{E}:\cos(\theta_{\rm hel})}$	0.07	0.01	-0.14	-0.80
$\boldsymbol{\Delta\mathbf{E}:\mathcal{C}'_{\rm NB}}$	0.55	0.63	1.22	2.98
$\boldsymbol{\cos(\theta_{\rm hel}):\mathcal{C}'_{\rm NB}}$	-0.58	0.09	1.25	-2.22

TABLE 4.1: *Values of correlation between different variables used in* $B_s^0 \to \phi\gamma$ *fit.*

4.2.1 Signal and Background PDFs

Signal MC samples are used to parameterize the signal PDFs. The $M_{\rm bc}$ distributions are parameterized with a Crystal Ball (CBall) function (CBall function is described in Appendix D) for $(B_s^0 \to \phi\gamma)_{B_s^{0*}\bar{B}_s^{0*}}$ signal and with double-Gaussian functions (2 Gaussians having common mean) for $(B_s^0 \to \phi\gamma)_{B_s^{0*}\bar{B}_s^{0}}$ and $(B_s^0 \to \phi\gamma)_{B_s^{0}\bar{B}_s^{0}}$ signals. The ΔE, $\cos(\theta_{\rm hel})$ and $\mathcal{C}'_{\rm NB}$ distributions of all three signals are modeled with CBall functions, $\sin^2(\theta_{\rm hel})$ functions and with a combination of two Gaussian functions, respectively. The functions

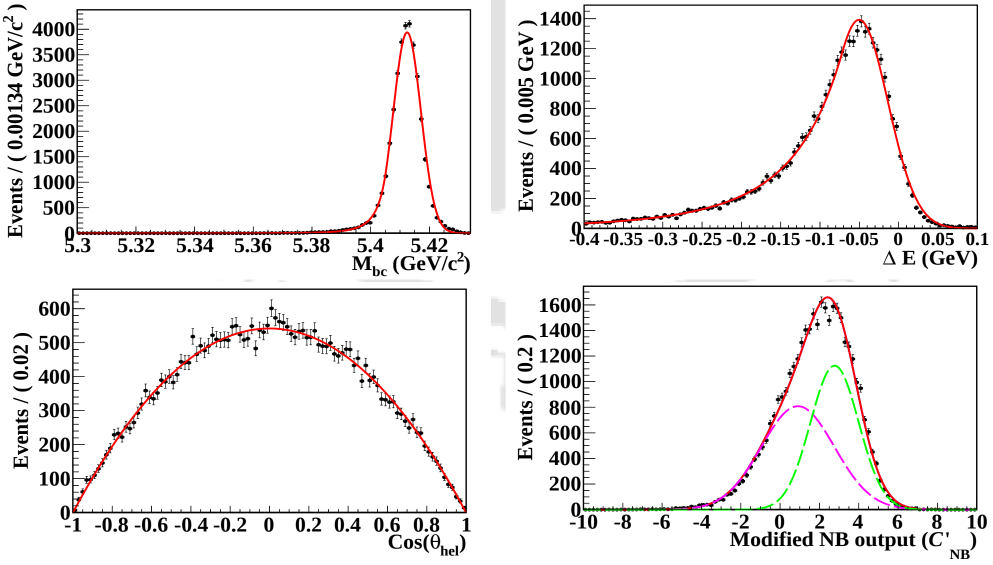

FIGURE 4.2: *Parameterization of* $M_{\rm bc}$*,* ΔE*,* $\cos(\theta_{\rm hel})$ *and* $\mathcal{C}'_{\rm NB}$ *distributions of* $(B_s^0 \to \phi\gamma)_{B_s^{0*}\bar{B}_s^{0*}}$ *signal. The points with error bars represent the signal MC data and the solid red curve represents the signal MC fit function. The dashed magenta and green curves in the* $\mathcal{C}'_{\rm NB}$ *plot represent the contributions from different Gaussian components.*

and fit parameters for different signals are summarized in Tables 4.2, 4.3 and 4.4, respectively and the plots are shown in Figures 4.2, 4.3 and 4.4.

Variable	**Function**	**Parameter**	**Value**	**Comment**
$M_{\rm bc}$	CBall function	Mean (μ)	5412.43 ± 0.03 MeV/c^2	Floated
		Sigma (σ)	4.71 ± 0.02 MeV/c^2	Floated
		n	4.59 ± 0.27	Floated
		alpha (α)	1.52 ± 0.03	Floated
ΔE	CBall function	Mean (μ)	-50.32 ± 0.59 MeV	Floated
		Sigma (σ)	36.70 ± 0.38 MeV	Floated
		n	5.15 ± 0.47	Floated
		alpha (α)	0.57 ± 0.02	Floated
$\cos(\theta_{\rm hel})$	$\sin^2(\theta_{\rm hel})$	No parameter		
$\mathcal{C}'_{\rm NB}$	2 Gaussian functions	Mean1 (μ_1)	0.90 ± 0.06	Floated
		Sigma1 (σ_1)	1.86 ± 0.02	Floated
		Mean2 (μ_2)	2.77 ± 0.04	Floated
		Sigma2 (σ_2)	1.23 ± 0.02	Floated
		Fraction (f)	0.52 ± 0.02	Floated

TABLE 4.2: $(B_s^0 \to \phi\gamma)_{B_s^{0*}\bar{B}_s^{0*}}$ *signal MC parameterizations.*

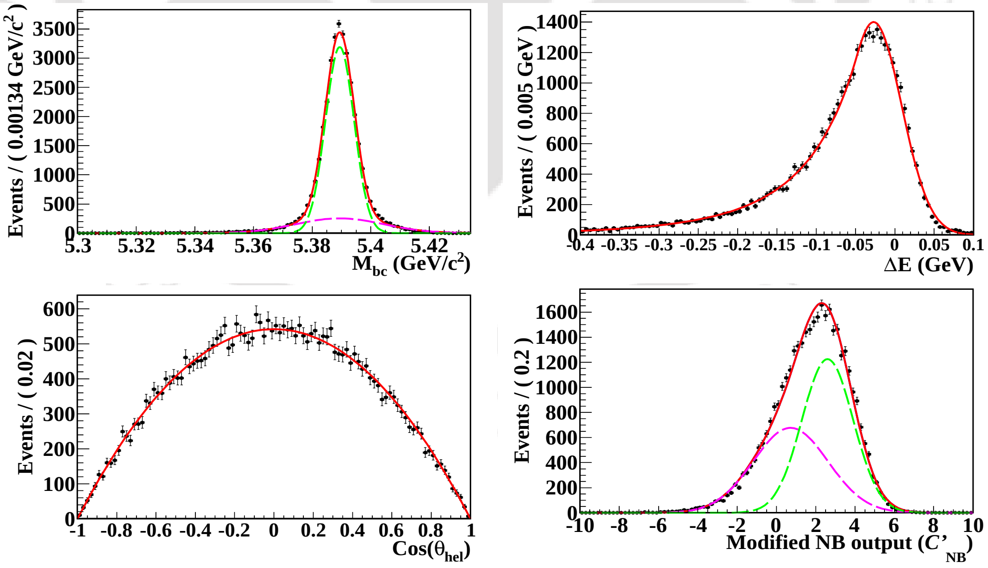

FIGURE 4.3: *Parameterization of* $M_{\rm bc}$*,* ΔE*,* $\cos(\theta_{\rm hel})$ *and* $\mathcal{C}'_{\rm NB}$ *distributions of* $(B_s^0 \to \phi\gamma)_{B_s^{0*}\bar{B}_s^0}$ *signal. The points with error bars represent the signal MC data and the solid red curve represents the signal MC fit function. The dashed magenta and green curves in the* $M_{\rm bc}$ *and* $\mathcal{C}'_{\rm NB}$ *plots represent the contributions from different Gaussian components.*

Variable	**Function**	**Parameter**	**Value**	**Comment**
$M_{\rm bc}$	Double- Gaussian	Mean (μ) Sigma1 (σ_1) Sigma2 (σ_2) Fraction (f)	5389.42 ± 0.03 MeV/c^2 14.97 ± 0.21 MeV/c^2 4.87 ± 0.04 MeV/c^2 0.20 ± 0.01	Floated Floated Floated Floated
ΔE	CBall function	Mean (μ) Sigma (σ) n alpha (α)	-27.03 ± 0.56 MeV 35.80 ± 0.37 MeV 5.74 ± 0.51 0.55 ± 0.02	Floated Floated Floated Floated
$\cos(\theta_{\rm hel})$	$\sin^2(\theta_{\rm hel})$	No parameter		
$\mathcal{C}'_{\rm NB}$	2 Gaussian functions	Mean1 (μ_1) Sigma1 (σ_1) Mean2 (μ_2) Sigma2 (σ_2) Fraction (f)	0.72 ± 0.08 1.90 ± 0.02 2.60 ± 0.04 1.30 ± 0.02 0.45 ± 0.03	Floated Floated Floated Floated Floated

TABLE 4.3: $(B_s^0 \to \phi\gamma)_{B_s^{0*}\bar{B}_s^0}$ *signal MC parameterizations.*

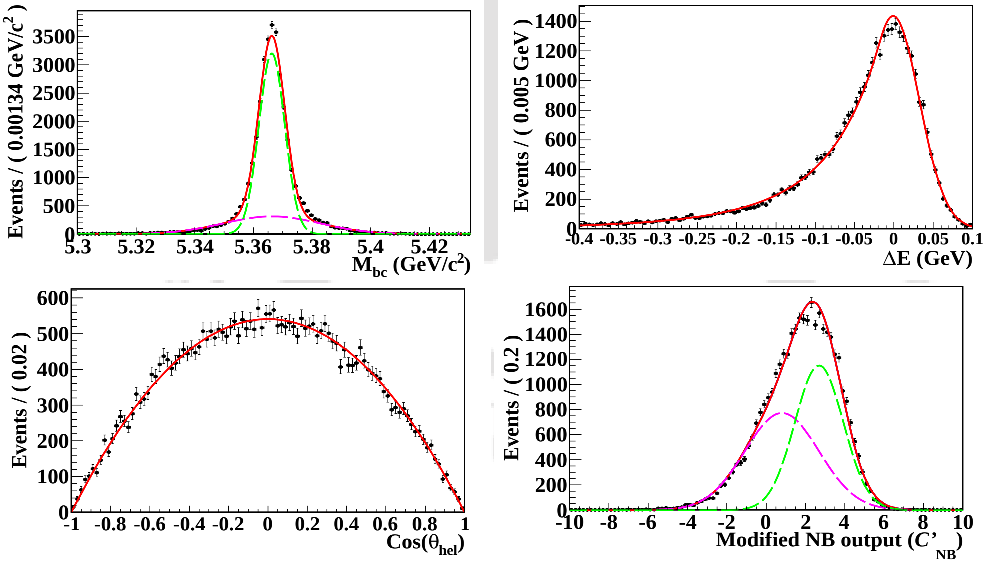

FIGURE 4.4: *Parameterization of* $M_{\rm bc}$, ΔE, $\cos(\theta_{\rm hel})$ *and* $\mathcal{C}'_{\rm NB}$ *distributions of* $(B_s^0 \to \phi\gamma)_{B_s^0\bar{B}_s^0}$ *signal. The points with error bars represent the signal MC data and the solid red curve represents the signal MC fit function. The dashed magenta and green curves in the* $M_{\rm bc}$ *and* $\mathcal{C}'_{\rm NB}$ *plots represent the contributions from different Gaussian components.*

Variable	**Function**	**Parameter**	**Value**	**Comment**
$M_{\rm bc}$	Double-Gaussian	Mean (μ)	5366.26 ± 0.03 MeV/c^2	Floated
		Sigma1 (σ_1)	16.47 ± 0.17 MeV/c^2	Floated
		Sigma2 (σ_2)	4.41 ± 0.03 MeV/c^2	Floated
		Fraction (f)	0.27 ± 0.01	Floated
ΔE	CBall function	Mean (μ)	-0.96 ± 0.59 MeV	Floated
		Sigma (σ)	33.32 ± 0.40 MeV	Floated
		n	5.98 ± 0.50	Floated
		alpha (α)	0.50 ± 0.01	Floated
$\cos(\theta_{\rm hel})$	$\sin^2(\theta_{\rm hel})$	No parameter		
$\mathcal{C}'_{\rm NB}$	2 Gaussian functions	Mean1 (μ_1)	0.80 ± 0.06	Floated
		Sigma1 (σ_1)	1.89 ± 0.02	Floated
		Mean2 (μ_2)	2.69 ± 0.04	Floated
		Sigma2 (σ_2)	1.23 ± 0.02	Floated
		Fraction (f)	0.51 ± 0.02	Floated

TABLE 4.4: $(B_s^0 \to \phi\gamma)_{B_s^0\bar{B}_s^0}$ *signal MC parameterizations.*

The background PDFs are modeled using $q\bar{q}$ background MC sample. The background PDFs are modeled with an Argus function for $M_{\rm bc}$ with its endpoint fixed at 5.434 GeV/c^2, Chebychev first order polynomial for ΔE, a quadratic polynomial for $\cos(\theta_{\rm hel})$ and a Gaussian function for $\mathcal{C}'_{\rm NB}$ (Argus function and Chebychev polynomials are described in

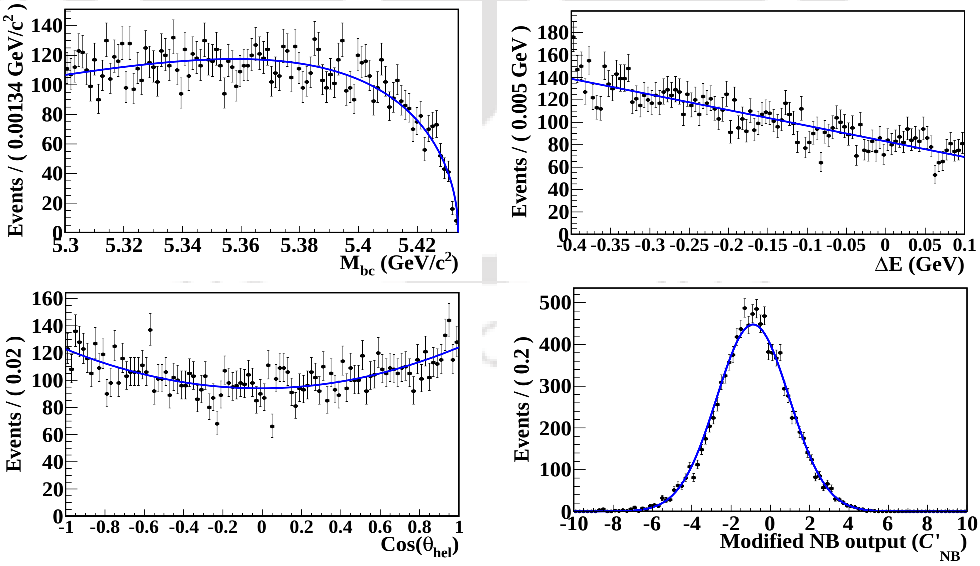

FIGURE 4.5: *Parameterization of* $M_{\rm bc}$, ΔE, $\cos(\theta_{\rm hel})$ *and* $\mathcal{C}'_{\rm NB}$ *distributions of the continuum background. The points with error bars represent the continuum background MC data and the solid blue curve represents the background MC fit function.*

details in Appendix D). The functions and fit parameters for background are summarized in Table 4.5 and the plots are shown in Figure 4.5.

Variable	**Function**	**Parameter**	**Value**	**Comment**
$M_{\rm bc}$	Argus function	Curvature (a_1) Endpoint (a_0)	-17.48 ± 0.75 5434 MeV	Floated Fixed
ΔE	Chebychev polynomial	Coefficient (c_1)	-0.34 ± 0.02	Floated
cos($\theta_{\rm hel}$)	Quadratic polynomial	Coefficient (p_1) Coefficient (p_2)	0.01 ± 0.02 0.31 ± 0.04	Floated Floated
$\mathcal{C}'_{\rm NB}$	Gaussian function	Mean (μ) Sigma (σ)	-0.88±0.02 1.85±0.01	Floated Floated

TABLE 4.5: *Background MC parameterizations for $B_s^0 \to \phi\gamma$ analysis.*

4.2.2 Mean and Resolution Corrections of $(B_s^0 \to \phi\gamma)_{B_s^{0*}\bar{B}_s^{0*}}$ signal

Since MC doesnot resemble the data exactly, we calibrate the $M_{\rm bc}$ and ΔE mean and sigma of $(B_s^0 \to \phi\gamma)_{B_s^{0*}\bar{B}_s^{0*}}$ signal using the $B^0 \to K^{0*}\gamma$ and $B_s^0 \to D_s\pi$ control samples. The calibration is done only for $(B_s^0 \to \phi\gamma)_{B_s^{0*}\bar{B}_s^{0*}}$ signal events since the other signal components are small and we will use only the $(B_s^0 \to \phi\gamma)_{B_s^{0*}\bar{B}_s^{0*}}$ signal yield in the final calculations. We calibrate the M_{bc} mean of $(B_s^0 \to \phi\gamma)_{B_s^{0*}\bar{B}_s^{0*}}$ signal using $M_{\rm bc}$ mean corrections taken from $B_s^0 \to D_s\pi$ analysis. The $B_s^0 \to D_s\pi$ analysis is done at the same Υ(5S) resonance and have much higher statistics. We correct the $M_{\rm bc}$ and ΔE sigma of $(B_s^0 \to \phi\gamma)_{B_s^{0*}\bar{B}_s^{0*}}$ signal using resolution corrections obtained from $B^0 \to K^{0*}\gamma$ analysis done using 562.2 fb^{-1} of Υ(4S) data. The Υ(4S) data were taken in the similar experimental conditions as the Υ(5S) data used in these analyses. $B^0 \to K^{0*}\gamma$ is chosen as a control sample as it has higher statistics and similar final states. The mean and sigma correction factors for $M_{\rm bc}$ and ΔE are estimated using the mean and sigma values from signal MC and real data fit. In the following subsections, we describe these corrections in details.

4.2.2.1 Estimation of Resolution Corrections from $B^0 \to K^{0*}\gamma$

For $B^0 \to K^{0*}\gamma$, we have performed a 2D unbinned extended ML fit involving $M_{\rm bc}$ and ΔE. Before performing the fit, we have applied similar kinematic selection cuts as in our

$B_s^0 \to \phi\gamma$ and $B_s^0 \to \gamma\gamma$ analyses. All these cuts are summarized in Table 3.2. To further reduce the backgrounds, we apply the selection criteria $|\cos(\theta_{\rm hel})| < 0.8$ and $\mathcal{C}'_{\rm NB} > 0.6$. Two components are used in the fit: signal and background. The fit regions for $M_{\rm bc}$ and ΔE are listed below:

- $5.2 < M_{\rm bc} < 5.289$
- $-0.4 < \Delta{\rm E} < 0.2$

We have fitted the $M_{\rm bc}$ and ΔE signals with CBall functions. The continuum background is modeled with an Argus function for $M_{\rm bc}$, the endpoint being fixed at 5.289 GeV/c^2 and a Chebychev first order polynomial for ΔE. The signal and background PDFs and parameters are summarized in Table 4.6 and Table 4.7, and the plots are shown in Figure 4.6 and Figure 4.7, respectively. In fitting the real data, all the signal parameters are kept fixed to MC values except $M_{\rm bc}$ and ΔE mean and sigma. All the background parameters are floated except the Argus endpoint. The sigma correction factors are estimated using the sigma values obtained from the signal MC and 2D real data fits. The details of the real data fits are presented in Table 4.8 and the resolution corrections obtained from the fit is presented in Table 4.9. The real data plots projected over the signal region (5.27 $< M_{\rm bc} <$ 5.289, $-0.1 < \Delta{\rm E} < 0.05$) are shown in Figure 4.8. The fit yields a value of 3033 ± 67 for $B^0 \to K^{0*}\gamma$ signal.

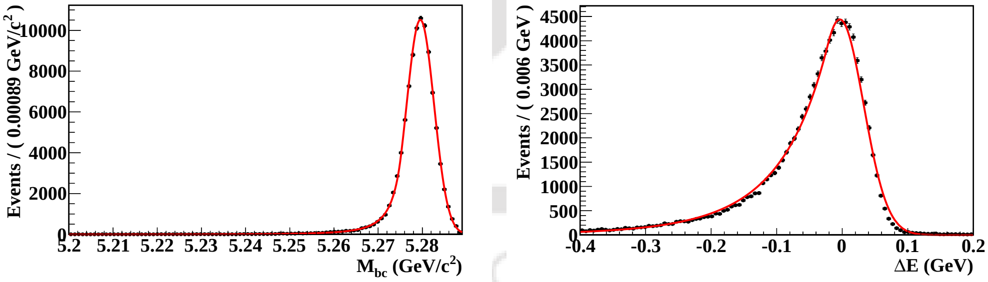

FIGURE 4.6: *Parameterizations of $M_{\rm bc}$ and ΔE distributions of $B^0 \to K^{0*}\gamma$ signal. The points with error bars represent the signal MC data and the solid red curve represents the signal MC fit function.*

We calculate the BF of $B^0 \to K^{0*}\gamma$ using the above signal yield to cross-check our fitting procedure. The BF is calculated as:

$$\mathcal{B}(B^0 \to K^{0*}\gamma) \;=\; \frac{N_{\rm signal}}{\mathcal{B}(K^{*0} \to K^+\pi^-) * \epsilon * N(B\bar{B})}$$

Variable	Function	Parameter	Value	Comment
$M_{\rm bc}$	CBall function	Mean (μ)	5279.55 ± 0.01 MeV/c^2	Floated
		Sigma (σ)	3.10 ± 0.01 MeV/c^2	Floated
		n	3.05 ± 0.07	Floated
		alpha (α)	1.42 ± 0.02	Floated
ΔE	CBall function	Mean (μ)	-3.76 ± 0.22 MeV	Floated
		Sigma (σ)	36.32 ± 0.16 MeV	Floated
		n	9.25 ± 0.35	Floated
		alpha (α)	0.50	Fixed

TABLE 4.6: *Signal MC parameterizations for* $B^0 \to K^{0*}\gamma$.

where, $N_{\rm signal}$ (or $N(B^0 \to K^{0*}\gamma)$) is the signal yield of $B^0 \to K^{0*}\gamma$ signal obtained from the fit; ϵ denotes the signal selection efficiency i.e., the number of signal events remaining after all the cuts; $N(B\bar{B})$ is the number of B meson pairs in the real data sample and $\mathcal{B}(K^{*0} \to K^+\pi^-)$ is the branching fraction of $K^{*0} \to K^+\pi^-$.

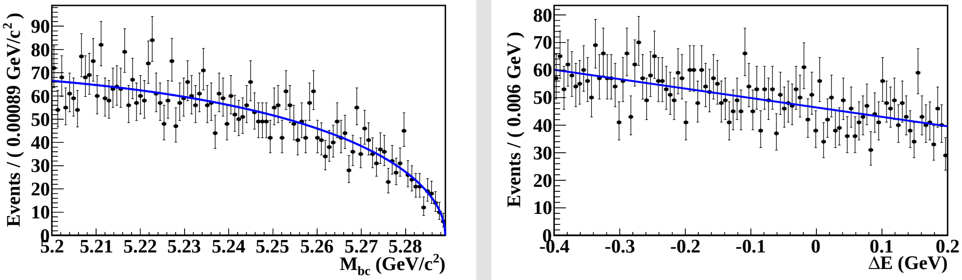

FIGURE 4.7: *Parameterizations of $M_{\rm bc}$ and ΔE distributions of the continuum background. The points with error bars represent the continuum background MC data and the solid blue curve represents the background MC fit function.*

We have obtained a BF of $(4.07 \pm 0.09)\times 10^{-5}$ for the $B^0 \to K^{0*}\gamma$ decay. This result doesnot include the systematic uncertainties. This value is consistent to the world

Variable	Function	Parameter	Value	Comment
$M_{\rm bc}$	Argus function	Curvature (a_1)	-7.91 ± 1.59	Floated
		Endpoint (a_0)	5289 MeV	Fixed
ΔE	Chebychev polynomial	Coefficient (c_1)	-0.21 ± 0.02	Floated

TABLE 4.7: *Background MC parameterizations for* $B^0 \to K^{0*}\gamma$.

average value of $B^0 \to K^{0*}\gamma$ branching fraction, which is $(4.33 \pm 0.15)\times10^{-5}$ [34]. The $B^0 \to K^{0*}\gamma$ results along with their uncertainties have been summarized in Table 4.10.

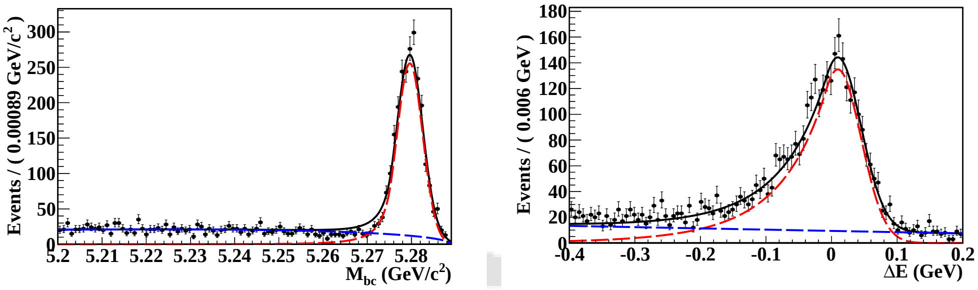

FIGURE 4.8: Data distributions for $M_{\rm bc}$ and ΔE variables for $B^0 \to K^{0*}\gamma$. The points with error bars represent the data, the solid black curve represents the total fit function and the red dashed (blue dashed) curve represents the signal (continuum background) contribution.

Variable		Function	Parameter	Value	Comment
$M_{\rm bc}$	Signal	CBall function	Mean (μ)	5279.63 ± 0.07 MeV/c^2	Floated
			Sigma (σ)	2.92 ± 0.06 MeV/c^2	Floated
			n	3.05	Fixed(MC)
			alpha (α)	1.42	Fixed(MC)
	Background	Argus function	Curvature (a_1)	-19.31 ± 1.53	Floated
			Endpoint (a_0)	5289 MeV/c^2	Fixed(MC)
ΔE	Signal	CBall function	Mean (μ)	9.55 ± 1.19 MeV	Floated
			Sigma (σ)	35.35 ± 0.96 MeV	Floated
			n	9.25	Fixed(MC)
			alpha (α)	0.50	Fixed
	Background	Chebychev polynomial	Coefficient (c_1)	-0.28 ± 0.02	Floated
	Yields		$N_{\rm signal}$	3033.17 ± 67.16	Floated
			$N_{\rm background}$	7823.91 ± 96.43	Floated

TABLE 4.8: *Real data fit results for $B^0 \to K^{0*}\gamma$.*

4.2.2.2 $M_{\rm bc}$ Mean Correction Factor from $B_s^0 \to D_s\pi$ Analysis

We have obtained the $M_{\rm bc}$ mean corrections for $B_s^{0*}\bar{B}_s^{0*}$ signal from $B_s^0 \to D_s\pi$ analysis [101, 102]. The correction factor is 4.47 ± 0.15 MeV.

Variable	Sigma(MC)	Sigma(Data)	Correction
$M_{\rm bc}$	3.10 ± 0.01 MeV/c^2	2.92 ± 0.06 MeV/c^2	0.94 ± 0.02
ΔE	36.32 ± 0.16 MeV	35.35 ± 0.96 MeV	0.97 ± 0.03

TABLE 4.9: *Resolution corrections for* $M_{\rm bc}$ *and* ΔE *from* $B^0 \to K^{0*}\gamma$.

Parameter	Value
$N(B^0 \to K^{0*}\gamma)$	3033 ± 67
ϵ	(19.7 ± 0.1)%
$N(B\bar{B})$	(576.66 ± 9.44)×10^6
$B(K^{*0} \to K^+\pi^-)$	0.6626
$\mathrm{B}(B^0 \to K^{0*}\gamma)$	(4.07 ± 0.09)×10^{-5}
$\mathrm{B}(B^0 \to K^{0*}\gamma)$ ([34])	(4.33 ± 0.15)×10^{-5}

TABLE 4.10: *Results of* $B^0 \to K^{0*}\gamma$.

4.2.2.3 Calibrating the $M_{\rm bc}$ Mean and the $M_{\rm bc}$, ΔE Resolutions of $(B_s^0 \to \phi\gamma)_{B_s^{0*}\bar{B}_s^{0*}}$ Signal

We have calibrated the $M_{\rm bc}$ mean, $M_{\rm bc}$ and ΔE sigma of $(B_s^0 \to \phi\gamma)_{B_s^{0*}\bar{B}_s^{0*}}$ signal using the correction factors presented in sections 4.2.2.2 and 4.2.2.1, respectively which are presented in Tables 4.11 and 4.12, respectively.

Variable	Mean(MC)	Correction	Corrected Mean
$M_{\rm bc}$ (in MeV/c^2)	5412.43 ± 0.03	4.47 ± 0.15	5416.90 ± 0.15

TABLE 4.11: *Correction of* $M_{\rm bc}$ *mean for* $(B_s^0 \to \phi\gamma)_{B_s^{0*}\bar{B}_s^{0*}}$ *signal.*

Variable	Sigma(MC)	Correction	Corrected Sigma
$M_{\rm bc}$	4.71 ± 0.02 MeV/c^2	0.94 ± 0.02	4.43 ± 0.10 MeV/c^2
ΔE	36.70 ± 0.38 MeV	0.97 ± 0.03	35.72 ± 1.07 MeV

TABLE 4.12: *Correction of* $M_{\rm bc}$ *and* ΔE *sigma for* $(B_s^0 \to \phi\gamma)_{B_s^{0*}\bar{B}_s^{0*}}$ *signal.*

4.2.3 Real Data Fit PDF

The total PDF for each component is created by taking the product of the individual 1D PDFs. The final PDF is then formed by adding the PDFs of all four components. All the signal parameters except the mean and width of $M_{\rm bc}$ and ΔE distributions of $(B_s^0 \to \phi\gamma)_{B_s^{0*}\bar{B}_s^{0*}}$ signal are kept fixed to the MC values. The $M_{\rm bc}$ mean, sigma and the ΔE sigma of $(B_s^0 \to \phi\gamma)_{B_s^{0*}\bar{B}_s^{0*}}$ signal are fixed to the corrected mean and sigma values presented in section 4.2.2.3. The ΔE mean of $(B_s^0 \to \phi\gamma)_{B_s^{0*}\bar{B}_s^{0*}}$ signal and all background parameters except the Argus endpoint are floated. The signal and background yields are also floated. The fit has 11 floated parameters:

- ΔE mean.
- Argus and Chebychev background parameters.
- Both parameters of $\cos(\theta_{\rm hel})$ background.
- Both mean and sigma of $\mathcal{C}'_{\rm NB}$ background.
- $B_s^0 \to \phi\gamma$ signal yields from $B_s^{0*}\bar{B}_s^{0*}$, $B_s^{0*}\bar{B}_s^0$ and $B_s^0\bar{B}_s^0$ decays.
- Background yield.

4.2.4 Fit Validation Using Toy MC

We perform toy studies to validate our fit procedure. We generate pure toy events according to our fit PDFs by fixing all parameters including the background parameters and yields of signal and background components. We perform toy studies for different $(B_s^0 \to \phi\gamma)_{B_s^{0*}\bar{B}_s^{0*}}$ signal events. The yields of $(B_s^0 \to \phi\gamma)_{B_s^{0*}\bar{B}_s^0}$ and $(B_s^0 \to \phi\gamma)_{B_s^0\bar{B}_s^0}$ signals for each case are fixed according to $(B_s^0 \to \phi\gamma)_{B_s^{0*}\bar{B}_s^{0*}}$ signal yield and fraction of $B_s^{0*}\bar{B}_s^0$ and $B_s^0\bar{B}_s^0$ events at $\Upsilon(5S)$. We fix the background yield to the expected background events. We then fit these pseudo events with our fit PDF. For each case, we generate and fit 5,000 toy events and obtain the fit yield and residual (where, residual = fit yield - actual yield) distributions of $(B_s^0 \to \phi\gamma)_{B_s^{0*}\bar{B}_s^{0*}}$ signal. We then fit the $(B_s^0 \to \phi\gamma)_{B_s^{0*}\bar{B}_s^{0*}}$ signal residual mean with a linear polynomial to check the stability of the fitter. From our studies the fitter seems to be stable. The toy results for $(B_s^0 \to \phi\gamma)_{B_s^{0*}\bar{B}_s^{0*}}$ signal are shown in Figure 4.9 for $N_{B_s^{0*}\bar{B}_s^{0*}} = 80$, $N_{B_s^{0*}\bar{B}_s^{0}} = 7$, $N_{B_s^{0}\bar{B}_s^{0}} = 5$ and $N_{\mathrm{background}} = 1876$.

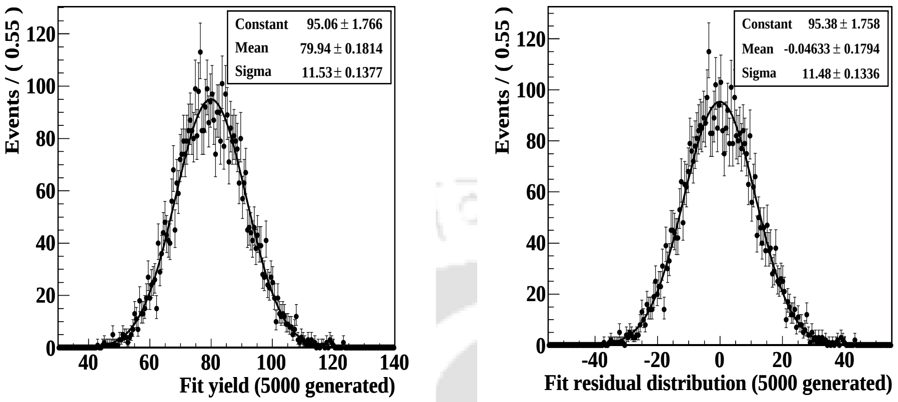

FIGURE 4.9: *Fit yield and residual distributions of* $(B_s^0 \to \phi\gamma)_{B_s^{0*}\bar{B}_s^{0*}}$ *signal. Toy MC events generated with* $N_{B_s^{0*}\bar{B}_s^{0*}} = 80$, $N_{B_s^{0*}\bar{B}_s^{0}} = 7$, $N_{B_s^{0}\bar{B}_s^{0}} = 5$ & $N_{\mathrm{background}} = 1876$.

The fit residual values for different $(B_s^0 \to \phi\gamma)_{B_s^{0*}\bar{B}_s^{0*}}$ signals are plotted and fitted with a linear polynomial to check the stability of the fitter. The fitted $(B_s^0 \to \phi\gamma)_{B_s^{0*}\bar{B}_s^{0*}}$ signal residual distribution is shown in Figure 4.10. We obtain a fit bias of 0.08 ± 0.01 from the fitted signal residual mean. The observed bias is corrected and its uncertainty is assigned as an additive systematic uncertainty.

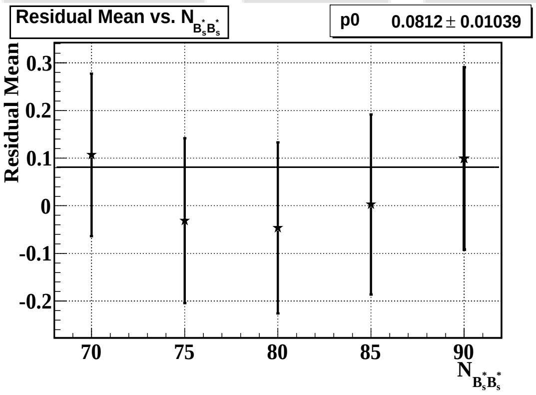

FIGURE 4.10: *Fitted residual distribution of* $(B_s^0 \to \phi\gamma)_{B_s^{0*}\bar{B}_s^{0*}}$ *signal.*

4.2.5 Fit Results for 121.4 fb^{-1} Real Data Sample

The Υ(5S) dataset is unblinded with the fit strategy described in section 4.2.3 to extract the signal and background yields. Details of the fit are listed in Table 4.13 and the fit plots

Variable		Function	Parameter	Value	Comment
$M_{\rm bc}$	Signal ($B_s^{0*}\bar{B}_s^{0*}$)	CBall function	Mean (μ)	5416.90 MeV/c^2	Fixed(Corr. Value)
			Sigma (σ)	4.43 MeV/c^2	Fixed(Corr. Value)
			n	4.59	Fixed(MC Value)
			alpha (α)	1.52	Fixed(MC Value)
	Signal ($B_s^{0*}\bar{B}_s^{0}$)	Double-Gaussian function	Mean1 (μ_1)	5389.42 MeV/c^2	Fixed(MC Value)
			Sigma1 (σ_1)	14.97 MeV/c^2	Fixed(MC Value)
			Sigma2 (σ_2)	4.87 MeV/c^2	Fixed(MC Value)
			Fraction (f)	0.20	Fixed(MC Value)
	Signal ($B_s^{0}\bar{B}_s^{0}$)	Double-Gaussian function	Mean1 (μ_1)	5366.26 MeV/c^2	Fixed(MC Value)
			Sigma1 (σ_1)	16.47 MeV/c^2	Fixed(MC Value)
			Sigma2 (σ_2)	4.41 MeV/c^2	Fixed(MC Value)
			Fraction (f)	0.27	Fixed(MC Value)
	Background	Argus function	Curvature (a_1)	$-14.94^{+1.85}_{-1.84}$	Floated
			Endpoint (a_0)	5434 MeV/c^2	Fixed(MC Value)
ΔE	Signal ($B_s^{0*}\bar{B}_s^{0*}$)	CBall function	Mean (μ)	$-47.73^{+6.87}_{-6.96}$ MeV	Floated
			Sigma (σ)	35.72 MeV	Fixed(Corr. Value)
			n	5.15	Fixed(MC Value)
			alpha (α)	0.57	Fixed(MC Value)
	Signal ($B_s^{0*}\bar{B}_s^{0}$)	CBall function	Mean (μ)	-27.03 MeV	Fixed(MC Value)
			Sigma (σ)	35.80 MeV	Fixed(MC Value)
			n	5.74	Fixed(MC Value)
			alpha (α)	0.55	Fixed(MC Value)
	Signal ($B_s^{0}\bar{B}_s^{0}$)	CBall function	Mean (μ)	-0.96 MeV	Fixed(MC Value)
			Sigma (σ)	33.32 MeV	Fixed(MC Value)
			n	5.98	Fixed(MC Value)
			alpha (α)	0.50	Fixed(MC Value)
	Background	Chebychev polynomial	Coefficient (c_1)	-0.33 ± 0.04	Floated
$\cos(\theta_{\rm hel})$	$B_s^{0*}\bar{B}_s^{0*}$, $B_s^{0*}\bar{B}_s^{0}$& $B_s^{0}\bar{B}_s^{0}$ signals	$\sin^2(\theta_{\rm hel})$	No parameter		
	Background	Quadratic polynomial	Coefficient (p_1)	0.02 ± 0.04	Floated
			Coefficient (p_2)	$0.004^{+0.080}_{-0.075}$	Floated
$\mathcal{C}'_{\rm NB}$	Signal ($B_s^{0*}\bar{B}_s^{0*}$)	2 Gaussian functions	Mean1 (μ_1)	0.90	Fixed(MC Value)
			Sigma1 (σ_1)	1.86	Fixed(MC Value)
			Mean2 (μ_2)	2.77	Fixed(MC Value)
			Sigma2 (σ_2)	1.23	Fixed(MC Value)
			Fraction (f)	0.52	Fixed(MC Value)
	Signal ($B_s^{0*}\bar{B}_s^{0}$)	2 Gaussian functions	Mean1 (μ_1)	0.72	Fixed(MC Value)
			Sigma1 (σ_1)	1.90	Fixed(MC Value)
			Mean2 (μ_2)	2.60	Fixed(MC Value)
			Sigma2 (σ_2)	1.30	Fixed(MC Value)
			Fraction (f)	0.45	Fixed(MC Value)
	Signal ($B_s^{0}\bar{B}_s^{0}$)	2 Gaussian functions	Mean1 (μ_1)	0.80	Fixed(MC Value)
			Sigma1 (σ_1)	1.89	Fixed(MC Value)
			Mean2 (μ_2)	2.69	Fixed(MC Value)
			Sigma2 (σ_2)	1.23	Fixed(MC Value)
			Fraction (f)	0.51	Fixed(MC Value)
	Background	Gaussian function	Mean (μ)	-0.79 ± 0.04	Floated
			Sigma (σ)	1.81 ± 0.03	Floated
	Yields		$N_{B_s^{0*}\bar{B}_s^{0*}}$	$80.49^{+12.10}_{-11.30}$	Floated
			$N_{B_s^{0*}\bar{B}_s^{0}}$	$7.02^{+7.13}_{-5.75}$	Floated
			$N_{B_s^{0}\bar{B}_s^{0}}$	$-8.63^{+6.53}_{-5.09}$	Floated
			$N_{\rm background}$	$1878.10^{+45.20}_{-44.60}$	Floated

TABLE 4.13: *Real data fit results for $B_s^0 \to \phi\gamma$ analysis.*

are shown in Figure 4.11. The real data fits are shown projected over the $(B_s^0 \to \phi\gamma)_{B_s^{0*}\bar{B}_s^{0*}}$ signal regions:

- $M_{\rm bc}$ ⟶ (5.4 - 5.434) GeV/c^2
- ΔE ⟶ (-0.2 - 0.02) GeV
- $\cos(\theta_{\rm hel})$ ⟶ (-0.8 - 0.8)
- $\mathcal{C}'_{\rm NB}$ ⟶ (0.0 - 10.0)

The fit yields 80^{+12}_{-11}, 7^{+7}_{-6} and -9^{+7}_{-5} $B_s^0 \to \phi\gamma$ signal events coming from $B_s^{0*}\bar{B}_s^{0*}$, $B_s^{0*}\bar{B}_s^0$ and $B_s^0\bar{B}_s^0$ decays and 1878^{+45}_{-44} background events.

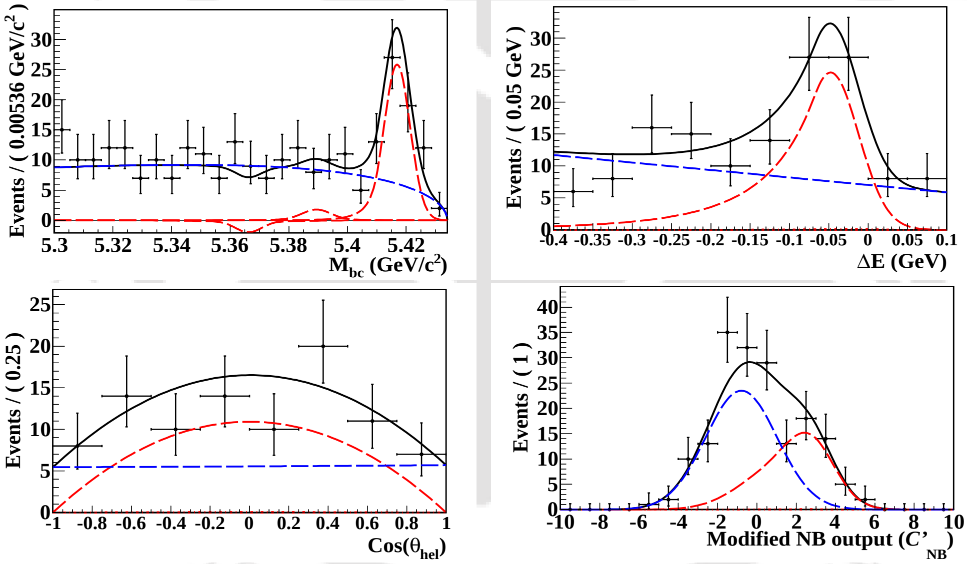

FIGURE 4.11: *Data distributions for $M_{\rm bc}$, ΔE, $\cos(\theta_{\rm hel})$ and $\mathcal{C}'_{\rm NB}$ variables for $B_s^0 \to \phi\gamma$ analysis. The points with error bars represent the data, the solid black curve represents the total fit function and the red dashed (blue dashed) curve represents the signal (continuum background) contribution.*

4.3 Fit Procedure for $B_s^0 \to \gamma\gamma$

We have performed a 2D unbinned extended ML fit involving $M_{\rm bc}$ and ΔE to extract the $B_s^0 \to \gamma\gamma$ signals in the three signal regions. Similar to $B_s^0 \to \phi\gamma$ case, four components are used in the fitting: signals coming from $B_s^{0*}\bar{B}_s^{0*}$, $B_s^{0*}\bar{B}_s^0$, $B_s^0\bar{B}_s^0$ decays (i.e., $(B_s^0 \to \gamma\gamma)_{B_s^{0*}\bar{B}_s^{0*}}$, $(B_s^0 \to \gamma\gamma)_{B_s^{0*}\bar{B}_s^0}$ and $(B_s^0 \to \gamma\gamma)_{B_s^0\bar{B}_s^0}$ signals) and $q\bar{q}$ background. The correlation between the fit variables are checked and no strong correlation is observed. The plots are presented in Figure 4.12(a), (b), (c) and (d) for $(B_s^0 \to \gamma\gamma)_{B_s^{0*}\bar{B}_s^{0*}}$, $(B_s^0 \to \gamma\gamma)_{B_s^{0*}\bar{B}_s^0}$, $(B_s^0 \to \gamma\gamma)_{B_s^0\bar{B}_s^0}$ signals and $q\bar{q}$ background, respectively and the values are presented in Table 4.14. The contribution from generic-B_s and non-B_s backgrounds are checked and found to be negligible as reported in Chapter 3 and Appendix C. For $B_s^0 \to \gamma\gamma$ analysis, the fit regions chosen for $M_{\rm bc}$ and ΔE are listed below:

- $M_{\rm bc}$ ⟶ (5.3 - 5.434) GeV/c^2
- ΔE ⟶ (-0.7 - 0.4) GeV

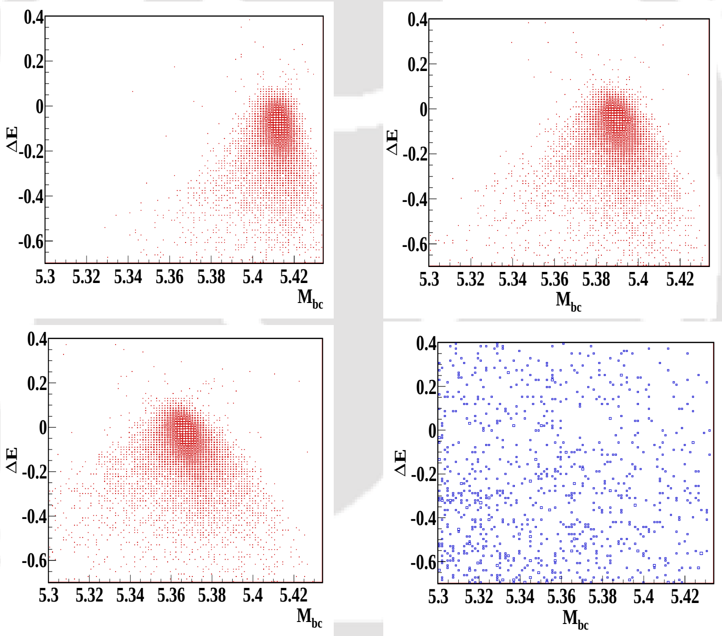

FIGURE 4.12: *Correlation between $M_{\rm bc}$ and ΔE for $B_s^0 \to \gamma\gamma$ analysis. Plots of (a) $(B_s^0 \to \gamma\gamma)_{B_s^{0*}\bar{B}_s^{0*}}$, (b) $(B_s^0 \to \gamma\gamma)_{B_s^{0*}\bar{B}_s^0}$, (c) $(B_s^0 \to \gamma\gamma)_{B_s^0\bar{B}_s^0}$ signal and (d) continuum ($q\bar{q}$) background.*

Variables	**Correlation Factor (%)**			
	(Signal)$_{B_s^{0*}\bar{B}_s^{0*}}$	**(Signal)**$_{B_s^{0*}\bar{B}_s^0}$	**(Signal)**$_{B_s^0\bar{B}_s^0}$	**Background**
$\boldsymbol{M_{\rm bc}}$**:**$\boldsymbol{\Delta}$**E**	15.51	2.44	-15.39	-0.34

TABLE 4.14: *Values of correlation between $M_{\rm bc}$ and ΔE for $B_s^0 \to \gamma\gamma$ analysis.*

4.3.1 Signal and Background PDFs

The signal and the background PDFs are modeled using signal MC and background MC samples, respectively. The $M_{\rm bc}$ distributions are parameterized with a combination of CBall and Gaussian functions having common means for $(B_s^0 \to \gamma\gamma)_{B_s^{0*}\bar{B}_s^{0*}}$ and $(B_s^0 \to \gamma\gamma)_{B_s^{0*}\bar{B}_s^0}$ signals and with a double-Gaussian function for $(B_s^0 \to \phi\gamma)_{B_s^0\bar{B}_s^0}$ signal. The ΔE distributions of all three signals are modeled with CBall functions. The functions and fit parameters for different signals are summarized in Tables 4.15, 4.16 and 4.17 and the plots are shown in Figures 4.13, 4.14 and 4.15.

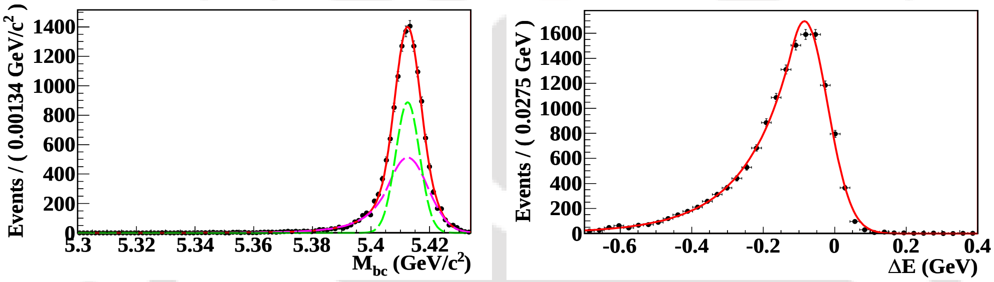

FIGURE 4.13: *Parameterizations of $M_{\rm bc}$ and ΔE distributions of $(B_s^0 \to \gamma\gamma)_{B_s^{0*}\bar{B}_s^{0*}}$ signal. The points with error bars represent the signal MC data and the solid red curve represents the signal MC fit function. The dashed magenta (green) curves in the $M_{\rm bc}$ plot represent the CBall (Gaussian) contributions.*

Variable	Function	Parameter	Value	Comment
$M_{\rm bc}$	CBall + Gaussian	Mean (μ) Sigma1 (σ_1) n alpha (α) Sigma2 (σ_2) f	5412.47 ± 0.06 MeV/c^2 6.89 ± 0.21 MeV/c^2 7.17 ± 1.56 1.01 ± 0.07 MeV/c^2 4.07 ± 0.15 0.52 ± 0.05	Floated Floated Floated Floated Floated Floated
ΔE	CBall function	Mean (μ) Sigma (σ) n alpha (α)	-84.59 ± 1.6 MeV 64.97 ± 1.04 MeV 23.17 ± 12.43 0.50 ± 0.02	Floated Floated Floated Floated

TABLE 4.15: $(B_s^0 \to \gamma\gamma)_{B_s^{0*}\bar{B}_s^{0*}}$ *signal MC parameterizations.*

The M_{bc} background is modeled with an Argus function with its endpoint fixed at 5.434 GeV/c^2 and the ΔE background is modeled with a Chebychev first order polynomial. The functions and fit parameters for background are summarized in Table 4.18 and the plots are shown in Figure 4.16.

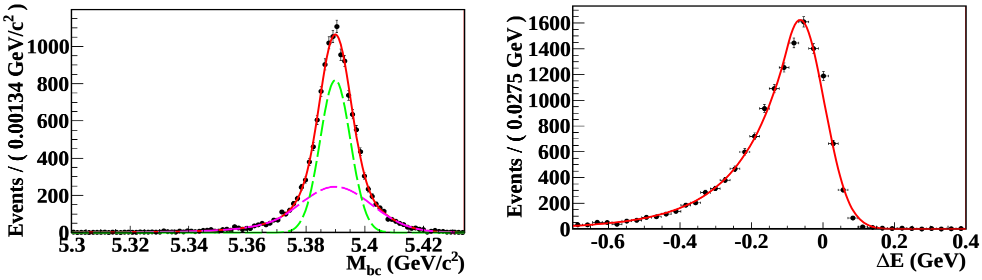

FIGURE 4.14: *Parameterizations of $M_{\rm bc}$ and ΔE distributions of $(B_s^0 \to \gamma\gamma)_{B_s^{0*}\bar{B}_s^0}$ signal. The points with error bars represent the signal MC data and the solid red curve represents the signal MC fit function. The dashed magenta (green) curves in the $M_{\rm bc}$ plot represent the CBall (Gaussian) contributions.*

Variable	Function	Parameter	Value	Comment
$M_{\rm bc}$	CBall + Gaussian	Mean (μ)	5389.92 ± 0.07 MeV/c^2	Floated
		Sigma1 (σ_1)	12.46 ± 0.29 MeV/c^2	Floated
		n	5.11 ± 1.33	Floated
		alpha (α)	1.36 ± 0.09 MeV/c^2	Floated
		Sigma2 (σ_2)	5.17 ± 0.12	Floated
		f	0.43 ± 0.02	Floated
ΔE	CBall function	Mean (μ)	-63.78 ± 1.66 MeV	Floated
		Sigma (σ)	67.30 ± 1.07 MeV	Floated
		n	15.79 ± 5.67	Floated
		alpha (α)	0.52 ± 0.02	Floated

TABLE 4.16: *$(B_s^0 \to \gamma\gamma)_{B_s^{0*}\bar{B}_s^0}$ signal MC parameterizations.*

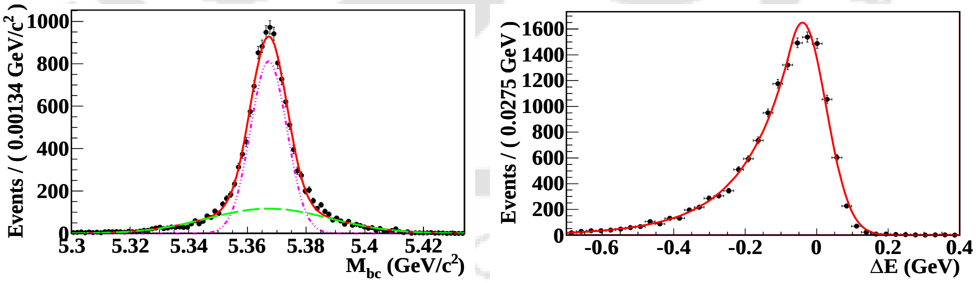

FIGURE 4.15: *Parameterizations of $M_{\rm bc}$ and ΔE distributions of $(B_s^0 \to \gamma\gamma)_{B_s^0\bar{B}_s^0}$ signal. The dashed magenta and green curves in the $M_{\rm bc}$ plot represent the contributions from different Gaussian components.*

Variable	Function	Parameter	Value	Comment
$M_{\rm bc}$	Double-Gaussian	Mean (μ)	5367.25 ± 0.08 MeV/c^2	Floated
		Sigma1 (σ_1)	6.20 ± 0.10 MeV/c^2	Floated
		Sigma2 (σ_2)	20.80 ± 0.35 MeV/c^2	Floated
		Fraction (f)	0.68 ± 0.01	Floated
ΔE	CBall function	Mean (μ)	-39.90 ± 1.63 MeV	Floated
		Sigma (σ)	65.96 ± 1.05 MeV	Floated
		n	19.07 ± 7.54	Floated
		alpha (α)	0.51 ± 0.02	Floated

TABLE 4.17: *$(B_s^0 \to \gamma\gamma)_{B_s^0\bar{B}_s^0}$ signal MC parameterizations.*

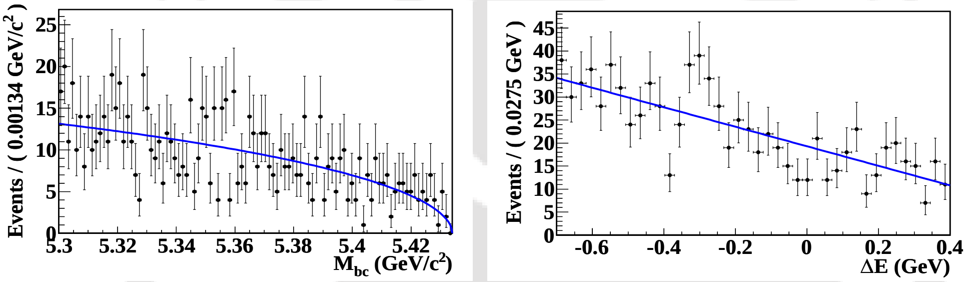

FIGURE 4.16: *Parameterization of $M_{\rm bc}$ and ΔE distributions of the continuum background. The points with error bars represent the continuum background MC data and the solid blue curve represents the background MC fit function.*

Variable	Function	Parameter	Value	Comment
$M_{\rm bc}$	Argus function	Curvature (a_1)	-0.70 ± 2.61	Floated
		Endpoint (a_0)	5434 MeV	Fixed
ΔE	Chebychev polynomial	Coefficient (c_1)	-0.52 ± 0.05	Floated

TABLE 4.18: *Background MC parameterizations for $B_s^0 \to \gamma\gamma$ analysis.*

4.3.2 Mean and Resolution Corrections of $(B_s^0 \to \gamma\gamma)_{B_s^{0*}\bar{B}_s^{0*}}$ Signal

Similar to the $B_s^0 \to \phi\gamma$ case, we have calibrated the $M_{\rm bc}$ and ΔE mean and sigma of $(B_s^0 \to \gamma\gamma)_{B_s^{0*}\bar{B}_s^{0*}}$ signal using the results from $B_s^0 \to D_s\pi$, $B_s^0 \to \phi\gamma$ and $B^0 \to K^{0*}\gamma$ analysis. We have calibrated the $M_{\rm bc}$ mean using $M_{\rm bc}$ mean corrections taken from $B_s^0 \to D_s\pi$ and have calibrated $M_{\rm bc}$ and ΔE sigma using resolution corrections taken from $B^0 \to K^{0*}\gamma$. We have estimated the ΔE mean correction factor from $B_s^0 \to \phi\gamma$ to correct the ΔE mean of $(B_s^0 \to \gamma\gamma)_{B_s^{0*}\bar{B}_s^{0*}}$ signal. In the following subsections, we describe the estimation of ΔE mean correction factor and the calibrations in detail.

4.3.2.1 Estimation of ΔE Mean Correction Factor from $B_s^0 \to \phi\gamma$ Analysis

Both the decays $B_s^0 \to \phi\gamma$ and $B_s^0 \to \gamma\gamma$ are radiative penguin decays involving a photon in their final state. Since their final states are similar and both decays are produced at Υ(5S) resonance, so we have planned to correct the ΔE mean for the $(B_s^0 \to \gamma\gamma)_{B_s^{0*}\bar{B}_s^{0*}}$ signal using the ΔE mean corrections taken from $(B_s^0 \to \phi\gamma)_{B_s^{0*}\bar{B}_s^{0*}}$ analysis. The ΔE mean correction factor is estimated from the ΔE mean values of $(B_s^0 \to \phi\gamma)_{B_s^{0*}\bar{B}_s^{0*}}$ signal, obtained from signal MC and real data fit of $B_s^0 \to \phi\gamma$ analysis. The correction factor is presented in Table 4.19.

Variable	Mean(MC)	Mean(Data)	Correction Factor
ΔE	-50.32 ± 0.59 MeV	$-47.73^{+6.87}_{-6.96}$ MeV	$2.59^{+6.90}_{-6.98}$ MeV

TABLE 4.19: *Mean correction factor for ΔE from $B_s^0 \to \phi\gamma$ analysis.*

4.3.2.2 Calibrating the $M_{\rm bc}$ Mean and the $M_{\rm bc}$, ΔE Resolutions of $(B_s^0 \to \gamma\gamma)_{B_s^{0*}\bar{B}_s^{0*}}$ Signal

For the $B_s^0 \to \gamma\gamma$ decay, where B_s^0 is produced from $B_s^{0*}\bar{B}_s^{0*}$ decay, we have calibrated the mean of $M_{\rm bc}$ and sigma of $M_{\rm bc}$ and ΔE using the correction factors presented in sections 4.2.2.2 and 4.2.2.1, respectively. The corrected mean and sigma values are presented in Tables 4.20 and 4.21, respectively.

Variable	Mean(MC)	Correction	Corrected Mean
$M_{\rm bc}$ (in MeV/c^2)	5412.47 ± 0.06	4.47 ± 0.15	5416.94 ± 0.16

TABLE 4.20: *Correction of $M_{\rm bc}$ mean for $(B_s^0 \to \gamma\gamma)_{B_s^{0*}\bar{B}_s^{0*}}$ signal.*

Variable	Sigma(MC)	Correction	Corrected Sigma
$M_{\rm bc}$ σ_1	6.89 ± 0.21 MeV/c^2	0.94 ± 0.02	6.47 ± 0.24 MeV/c^2
$M_{\rm bc}$ σ_2	4.07 ± 0.15 MeV/c^2	0.94 ± 0.02	3.82 ± 0.16 MeV/c^2
ΔE	64.97 ± 1.04 MeV	0.97 ± 0.03	63.02 ± 2.19 MeV

TABLE 4.21: *Correction of $M_{\rm bc}$ and ΔE sigma for $(B_s^0 \to \gamma\gamma)_{B_s^{0*}\bar{B}_s^{0*}}$ signal.*

4.3.3 Real Data Fit PDF

The total PDF for each component is created by taking the product of individual 1D PDFs. The final PDF is then formed by adding the PDFs of all four components. All the signal parameters except $M_{\rm bc}$ and ΔE mean and sigma of $(B_s^0 \to \gamma\gamma)_{B_s^{0*}\bar{B}_s^{0*}}$ signal are kept fixed to MC values. The $M_{\rm bc}$ mean, sigma and the ΔE sigma of $(B_s^0 \to \gamma\gamma)_{B_s^{0*}\bar{B}_s^{0*}}$ signal are fixed to the corrected mean and sigma values presented in section 4.3.2.2. The ΔE mean of $(B_s^0 \to \gamma\gamma)_{B_s^{0*}\bar{B}_s^{0*}}$ signal is fixed to the MC value as the calibration factor is well within the statistical uncertainties. The uncertainty associated with this procedure is included as systematics in the $B_s^0 \to \gamma\gamma$ analysis. All background parameters are floated except the Argus endpoint. The fit has 6 floated parameters:

- Argus and Chebychev background parameters.
- $B_s^0 \to \phi\gamma$ signal yields from $B_s^{0*}\bar{B}_s^{0*}$, $B_s^{0*}\bar{B}_s^0$ and $B_s^0\bar{B}_s^0$ decays.
- Background yield.

4.3.4 Fit Validation Using Toy MC

We perform toy studies to validate our fit procedure. We generate pure toy events according to our fit PDFs by fixing all parameters including the background parameters and yields of signal and background components. The yields of $(B_s^0 \to \gamma\gamma)_{B_s^{0*}\bar{B}_s^{0*}}$,

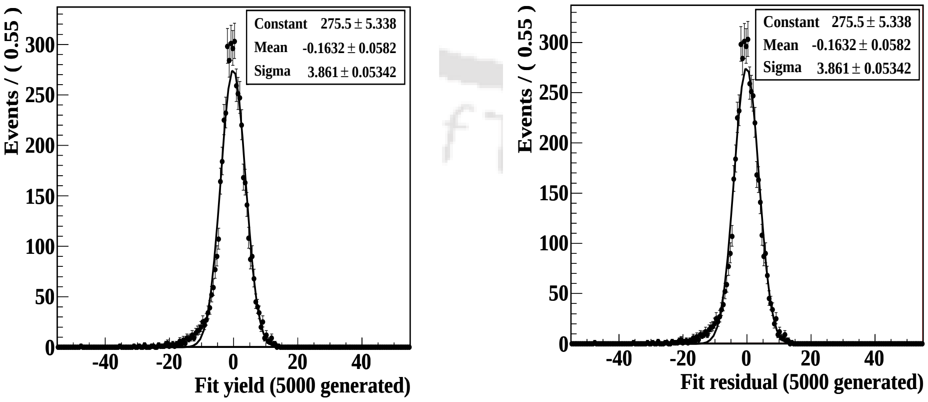

FIGURE 4.17: *Fit yield and residual distributions of* $(B_s^0 \to \gamma\gamma)_{B_s^{0*}\bar{B}_s^{0*}}$ *signal. Toy MC events generated with* $N_{B_s^{0*}\bar{B}_s^{0*}} = 0$, $N_{B_s^{0*}\bar{B}_s^0} = 0$, $N_{B_s^0\bar{B}_s^0} = 0$ & $N_{\rm background} = 331$.

$(B_s^0 \to \gamma\gamma)_{B_s^{0*}\bar{B}_s^0}$ and $(B_s^0 \to \gamma\gamma)_{B_s^0\bar{B}_s^0}$ signals are fixed to the expected signal (i.e., to 0). We fix the background yield to the total expected background. We generate and fit 5,000 such events and obtain the return fit yield and the residual distributions of $(B_s^0 \to \gamma\gamma)_{B_s^{0*}\bar{B}_s^{0*}}$ signal. From our studies the fitter seems to be stable. The toy results for $(B_s^0 \to \gamma\gamma)_{B_s^{0*}\bar{B}_s^{0*}}$ signal are shown in Figure 4.17 for $N_{B_s^{0*}\bar{B}_s^{0*}} = 0$, $N_{B_s^{0*}\bar{B}_s^0} = 0$, $N_{B_s^0\bar{B}_s^0} = 0$ and $N_{\text{background}} = 331$. From the residual mean distribution of $(B_s^0 \to \gamma\gamma)_{B_s^{0*}\bar{B}_s^{0*}}$ signal, we have obtained a fit bias of -0.16 ± 0.06. The uncertainty in the bias (± 0.1) is assigned as an additive systematic uncertainty.

4.3.5 Fit Results for 121.4 fb^{-1} Real Data Sample

The Υ(5S) dataset is unblinded with the fit strategy described in section 4.3.3 to extract the signal and background yields. Details of the fit are listed in Table 4.22 and the fit plots are shown in Figure 4.18. The real data fits are shown projected over the $(B_s^0 \to \gamma\gamma)_{B_s^{0*}\bar{B}_s^{0*}}$ signal regions:

- M_{bc} $\longrightarrow$ (5.4 - 5.434) GeV/c^2
- ΔE $\longrightarrow$ (-0.3 - 0.05) GeV

The fit yields -3^{+3}_{-2}, -6^{+5}_{-4} and 11^{+8}_{-7} $B_s^0 \to \gamma\gamma$ signal events coming from $B_s^{0*}\bar{B}_s^{0*}$, $B_s^{0*}\bar{B}_s^0$ and $B_s^0\bar{B}_s^0$ decays and 329 ± 20 background events.

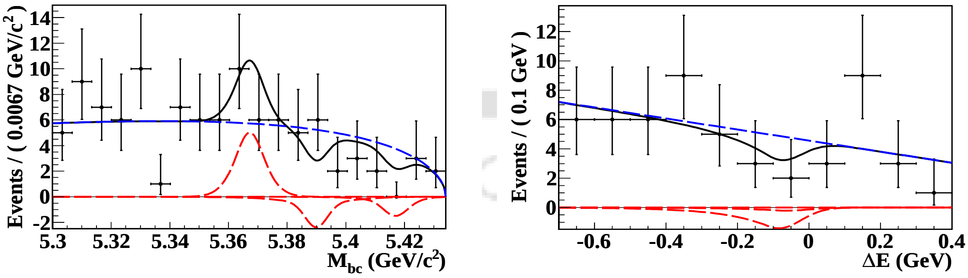

FIGURE 4.18: *Data distributions for M_{bc} and ΔE variables for $B_s^0 \to \gamma\gamma$ analysis. The points with error bars represent the data, the solid black curve represents the total fit function and the red dashed (blue dashed) curve represents the signal (continuum background) contribution.*

Variable		Function	Parameter	Value	Comment
M_{bc}	Signal ($B_s^{0*}\bar{B}_s^{0*}$)	(CBall + Gaussian) (having common mean)	Mean (μ)	5416.94 MeV/c^2	Fixed(Corr. Value)
			Sigma1 (σ_1)	6.47 MeV/c^2	Fixed(Corr. Value)
			n	7.17	Fixed(MC Value)
			alpha (α)	1.01	Fixed(MC Value)
			Sigma2 (σ_2)	3.82 MeV/c^2	Fixed(MC Value)
			Fraction (f)	0.52	Fixed(MC Value)
	Signal ($B_s^{0*}\bar{B}_s^{0}$)	(CBall + Gaussian) (having common mean)	Mean (μ)	5389.92 MeV/c^2	Fixed(MC Value)
			Sigma1 (σ_1)	12.46 MeV/c^2	Fixed(MC Value)
			n	5.11	Fixed(MC Value)
			alpha (α)	1.36	Fixed(MC Value)
			Sigma2 (σ_2)	5.17	Fixed(MC Value)
			Fraction (f)	0.43	Fixed(MC Value)
	Signal ($B_s^{0}\bar{B}_s^{0}$)	Double-Gaussian function	Mean1 (μ_1)	5367.26 MeV/c^2	Fixed(MC Value)
			Sigma1 (σ_1)	6.20 MeV/c^2	Fixed(MC Value)
			Sigma2 (σ_2)	20.80 MeV/c^2	Fixed(MC Value)
			Fraction (f)	0.68	Fixed(MC Value)
	Background	Argus function	Curvature (a_1)	$-13.60^{+4.56}_{-4.50}$	Floated
			Endpoint (a_0)	5434 MeV/c^2	Fixed(MC Value)
ΔE	Signal ($B_s^{0*}\bar{B}_s^{0*}$)	CBall function	Mean (μ)	-84.59 MeV	Fixed(MC Value)
			Sigma (σ)	63.05 MeV	Fixed(Corr. Value)
			n	23.17	Fixed(MC Value)
			alpha (α)	0.50	Fixed(MC Value)
	Signal ($B_s^{0*}\bar{B}_s^{0}$)	CBall function	Mean (μ)	-63.78 MeV	Fixed(MC Value)
			Sigma (σ)	67.30 MeV	Fixed(MC Value)
			n	15.79	Fixed(MC Value)
			alpha (α)	0.52	Fixed(MC Value)
	Signal ($B_s^{0}\bar{B}_s^{0}$)	CBall function	Mean (μ)	-39.90 MeV	Fixed(MC Value)
			Sigma (σ)	65.96 MeV	Fixed(MC Value)
			n	19.07	Fixed(MC Value)
			alpha (α)	0.51	Fixed(MC Value)
	Background	Chebychev polynomial	Coefficient (c_1)	-0.40 ± 0.09	Floated
	Yields		$N_{B_s^{0*}\bar{B}_s^{0*}}$	$-3.28^{+3.23}_{-2.27}$	Floated
			$N_{B_s^{0*}\bar{B}_s^{0}}$	$-5.76^{+4.75}_{-3.73}$	Floated
			$N_{B_s^{0}\bar{B}_s^{0}}$	$11.47^{+7.74}_{-6.74}$	Floated
			$N_{\text{background}}$	$328.57^{+20.40}_{-19.70}$	Floated

TABLE 4.22: *Real data fit results for $B_s^0 \to \gamma\gamma$ analysis.*

4.4 Chapter Summary

In this chapter we have provided a brief introduction to the ML fit procedure. The PDF parameterizations of signal and background for both $B_s^0 \to \phi\gamma$ and $B_s^0 \to \gamma\gamma$ analyses are then presented. We have also discussed various calibration procedures used to take into account data and MC differences. Finally, we have presented the final fit results for both the channels using the unblinded dataset.

Chapter 5

Systematic Uncertainties

This chapter provides a brief introduction of the systematic uncertainties and their impact on the results of the analyses. Systematic errors affect all the data in the same way i.e., systematically [92, 93]. Repeated measurements share the same systematic effect, and are therefore correlated to each other. Thus, these errors cannot be reduced by performing repeated measurements. Typical sources of systematics in an experiment include improper calibration of measuring instruments, poor knowledge of experimental set up, acceptance and sensitivity of detector components, uncertainties in theoretical and experimental inputs used in the experiment, etc.

The systematic uncertainties can be classified into two types: additive and multiplicative. The multiplicative uncertainties donot affect the signal yield and signal significance of the decay channel but affects its BF. For both the modes, these uncertainties arise due to the uncertainty in signal reconstruction efficiency, on the number of B_s mesons and in the fraction $f_{B_s^{0*}\bar{B}_s^{0*}}$. For $B_s^0 \to \phi\gamma$, the uncertainty due to $\phi \to K^+K^-$ branching fraction also adds to the multiplicative systematics. The additive uncertainties reduce the signal significance of the observed peak and changes the BF of the decay. The additive systematics arise due to the fit procedure, which includes the uncertainty due to PDF parametrization and fit bias, respectively. All the sources of systematic uncertainties that may affect the decay modes studied in this thesis, are listed and discussed in details in this chapter.

5.1 Uncertainty on the Signal Reconstruction Efficiency

The uncertainty due to signal reconstruction efficiency ($\epsilon_{\rm syst.}$) is multiplicative in nature. It is computed as the quadratic sum of the systematic uncertainties in the photon reconstruction, kaon identification, tracking efficiency, $\mathcal{C}_{\rm NB}$ cut and the MC statistics. These uncertainties are described in details in the following subsections:

5.1.1 Uncertainty on the Photon Reconstruction Efficiency

The uncertainty on the photon reconstruction efficiency is computed to be 2.2% per photon by comparing the detection efficiency of real data and MC samples of radiative Bhabha events [103].

5.1.2 Uncertainty on the Tracking Efficiency

The uncertainty on the tracking efficiency was evaluated using partially reconstructed D^* decays. Its value is estimated to be (-0.13 ± 0.30 ± 0.10)% for any charged track of momentum > 200 MeV/c. Since, the value is much smaller than the statistical uncertainty associated with it, therefore, the total systematic uncertainty is taken as the quadratic sum of the actual value and its uncertainties. Thus, the recommended systematic uncertainty is 0.35% per track (of momentum > 200 MeV/c) [104]. This uncertainty will contribute to $B_s^0 \to \phi\gamma$ case only.

5.1.3 Uncertainty on the Kaon Identification Efficiency (K/π Systematics)

Particle identification (PID) performance depends on the laboratory momentum ($\rm p = |\overrightarrow{p}|$) and polar angle ($\theta$). The uncertainty on the kaon identification efficiency has been studied using the PID table provided by Belle PID joint group. In that table, the ratio of PID efficiency in data and MC (i.e., the relative PID efficiency between data and MC) are provided as a function of 'p' and 'cos(θ)'. After incorporating the PID table in our reconstruction code, we have obtained the output as shown in Figure 5.1.

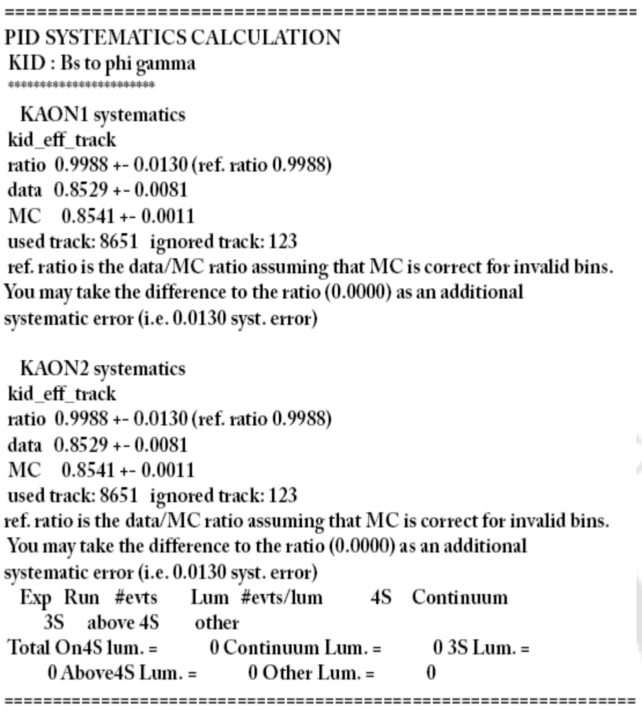

```
=================================================================
PID SYSTEMATICS CALCULATION
 KID : Bs to phi gamma
 ***********************
   KAON1 systematics
 kid_eff_track
 ratio  0.9988 +- 0.0130 (ref. ratio 0.9988)
 data   0.8529 +- 0.0081
 MC     0.8541 +- 0.0011
 used track: 8651   ignored track: 123
 ref. ratio is the data/MC ratio assuming that MC is correct for invalid bins.
You may take the difference to the ratio (0.0000) as an additional
systematic error (i.e. 0.0130 syst. error)

   KAON2 systematics
 kid_eff_track
 ratio  0.9988 +- 0.0130 (ref. ratio 0.9988)
 data   0.8529 +- 0.0081
 MC     0.8541 +- 0.0011
 used track: 8651   ignored track: 123
ref. ratio is the data/MC ratio assuming that MC is correct for invalid bins.
 You may take the difference to the ratio (0.0000) as an additional
systematic error (i.e. 0.0130 syst. error)
   Exp  Run  #evts      Lum  #evts/lum        4S   Continuum
        3S    above 4S       other
 Total On4S lum. =          0 Continuum Lum. =        0 3S Lum. =
       0 Above4S Lum. =         0 Other Lum. =        0
=================================================================
```

FIGURE 5.1: *Output of the PID systematics calculation for $B_s^0 \to \phi\gamma$ analysis.*

The relative PID efficiency or the PID correction factor for each kaon is 0.9988 ± 0.0130. Since the correction factor $(1 - 0.9988) \times 100\% = 0.12\%$ is very small, we assign a systematic uncertainty of 1.3% per kaon track in this analysis. Therefore, for the two correlated kaon tracks in the ϕ reconstruction, we assign a systematic uncertainty of 2.6%.

5.1.4 Uncertainty due to $\mathcal{C}_{\rm NB}$ Cut

The uncertainty due to $\mathcal{C}_{\rm NB}$ cut is obtained using the control sample $B^0 \to K^{0*}\gamma$. To estimate this uncertainty, we calculate the relative signal selection efficiency (R) and hence the efficiency discrepancy between MC and data, when a selection criteria $\mathcal{C}_{\rm NB} > \mathcal{C}_{\rm NB_{cut}}$ is applied. The relative efficiency shown in Table 5.1 is calculated as:

$R = \dfrac{\mathcal{E}_{\rm data}}{\mathcal{E}_{\rm MC}}$ where,

$$\mathcal{E}_{\rm data} = \frac{N_{\rm data}(\text{with } \mathcal{C}_{\rm NB} > \mathcal{C}_{\rm NB_{cut}})}{N_{\rm data}(\text{without } \mathcal{C}_{\rm NB_{cut}})} \text{ and } \mathcal{E}_{\rm MC} = \frac{N_{\rm MC}(\text{with } \mathcal{C}_{\rm NB} > \mathcal{C}_{\rm NB_{cut}})}{N_{\rm MC}(\text{without } \mathcal{C}_{\rm NB_{cut}})}$$

are the efficiencies of the NeuroBayes classifier for real data and signal MC, respectively, after applying $\mathcal{C}_{\rm NB} > \mathcal{C}_{\rm NB_{cut}}$.

Channel	**Data/MC**	**Requirement**	**Yield**	$\mathcal{E}$	$\boldsymbol{R}$
$\boldsymbol{B_s^0 \to \phi\gamma}$	Data	No Cut	4741 ± 146	0.9597 ± 0.0387	1.026 ± 0.040
		$\mathcal{C}_{\rm NB}$ > -0.6	4551 ± 107		
	MC	No Cut	164155 ± 405	0.9356 ± 0.0035	
		$\mathcal{C}_{\rm NB}$ > -0.6	153580 ± 392		
$\boldsymbol{B_s^0 \to \gamma\gamma}$	Data	No Cut	4741 ± 146	0.4921 ± 0.0393	1.035 ± 0.080
		$\mathcal{C}_{\rm NB}$ > 0.77	2333 ± 57		
	MC	No Cut	164155 ± 405	0.4756 ± 0.0043	
		$\mathcal{C}_{\rm NB}$ > 0.77	78078 ± 279		

TABLE 5.1: *Systematic uncertainty due to* $\mathcal{C}_{\rm NB}$ *cut.*

The relative efficiency for $B_s^0 \to \phi\gamma$ is obtained after applying $\mathcal{C}_{\rm NB} >$ -0.6 to the data and MC samples for the decay $B^0 \to K^{0*}\gamma$, since we have applied this selection criteria for the $B_s^0 \to \phi\gamma$ mode. For $B_s^0 \to \gamma\gamma$ case, a selection criteria of $\mathcal{C}_{\rm NB} > 0.77$ is used. For $B_s^0 \to \phi\gamma$, an efficiency discrepancy of 2.6% is observed between data and MC with an error of 4.0%. We thus assign a systematic uncertainty of 4.8% to the $B_s^0 \to \phi\gamma$ channel, by adding them in quadrature. For $B_s^0 \to \gamma\gamma$ mode, a systematic uncertainty of 8.7% is assigned by adding the data-MC discrepancy of 3.5% with the error (8.0%).

5.1.5 Uncertainty due to MC Statistics

The statistical error in signal efficiency contributes to the systematic uncertainty. Since we calculate the final results based on the $(B_s^0 \to \phi\gamma)_{B_s^{0*}\bar{B}_s^{0*}}$ and $(B_s^0 \to \gamma\gamma)_{B_s^{0*}\bar{B}_s^{0*}}$ signal yields, the uncertainty due to MC statistics includes the uncertainty due to these signals only. The uncertainty due to MC statistics is computed as:

$$\Delta\epsilon = \sqrt{\frac{\epsilon \times (1-\epsilon)}{N}}$$

where, N is the total number of signal MC events. We have generated 100,000 events each for $(B_s^0 \to \phi\gamma)_{B_s^{0*}\bar{B}_s^{0*}}$ and $(B_s^0 \to \gamma\gamma)_{B_s^{0*}\bar{B}_s^{0*}}$ signals. The signal efficiencies $(\epsilon \pm \Delta\epsilon)$ for $(B_s^0 \to \phi\gamma)_{B_s^{0*}\bar{B}_s^{0*}}$ and $(B_s^0 \to \gamma\gamma)_{B_s^{0*}\bar{B}_s^{0*}}$ signals are computed to be (36.1 ± 0.2)% and (14.1 ± 0.1)%, as discussed in section 3.5. Thus, the uncertainty due to MC statistics $\left(\frac{\Delta\epsilon}{\epsilon}\right)$ is computed to be 0.6% for $B_s^0 \to \phi\gamma$ and 0.8% for $B_s^0 \to \gamma\gamma$.

5.2 Uncertainty in $\phi \to K^+K^-$ Branching Fraction

The BF of $\phi \to K^+K^-$ is (0.489 ± 0.005). Thus a multiplicative systematic uncertainty of 1.0% is assigned for the $B_s^0 \to \phi\gamma$ channel.

5.3 Uncertainty on the Number of B_s^0 Mesons

The total number of B_s^0 mesons is evaluated as $N(B_s^0) = 2 \times L_{\rm int}^{\Upsilon(5S)} \times \sigma_{b\bar{b}}^{\Upsilon(5S)} \times f_s$ where, $L_{\rm int}^{\Upsilon(5S)}$ and $\sigma_{b\bar{b}}^{\Upsilon(5S)}$ are the integrated luminosity and $b\bar{b}$ production cross-section at $\Upsilon(5{\rm S})$ resonance and f_s is the fraction of $b\bar{b}$ events that hadronize to $B_s^{(*)}\bar{B}_s^{(*)}$ events. Thus the systematic uncertainty on the number of B_s^0 is the quadratic sum of the uncertainties in $L_{\rm int}^{\Upsilon(5S)}$, $\sigma_{b\bar{b}}^{\Upsilon(5S)}$ and f_s. These systematic uncertainties are listed in Table 5.2. This uncertainty is again multiplicative in nature.

5.4 Uncertainty in the Fraction $f_{B_s^{0*}\bar{B}_s^{0*}}$

The value of fraction $f_{B_s^{0*}\bar{B}_s^{0*}}$ is $(87.0 \pm 1.7)\%$. Thus, a multiplicative systematic uncertainty of 2.0% is assigned due to $f_{B_s^{0*}\bar{B}_s^{0*}}$.

5.5 Uncertainty due to the Fit Procedure

Uncertainty due to the fit procedure affects the signal yield. It includes the uncertainty due to PDF parametrization and fit bias, and is estimated using the quadratic sum of these uncertainties. This uncertainty is additive in nature. The uncertainty due to PDF parametrization and fit bias is described in details in the following subsections:

5.5.1 Uncertainty due to PDF Parametrization

The uncertainty due to PDF parametrization is estimated by varying each fixed parameter of the fit PDF by $\pm 1\sigma$ and estimating the variation in $(B_s^0 \to \phi\gamma)_{B_s^{0*}\bar{B}_s^{0*}}$ and $(B_s^0 \to \gamma\gamma)_{B_s^{0*}\bar{B}_s^{0*}}$ signal yields and then adding them in quadrature. The total PDF parametrization uncertainty is computed to be $^{+1.5}_{-1.6}$ events for $B_s^0 \to \phi\gamma$ and $^{+0.2}_{-0.3}$ events for $B_s^0 \to \gamma\gamma$. The calibration uncertainties are also included in the calculation. For those parameters where we have made the corrections, if the corrected value is $\mathbb{C} \pm \mathrm{d}\mathbb{C}$, we have varied the parameters by $\pm\mathrm{d}\mathbb{C}$ amount in the fitter and have checked the yield. The uncertainty '$\mathrm{d}\mathbb{C}$' includes the error in the parameter as well as in the correction factor.

5.5.2 Fit Bias

From our fit bias studies for $B_s^0 \to \phi\gamma$ and $B_s^0 \to \gamma\gamma$, documented in sections 4.2.4 and 4.3.4, we have obtained an average fit bias of ± 0.01 events for $B_s^0 \to \phi\gamma$ and ± 0.1 events for $B_s^0 \to \gamma\gamma$ for the expected signal, which we have assigned as the systematic uncertainty due to fit bias.

5.6 Final Systematic Uncertainties

Tables 5.2 and 5.3 summarizes all the multiplicative and additive systematics and their values, that affect these analyses. The total systematic uncertainty for each mode is the quadratic sum of all the uncertainties corresponding to that mode.

Multiplicative systematic uncertainties (%)		
Source	$\boldsymbol{B_s^0 \to \phi\gamma}$	$\boldsymbol{B_s^0 \to \gamma\gamma}$
Photon Identification	2.2	2 × 2.2
Kaon Identification	2.6	-
Tracking	2 × 0.35	-
$\mathcal{C}_{\mathrm{NB}}$ cut	4.8	8.7
MC statistics	0.6	0.8
Total ($\boldsymbol{\epsilon}$**(syst.)**)	**6.0**	**9.8**
$\mathcal{B}(\phi \to K^+K^-)$	**1.0**	-
L_{int}	1.3	
$\sigma_{b\bar{b}}^{\Upsilon(5S)}$	4.7	
f_s	17.4	
Total ($\boldsymbol{N(B_s^0)}$**(syst.)**)	**18.1**	
$\boldsymbol{f_{B_s^{0*}\bar{B}_s^{0*}}}$	**2.0**	
Total(quadratic sum)	**19.2**	**20.7**

TABLE 5.2: *Summary of multiplicative systematic uncertainties.*

Additive systematic uncertainties (events)		
Source	$B_s^0 \to \phi\gamma$	$B_s^0 \to \gamma\gamma$
PDF parametrization	$^{+1.5}_{-1.6}$	$^{+0.2}_{-0.3}$
Fit bias	± 0.01	± 0.1
Total(quadratic sum)	$^{\mathbf{+1.5}}_{\mathbf{-1.6}}$	$^{\mathbf{+0.2}}_{\mathbf{-0.3}}$

Table 5.3: *Summary of additive systematic uncertainties.*

5.7 Chapter Summary

In this chapter we have summarized all possible sources of multiplicative and additive systematic uncertainties for both the modes. The values of all the systematic uncertainties are listed and the total uncertainties are computed for both the modes.

Chapter 6

Results and Conclusions

This chapter presents the final results for both $B_s^0 \to \phi\gamma$ and $B_s^0 \to \gamma\gamma$ analyses. The estimation of signal significance, branching fraction (BF) calculation for $B_s^0 \to \phi\gamma$ and the estimation of Bayesian upper limit (UL) at 90% confidence level (CL) for $B_s^0 \to \gamma\gamma$ analysis are explained in details. Finally, we conclude with a brief discussion on the possible implications of the results of these analyses and the possibility of observing the decay $B_s^0 \to \gamma\gamma$ at future B-physics experiments such as Belle II.

6.1 $B_s^0 \to \phi\gamma$ Results

In this section, we briefly summarize the $B_s^0 \to \phi\gamma$ results.

6.1.1 Signal Efficiency

We had generated 100,000 signal MC events for $(B_s^0 \to \phi\gamma)_{B_s^{0*}\bar{B}_s^{0*}}$. After applying all the selection criteria, we are left with 36,125 signal MC events, which we use for PDF parametrization. Thus, the signal efficiency for $(B_s^0 \to \phi\gamma)_{B_s^{0*}\bar{B}_s^{0*}}$ signal $(\epsilon \pm \Delta\epsilon)_{B_s^{0*}\bar{B}_s^{0*}}$, is computed to be (36.1 ± 0.2)% as explained in section 3.5.

6.1.2 Signal Significance

As discussed in section 4.2, we have performed a 4D unbinned extended maximum likelihood fit to extract the signal yield for the $B_s^0 \to \phi\gamma$ channel. The significance for the signal yield is calculated by assuming a null or background only hypothesis [92, 93]. The signal significance is computed as $S = \text{sign}(N_{\text{signal}}) * \sqrt{-2 * \ln(\mathcal{L}_0/\mathcal{L}_{\text{max}})}$, where $\mathcal{L}_0$ is the likelihood value when the $(B_s^0 \to \phi\gamma)_{B_s^{0*}\bar{B}_s^{0*}}$ signal yield is constrained to 0 and $\mathcal{L}_{\text{max}}$ is the maximum likelihood value of the likelihood fit. Here, N_{signal} (or $N_{B_s^{0*}\bar{B}_s^{0*}}$) is the yield of $(B_s^0 \to \phi\gamma)_{B_s^{0*}\bar{B}_s^{0*}}$ signal obtained from the likelihood fit. Additive systematic uncertainties are incorporated by convolving the plain likelihood curve with a Gaussian of width equal to the total additive systematics i.e., $\sigma = \sigma_{\text{additive syst}}$. The convolution of the two functions f and g over an infinite range is given by:

$$h(x) = f(x) \star g(x) = \int_{-\infty}^{+\infty} f(x-y)g(y)dy$$

The signal significance with (without) systematics is computed to be 10.6 (11.7). The profile and plain likelihood plots are shown in Figure 6.1.

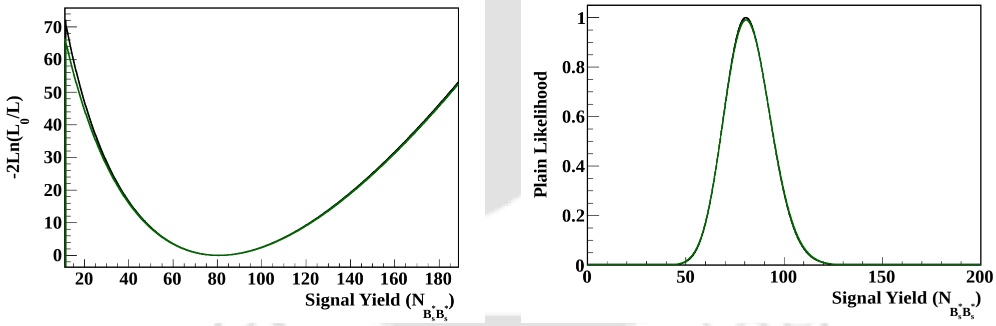

FIGURE 6.1: *Profile and plain likelihood curves for $B_s^0 \to \phi\gamma$ analysis Black (green) curves denote the likelihood curves before (after) convolution.*

6.1.3 Estimation of Branching Fraction

The BF for the decay $B_s^0 \to \phi\gamma$ is computed as:

$$\mathcal{B}(B_s^0 \to \phi\gamma) = \frac{N_{B_s^{0*}\bar{B}_s^{0*}}}{\mathcal{B}(\phi \to K^+K^-) \times \epsilon_{B_s^{0*}\bar{B}_s^{0*}} \times N(B_s^0) \times f_{B_s^{0*}\bar{B}_s^{0*}}}$$

where, $N_{B_s^{0*}\bar{B}_s^{0*}}$ is the signal yield of $(B_s^0 \to \phi\gamma)_{B_s^{0*}\bar{B}_s^{0*}}$ signal; $\epsilon_{B_s^{0*}\bar{B}_s^{0*}}$ is the signal selection efficiency of $(B_s^0 \to \phi\gamma)_{B_s^{0*}\bar{B}_s^{0*}}$ signal; $N(B_s^0)$ is the number of B_s^0 mesons in the 121.4 fb^{-1} Υ(5S) data evaluated as $N(B_s^0) = 2 * L_{\text{int}} * \sigma_{b\bar{b}}^{\Upsilon(5S)} * f_s$ and $f_{B_s^{0*}\bar{B}_s^{0*}}$ is the fraction of $B_s^{0*}\bar{B}_s^{0*}$ among $B_s^{(*)}\bar{B}_s^{(*)}$ events. Here, L_{int} is the integrated luminosity at Υ(5S) energy and $\sigma_{b\bar{b}}^{\Upsilon(5S)}$ is the production cross-section of $b\bar{b}$ at Υ(5S) energy.

The statistical uncertainty on the BF is computed as:

$$\Delta\mathcal{B}_{\text{stat.}} = \left(\frac{\Delta N_{B_s^{0*}\bar{B}_s^{0*}}}{N_{B_s^{0*}\bar{B}_s^{0*}}}\right) \times \mathcal{B}$$

and the systematic uncertainty $\Delta\mathcal{B}_{\text{syst.}}$ is the quadratic sum of multiplicative and additive systematics.

Thus, the BF for $B_s^0 \to \phi\gamma$ is computed to be $(3.7^{+0.6}_{-0.5} \pm 0.7) \times 10^{-5}$ where, the first uncertainty is statistical and the second uncertainty is systematic. The $B_s^0 \to \phi\gamma$ results along with their uncertainties are summarized in Table 6.1.

Parameter	**Value**
L_{int}	$(121.4 \pm 1.6)\ fb^{-1}$
$N_{B_s^{0*}\bar{B}_s^{0*}}$	80^{+12}_{-11}
$\mathcal{B}(\phi \to K^+K^-)$	0.489 ± 0.005
$\epsilon_{B_s^{0*}\bar{B}_s^{0*}}$	$(36.1 \pm 0.2)\%$
$f_{B_s^{0*}\bar{B}_s^{0*}}$	$(87.0 \pm 1.7)\%$
$\sigma_{b\bar{b}}^{\Upsilon(5S)}$	$(0.340 \pm 0.016)\ nb$
f_s	$(17.2 \pm 3.0)\%$
$N(B_s^0)$	$(14.2 \pm 2.6) \times 10^6$
$\mathcal{B}(B_s^0 \to \phi\gamma)$	$(3.7^{+0.6}_{-0.5} \pm 0.7) \times 10^{-5}$

TABLE 6.1: $B_s^0 \to \phi\gamma$ *results*

6.2 $B_s^0 \to \gamma\gamma$ Results

In this section, we summarize the $B_s^0 \to \gamma\gamma$ results.

6.2.1 Signal Efficiency

We had generated 100,000 signal MC events for $(B_s^0 \to \gamma\gamma)_{B_s^{0*}\bar{B}_s^{0*}}$. After applying all the selection criteria, we are left with 14,136 signal MC events, which we use for PDF parametrization. Thus, the signal efficiency for $(B_s^0 \to \gamma\gamma)_{B_s^{0*}\bar{B}_s^{0*}}$ signal $(\epsilon \pm \Delta\epsilon)_{B_s^{0*}\bar{B}_s^{0*}}$, is computed to be $(14.1 \pm 0.1)\%$ as explained in details in section 3.5.

6.2.2 Signal Significance

For the $B_s^0 \to \gamma\gamma$ channel, we have performed a 2D unbinned extended maximum likelihood fit to extract the signal yield as described in section 4.3. Similar to the $B_s^0 \to \phi\gamma$ case, we estimate the signal significance for $B_s^0 \to \gamma\gamma$ using the null hypothesis. The signal significance for $B_s^0 \to \gamma\gamma$ is computed to be -1.0 for both with and without systematics case (more precisely, -1.008 and -1.013 with and without systematics). The profile and plain likelihood plots are shown in Figure 6.2.

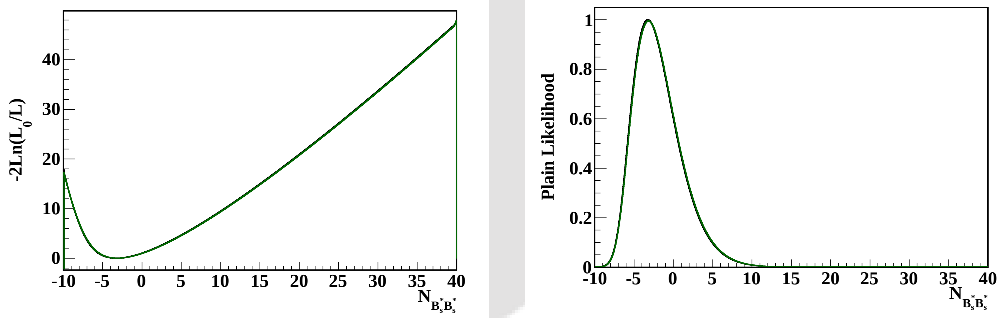

FIGURE 6.2: *Profile and plain likelihood curves for $B_s^0 \to \gamma\gamma$ analysis Black (green) curves denote the likelihood curves before (after) convolution.*

6.2.3 Upper Limit

In the absence of any significant signal yield for the $B_s^0 \to \gamma\gamma$ decay, we estimate the 90% CL upper limit on the BF of $B_s^0 \to \gamma\gamma$ using the Bayesian technique [93]. To do this, we incorporate the additive systematic uncertainties by convolving the plain likelihood curve with a Gaussian of width equal to total additive systematic uncertainties. We then obtain the modified likelihood curve and integrate that curve from 0 till we obtain 90% of the total integral under the likelihood curve (above zero) to obtain the 90% CL upper limit of N_{signal} and hence of the BF. The 90% CL upper limit of N_{signal} is estimated to be 5.5 (5.4) with (without) systematics. The 90% CL upper limit for $B_s^0 \to \gamma\gamma$ BF can be computed as:

$$\text{90\% CL upper limit of } \mathcal{B}(B_s^0 \to \gamma\gamma) \;=\; \frac{\text{90\% CL upper limit of } N_{B_s^{0*}\bar{B}_s^{0*}}}{\epsilon_{B_s^{0*}\bar{B}_s^{0*}} \times N(B_s^0) \times f_{B_s^{0*}\bar{B}_s^{0*}}}$$

where, (90% CL upper limit of $N_{B_s^{0*}\bar{B}_s^{0*}}$) is the 90% CL upper limit of the signal yield of $(B_s^0 \to \gamma\gamma)_{B_s^{0*}\bar{B}_s^{0*}}$ signal and $\epsilon_{B_s^{0*}\bar{B}_s^{0*}}$ is the signal selection efficiency of $(B_s^0 \to \gamma\gamma)_{B_s^{0*}\bar{B}_s^{0*}}$ signal. Thus, the 90% CL upper limit of $B_s^0 \to \gamma\gamma$ BF is estimated to be 3.1×10^{-6} for both with and without systematics case. The $B_s^0 \to \gamma\gamma$ results are presented in Table 6.2

Parameter	**Value**
L_{int}	$(121.4 \pm 1.6)\ fb^{-1}$
$N_{B_s^{0*}\bar{B}_s^{0*}}$	$-3.3^{+3.2}_{-2.3}$
$\epsilon_{B_s^{0*}\bar{B}_s^{0*}}$	$(14.1 \pm 0.1)\%$
$f_{B_s^{0*}\bar{B}_s^{0*}}$	$(87.0 \pm 1.7)\%$
$\sigma_{b\bar{b}}^{\Upsilon(5S)}$	$(0.340 \pm 0.016)\ nb$
f_s	$(17.2 \pm 3.0)\%$
$N(B_s^0)$	$(14.2 \pm 2.6) \times 10^6$
90% CL UL of $\mathcal{B}(B_s^0 \to \gamma\gamma)$	3.1×10^{-6}

TABLE 6.2: $B_s^0 \to \gamma\gamma$ *results*

6.3 Summary and Conclusions

This thesis describes the measurement of the BF for the decay $B_s^0 \to \phi\gamma$ and search for the decay $B_s^0 \to \gamma\gamma$ at high energy e^+e^- collisions. These analyses are done using 121.4 fb^{-1} of data collected by the Belle detector at Υ(5S) energy. We have made an updated measurement of $B_s^0 \to \phi\gamma$ BF, which is in agreement with the theoretical and current experimental results. Our measurement of $B_s^0 \to \phi\gamma$ BF is more precise than the theoretical expectations. Further improvement in the theoretical calculation is necessary to understand the possible new physics effects in this channel.

No significant signal yield is observed for the $B_s^0 \to \gamma\gamma$ mode. We have set the 90% CL upper limit on its BF to be 3.1×10^{-6}. This limit improves the previously measured value by a factor of about 3 and is the most stringent one till date. Our $B_s^0 \to \gamma\gamma$ result rules out large contributions from RPV SUSY in this channel and could possibly constrain various SUSY parameters in the RPV scenario. This decay will possibly be observed in Belle II with a dedicated run at $\Upsilon(5S)$ resonance.

Appendix A

Decay Files of $B_s^0 \to \phi\gamma$ and $B_s^0 \to \gamma\gamma$ Analyses

This appendix contains the decay files for $B_s^0 \to \phi\gamma$ and $B_s^0 \to \gamma\gamma$ analysis.

A.1 $B_s^0 \to \phi\gamma$ decay file ($B_s^{0*}\bar{B}_s^{0*}$ component)

```
#   DECAY $B_s^0 \to \phi\gamma$


Alias       MyB_s0          B_s0
Alias       MyantiB_s0      antiB_s0
Alias       MyB_s*0         B_s*0
Alias       MyantiB_s*0     anti-B_s*0
Alias       Myphi           phi

Decay       Upsilon(5S)
0.500       MyB_s*0         anti-B_s*0      PHSP;
0.500       B_s*0           Myanti-B_s*0    PHSP;
Enddecay

Decay       MyB_s*0
```

```
1.000      MyB_s0          gamma         VSP_PWAVE;
Enddecay

Decay      MyantiB_s*0
1.000      MyantiB_s0      gamma         VSP_PWAVE;
Enddecay

Decay      My_Bs0
1.000      Myphi           gamma         PHOTOS SVP_HELAMP 1.0 0.0 1.0 0.0
Enddecay

Decay      Myanti-B_s0
1.000      Myphi           gamma         PHOTOS SVP_HELAMP 1.0 0.0 1.0 0.0
Enddecay

Decay      Myphi
1.000      K+              K-            VSS
Enddecay
End
```

A.2 $B_s^0 \to \gamma\gamma$ decay file ($B_s^{0*}\bar{B}_s^{0*}$ component)

```
#   DECAY B_s^0 → γγ

Alias      MyB_s0         B_s0
Alias      MyantiB_s0     antiB_s0
Alias      MyB_s*0         B_s*0
Alias      MyantiB_s*0    anti-B_s*0

Decay      Upsilon(5S)
0.500      MyB_s*0        anti-B_s*0     PHSP;
0.500      B_s*0          Myanti-B_s*0  PHSP;
Enddecay
```

```
Decay     MyB_s*0
1.000     MyB_s0        gamma        VSP_PWAVE;
Enddecay

Decay     MyantiB_s*0
1.000     MyantiB_s0    gamma        VSP_PWAVE;
Enddecay

Decay     My_Bs0
1.000     gamma         gamma        PHSP;
Enddecay

Decay     Myanti-B_s0
1.000     gamma         gamma        PHSP;
Enddecay
End
```

A.3 Υ(5S) decay to $B_s^{0*}\bar{B}_s^0$ and $B_s^0\bar{B}_s^0$

To simulate Υ(5S) decaying to $B_s^{0*}\bar{B}_s^0$ and $B_s^0\bar{B}_s^0$, we have used:

```
Decay     Upsilon(5S)
0.250      MyB_s*0      anti-B_s0      PHSP;
0.250      MyB_s0       anti-B_s*0     PHSP;
0.250      B_s*0        Myanti-B_s0    PHSP;
0.250      B_s0         Myanti-B_s*0   PHSP;
Enddecay

Decay     Upsilon(5S)
0.500      MyB_s0       anti-B_s0      VSS;
0.500      B_s0         Myanti-B_s0    VSS;
Enddecay
```

Appendix B

Details of the Event Classifier

In this appendix, we present the plots of the event shape variables used in the event classifier (NeuroBayes) for $B_s^0 \to \phi\gamma$, $B_s^0 \to \gamma\gamma$ and $B^0 \to K^{0*}\gamma$ analyses as shown in Figure B.1, Figure B.2 and Figure B.3, respectively. The correlation matrices for $B_s^0 \to \gamma\gamma$ and $B^0 \to K^{0*}\gamma$ analyses are presented in Figure B.4 and the NeuroBayes training-validation comparison plots for $B^0 \to K^{0*}\gamma$ analysis are presented in Figure B.5, respectively.

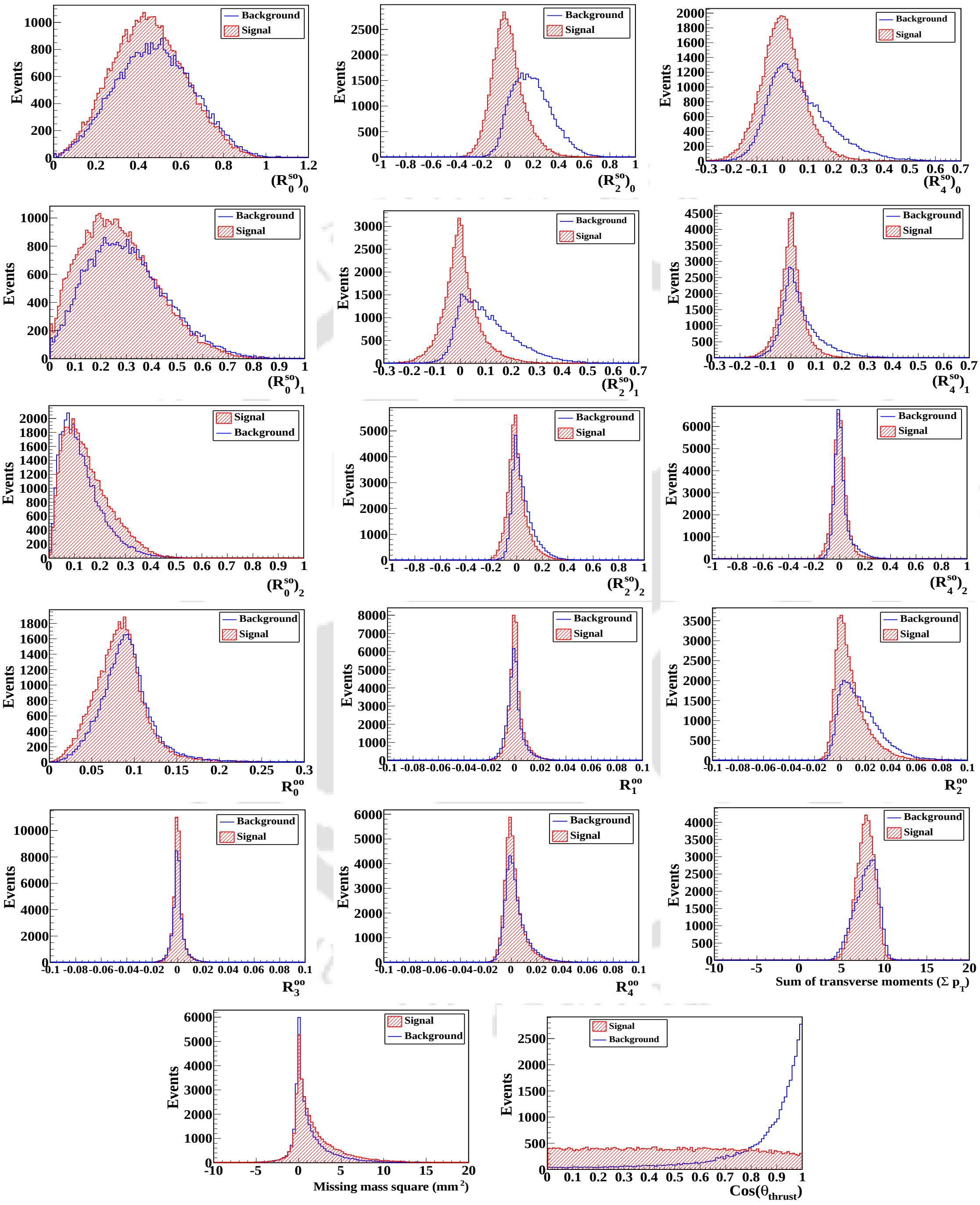

FIGURE B.1: *Continuum suppression variables for $B^0_s \to \phi\gamma$ analysis.*

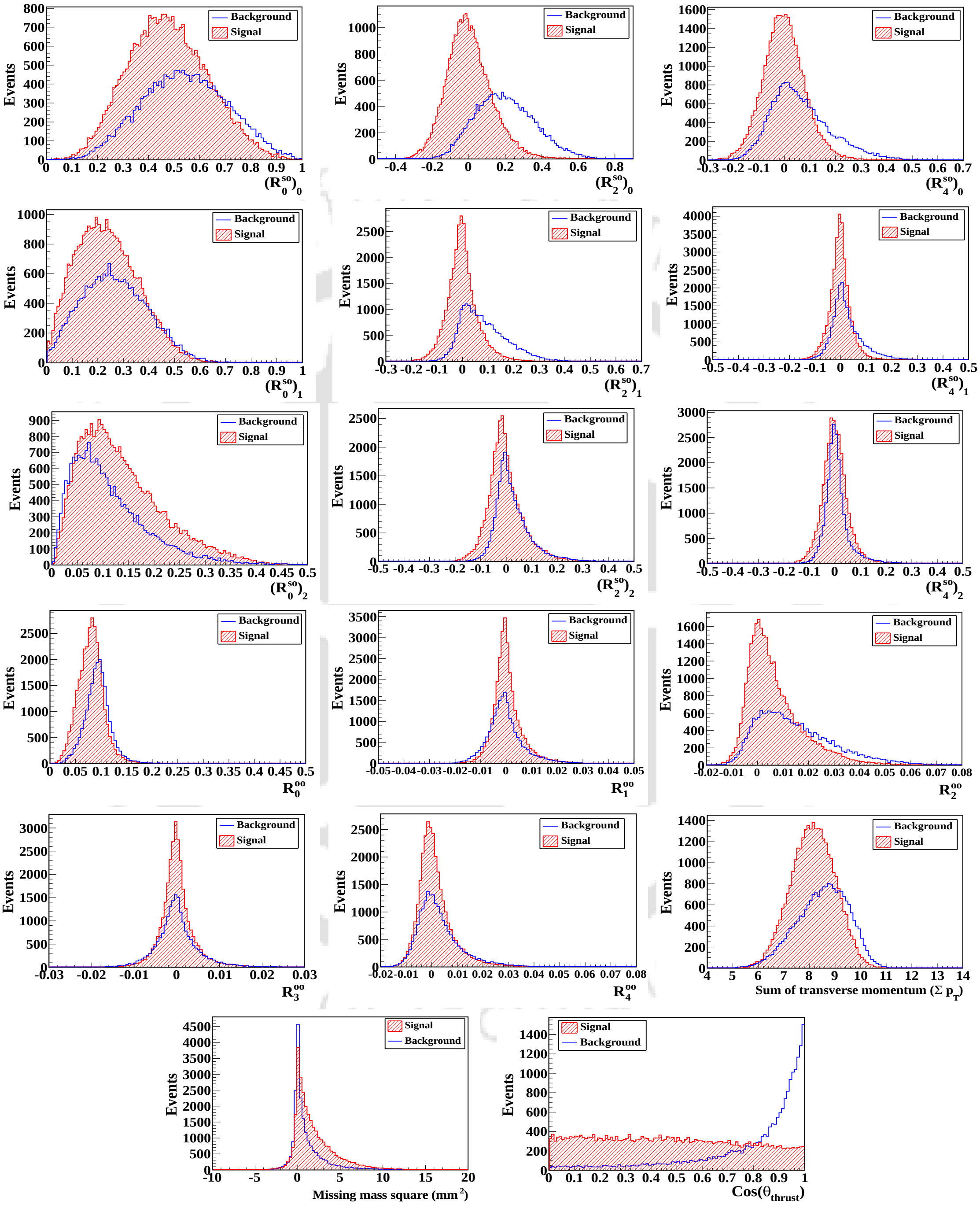

FIGURE B.2: *Continuum suppression variables for* $B_s^0 \to \gamma\gamma$ *analysis.*

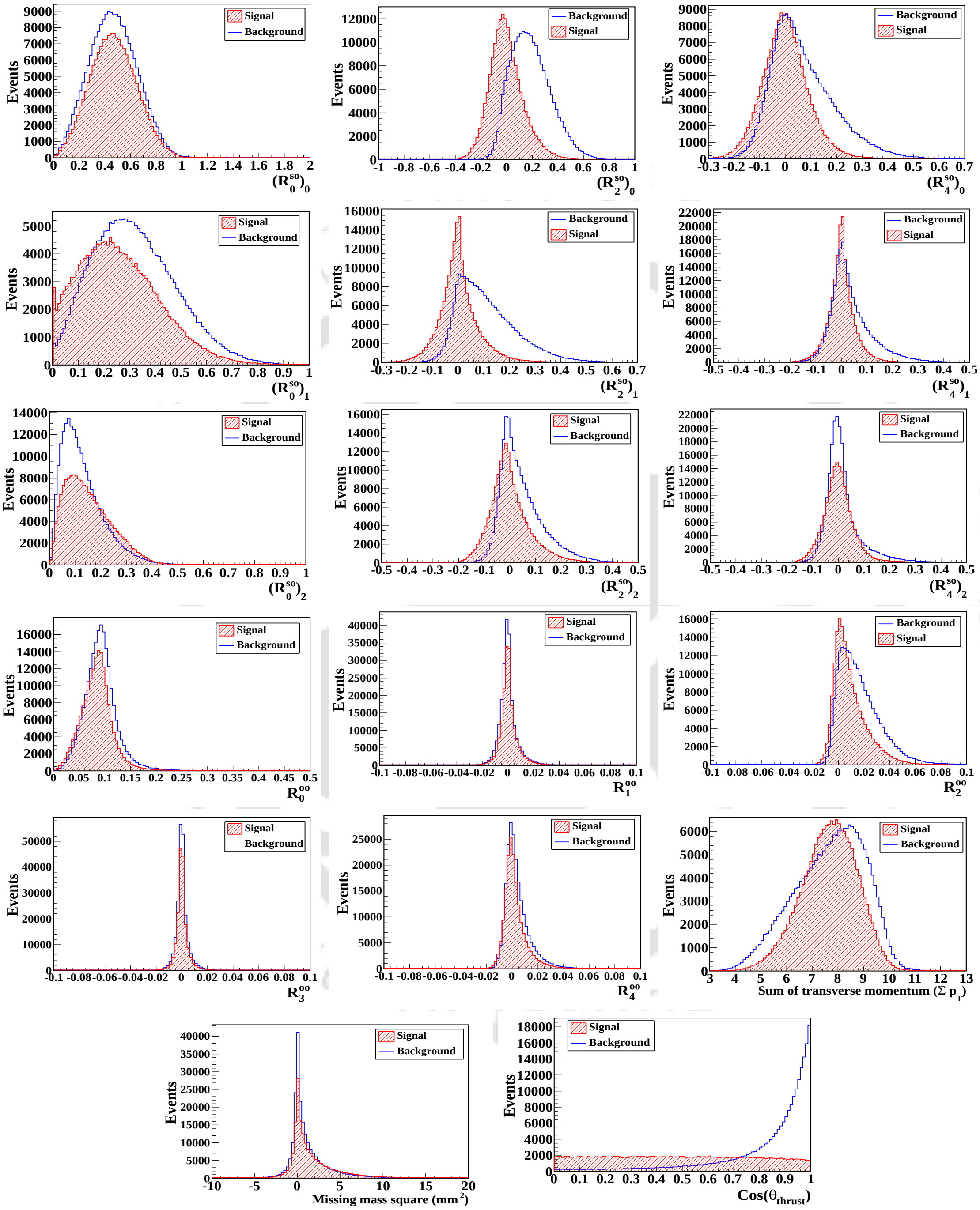

FIGURE B.3: *Continuum suppression variables for* $B^0 \to K^{0*}\gamma$ *analysis.*

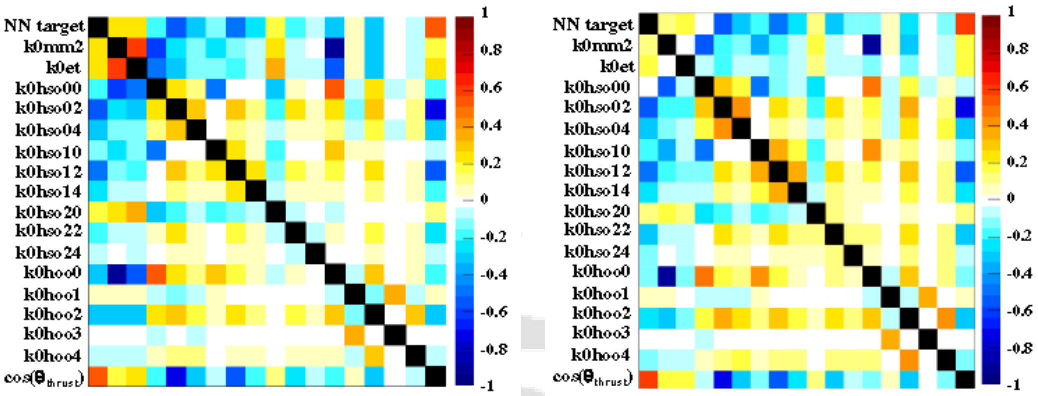

(a) (b)

FIGURE B.4: *Correlation matrices for (a)* $B_s^0 \to \gamma\gamma$ *and (b)* $B^0 \to K^{0*}\gamma$ *analysis.*

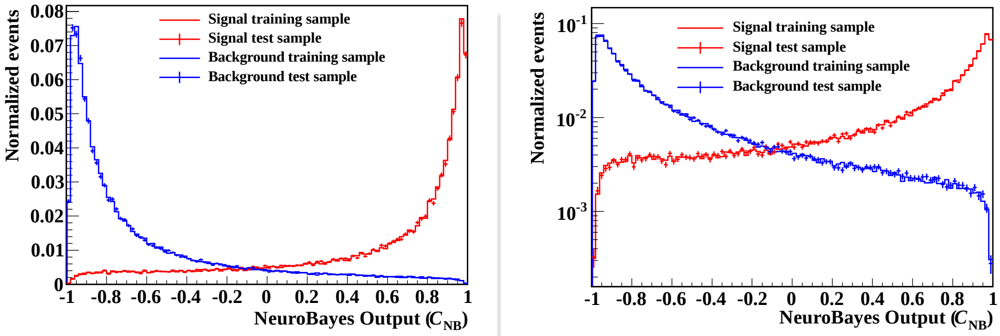

(a) (b)

FIGURE B.5: *NB output for training and validation samples for* $B^0 \to K^{0*}\gamma$ *analysis superimposed in (a) linear and (b) logarithmic vertical scale.*

भारतीय प्रौद्योगिकी संस्थान गुवाहाटी
Indian Institute of Technology Guwahati

Appendix C

Peaking Backgrounds

In this appendix, we present the plots of different fit variables for generic B_s and non-B_s backgrounds for both $B_s^0 \to \phi\gamma$ and $B_s^0 \to \gamma\gamma$ decays. These plots correspond to 6 streams, each stream having the same luminosity as data.

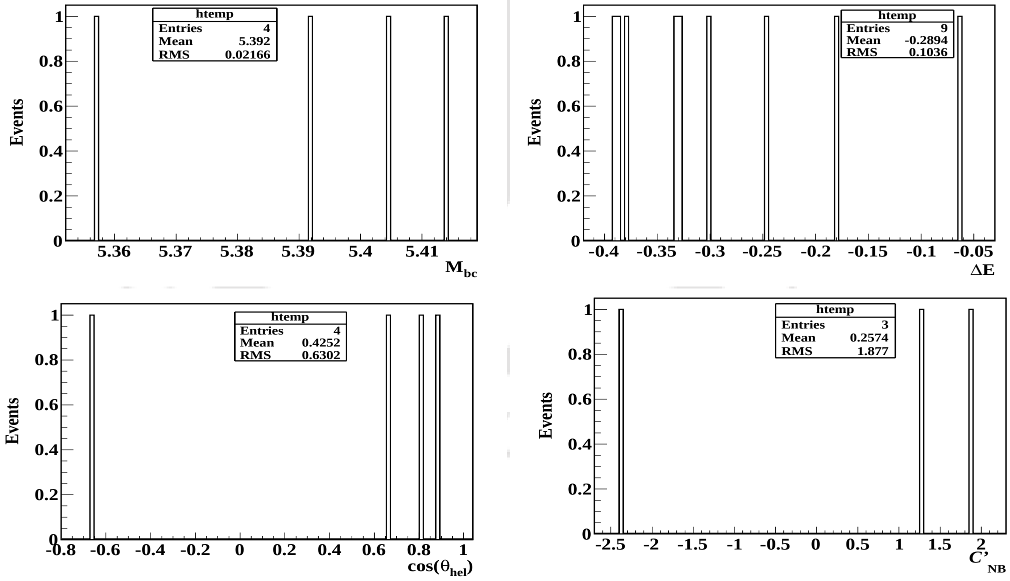

FIGURE C.1: *Generic B_s background plots for each fit variable for $B_s^0 \to \phi\gamma$, after all cuts including $(B_s^0 \to \phi\gamma)_{B_s^{0*}\bar{B}_s^{0*}}$ signal region cuts on other dimensions (6 streams).*

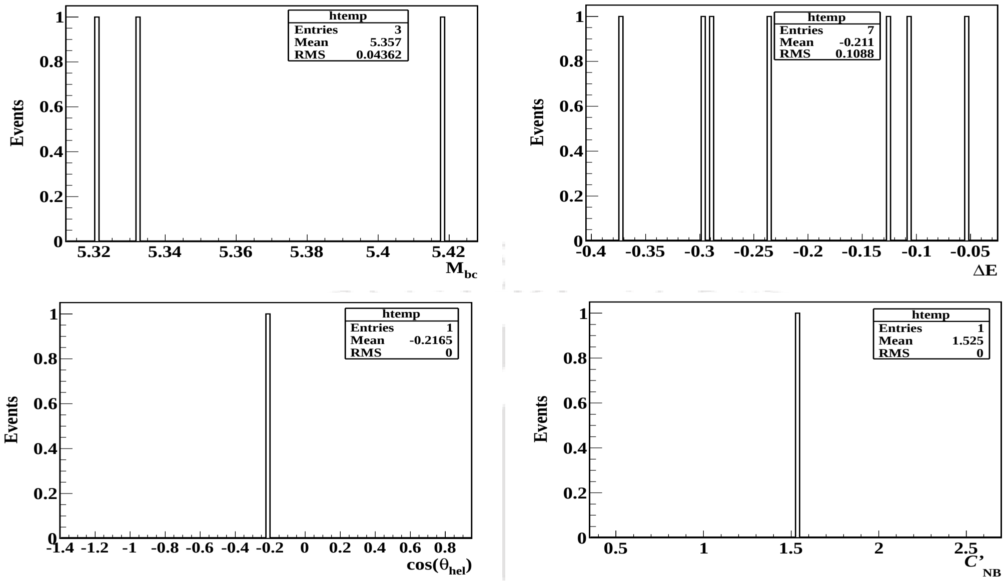

Figure C.2: *Generic non-B_s background plots for each fit variable for $B_s^0 \to \phi\gamma$, after all cuts including $(B_s^0 \to \phi\gamma)_{B_s^{0*}\bar{B}_s^{0*}}$ signal region cuts on other dimensions (6 streams).*

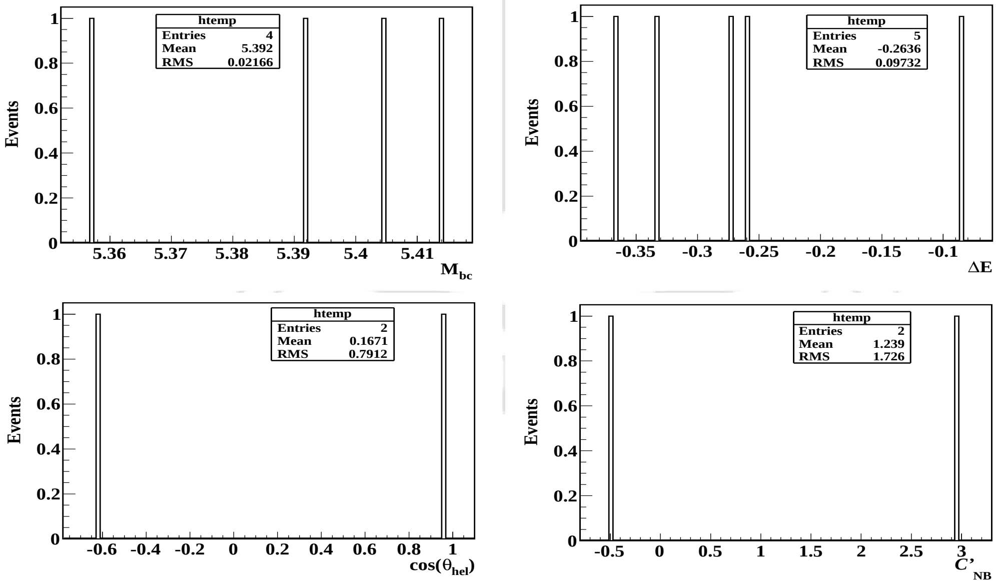

Figure C.3: *Generic B_s background plots for each fit variable for $B_s^0 \to \phi\gamma$, after all cuts including $(B_s^0 \to \phi\gamma)_{B_s^{0*}\bar{B}_s^0}$ signal region cuts on other dimensions (6 streams).*

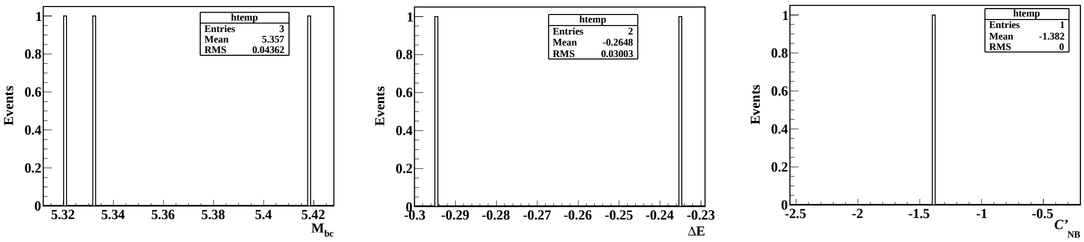

Figure C.4: *Generic non-B_s background plots for each fit variable for $B_s^0 \to \phi\gamma$, after all cuts including $(B_s^0 \to \phi\gamma)_{B_s^{0*}\bar{B}_s^0}$ signal region cuts on other dimensions (6 streams).*

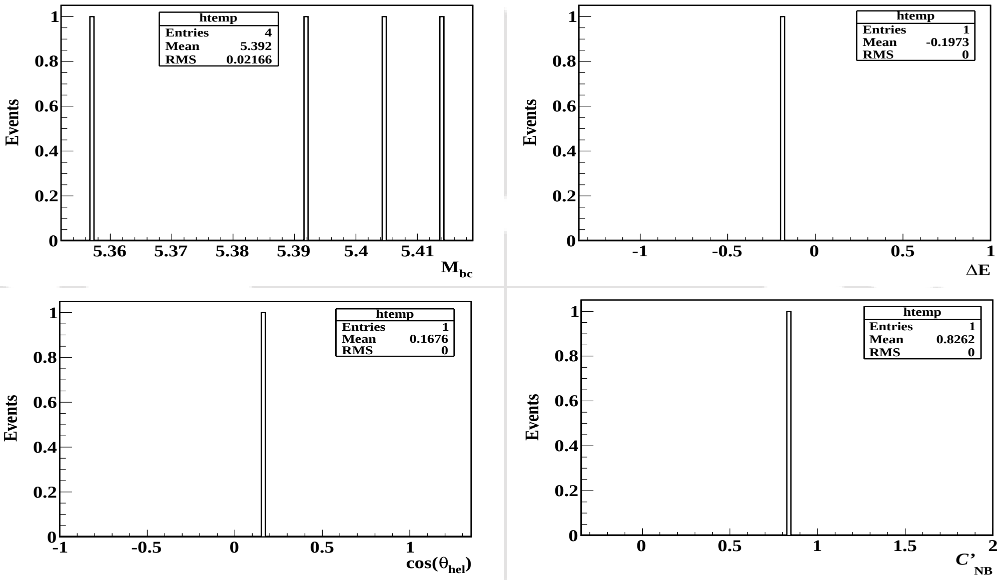

Figure C.5: *Generic B_s background plots for each fit variable for $B_s^0 \to \phi\gamma$, after all cuts including $(B_s^0 \to \phi\gamma)_{B_s^0\bar{B}_s^0}$ signal region cuts on other dimensions (6 streams).*

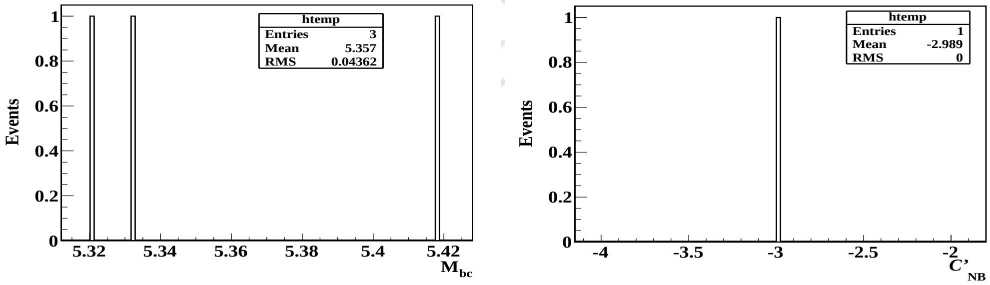

Figure C.6: *Generic non-B_s background plots for each fit variable for $B_s^0 \to \phi\gamma$, after all cuts including $(B_s^0 \to \phi\gamma)_{B_s^0\bar{B}_s^0}$ signal region cuts on other dimensions (6 streams).*

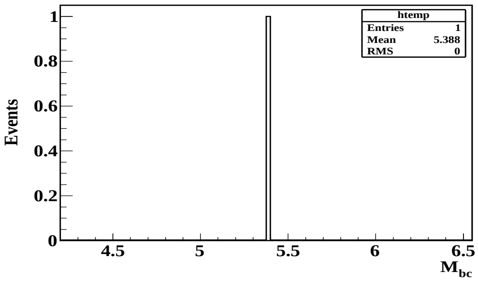

FIGURE C.7: *Generic non-B_s background plots for each fit variable for $B_s^0 \to \gamma\gamma$, after all cuts including $(B_s^0 \to \gamma\gamma)_{B_s^{0*}\bar{B}_s^{0*}}$ signal region cuts on other dimensions (6 streams).*

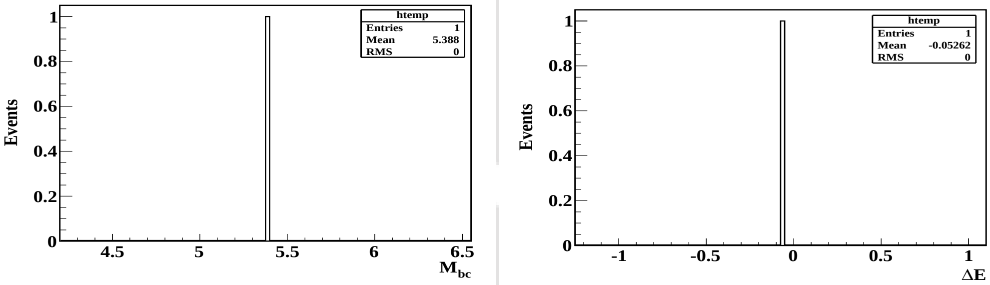

FIGURE C.8: *Generic non-B_s background plots for each fit variable for $B_s^0 \to \gamma\gamma$, after all cuts including $(B_s^0 \to \gamma\gamma)_{B_s^{0*}\bar{B}_s^{0}}$ signal region cuts on other dimensions (6 streams).*

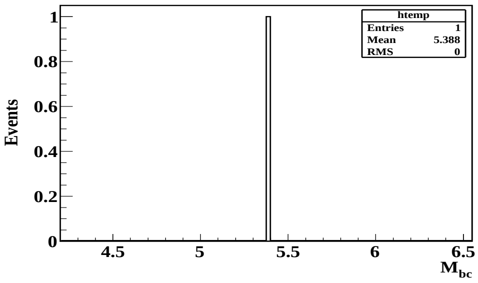

FIGURE C.9: *Generic non-B_s background plots for each fit variable for $B_s^0 \to \gamma\gamma$, after all cuts including $(B_s^0 \to \gamma\gamma)_{B_s^{0}\bar{B}_s^{0}}$ signal region cuts on other dimensions (6 streams).*

Appendix D

Details of Probability Distribution Functions

In this section we present the functional form of some of the functions which we have used to model the signal and background PDFs.

D.1 Crystal Ball Function

The CBall function is a Gaussian with a power law tail that is traditionally used to describe the effect of radiative energy loss in an invariant mass or an energy difference distribution [95, 96]. It is defined as:

$$f(x|\mu,\sigma,\alpha,n) \;=\; N.\begin{cases} \exp\left(\dfrac{-(x\;-\;\mu)^2}{2\,\sigma^2}\right), \text{ for } \dfrac{x-\mu}{\sigma} > -\alpha \\ \left(\dfrac{n}{\alpha}\right)^2 \exp\left(\dfrac{-|\alpha|^2}{2}\right)\left(\dfrac{n}{|\alpha|}\;-\;|\alpha|\;-\;\dfrac{x\;-\;\mu}{\sigma}\right)^{-n}, \text{ for } \dfrac{x-\mu}{\sigma} \leqslant -\alpha \end{cases}$$

where, N is the normalization factor and μ, σ, α and n are the parameters of the CBall function. μ and σ denotes the mean and sigma of the Gaussian part. The n parameter controls the slope of the exponential part and is usually held fixed in a fit. Lower values of n generate a longer tail. The parameter α determines the crossover point from the Gaussian distribution to the power law distribution, in units of the peak width σ. When

α is positive, the tail is below the peak (i.e., in the left) and when it is negative, it is above the peak.

D.2 Argus Function

The Argus function [95, 96, 105] is an empirical function first used by the ARGUS collaboration. It is frequently used in B-physics analysis and mostly used to model the invariant mass or $M_{\rm bc}$ distribution of the combinatorial background. It is defined as:

$$f(x|a_0,a_1) = \frac{1}{N}\, x\sqrt{1-\left(\frac{x}{a_0}\right)^2}\,\exp\left[a_1\left(1-\left(\frac{x}{a_0}\right)^2\right)\right]\Theta(x<a_0)$$

where, Θ is a step function with $\Theta(x < a_0) = 1$ and $\Theta(x > a_0) = 0$. a_0 denotes the threshold of the invariant mass distribution and is usually held fixed in a fit. a_1 denotes the curvature of the Argus distribution.

D.3 Chebychev Polynomial

The Chebyshev polynomials are a sequence of orthogonal polynomials which can be defined recursively as:

$$T_{n+1}(x) = 2xT_n(x) - T_{n-1}(x)$$

The first few Chebychev polynomials are:

$$\begin{aligned}
&T_0(x) = 1.\\
&T_1(x) = x.\\
&T_2(x) = 2x^2 - 1.\\
&T_3(x) = 4x^3 - 3x.\\
&T_4(x) = 8x^4 - 8x^2 + 1.\\
&\vdots
\end{aligned}$$

Any arbitrary polynomial of degree $\mathcal{N}$ can be written in terms of Chebychev polynomial [95, 96] as:

$$f(x|c_i) = \frac{1}{N}\left[T_0(x) + \sum_{i=1}^{\mathcal{N}} c_i T_i(x)\right]$$

where, $T_i(x)$ is a i^{th} order Chebychev polynomial. The parameters c_i's are coefficients of the functions T_i's. Chebychev polynomials are orthogonal in the interval [-1,1]. Due to lower correlations between coefficients in a fit, they have superior stability than normal polynomial functions.


भारतीय प्रौद्योगिकी संस्थान गुवाहाटी
Indian Institute of Technology Guwahati

Appendix E

Acronyms and Abbreviations

ACC	Aerogel Cherenkov Counter
ADC	Analogue-to-Digital Converter
BASF	Belle AnalysiS Framework
BF	Branching Fraction
BFGS	Broyden-Fletcher-Goldfarb-Shanno
BGO	Bismuth Germanium Oxide ($Bi_4Ge_3O_{12}$)
CDC	Central Drift Chamber
CFS	Columbia-Fermilab-Stony Brook
CsI	Cesium Iodide
CKM	Cabibbo-Kobayashi-Maskawa
CL	Confidence Level
CM	Centre of Mass
CP	Charge-Parity
CPV	Charge-Parity Violation
DAQ	Data Acquisition
DSSD	Double sided Silicon-Strip Detectors
DST	Data Summary Tapes
ECL	Electromagnetic Calorimeter
EFC	Extreme Forward calorimeter
EFT	Effective Field Theory
FCNC	Flavor Changing Neutral Current

FM-PMT	Fine-Mesh Photo Multiplier Tubes
FSI	Final State Interactions
GDL	Global Decision Logic
GIM	Glashow-Iliopoulos-Maiani
h.c.	Hermitian conjugate
2HDM	Two Higgs Doublet Model
HER	High Energy Ring
HJM	Heavy Jet Mass
HQE	Heavy Quark Expansion
IP	Interaction Point
KEK	High Energy Accelerator Research Organization
KLM	K_L and Muon detector
KSFW	Kakuno Super Fox-Wolfram
LER	Low Energy Ring
LINAC	LINear ACcelerator
MC	Monte Carlo
MDST	Mini Data Summary Tapes
OPE	Operator Product Expansion
PDF	Probability Distribution Functions
PHSP	(N-body) PHase SPace
PID	Particle IDentity
PMT	Photo Multiplier Tubes
QCD	Quantum ChromoDynamics
QED	Quantum ElectroDynamics
QFT	Quantum Field Theory
RG	Renormalization Group
RI	Refractive Index
RPC	Resistive Plate Counter
RPV	R-Parity Violation model
SM	Standard Model
SUSY	SUper SYmmetry
SVD	Silicon Vertex Detector
SVP_HELAMP	Scalar to Vector and Photon HELicity AMPlitude
Tl	Thallium

TDC	Time-to-Digital Converter
TOF	Time Of Flight
TSC	Trigger Scintillation Counter
UL	Upper Limit
VSS	Vector to Scalar and Scalar
VSP_PWAVE	Vector to Scalar and Photon PWAVE

Publications and Presentations

Publications and Technical Reports

- *Search for $B_s^0 \to \gamma\gamma$ and a measurement of the branching fraction for $B_s^0 \to \phi\gamma$. - D. Dutta, B. Bhuyan et. al.* - arXiv 1411.7771. Accepted for publication in PRD(RC).
- *Search for the decay $B_s^0 \to \gamma\gamma$ and branching fraction measurement for the decay $B_s^0 \to \phi\gamma$. - D. Dutta, B. Bhuyan and K. Trabelsi.* - Belle Note 1250.
- *Co-author of 30+ publications as a member of the Belle Collaboration.*
- *Exclusive $b \to s\gamma$ decays at Belle. - D. Dutta and B. Bhuyan.* - Manuscript under preparation for publication in Journal of Physics: Conference Series (IOP).

Talks at Conferences

The results of this thesis have been presented by me at:

- XXDAE HEP Symposium held at Visva Bharati, Shantiniketan during Jan 13, 2013 - Jan 19, 2013.
- National Conference on Contemporary Issues held at Gauhati University during Feb 12, 2013 - Feb 14, 2013.
- DISCRETE - 2014: Fourth Symposium on Prospects in the Physics of Discrete Symmetries held at Kings College Strand Campus, London during Dec 2, 2014 Dec 6, 2014.

Schools, Workshops and Collaboration Meetings

- VIII SERC School on experimental high energy physics held at VECC Kolkata during June 20, 2011 - July 10, 2011.
- First Belle Analysis Workshop at TIFR, Mumbai during Jan 15, 2012 - Jan 31, 2012.

- Belle Analysis School at KEK, Japan during May 9, 2012 - May 11, 2012.
- Belle Analysis Meeting at KEK, Japan during May 12, 2012 - May 13, 2012.
- Second Belle Analysis Workshop at TIFR, Mumbai during Jan 20, 2013 - Jan 31, 2013.
- Workshop of EWSB and Flavours in the Light of LHC at IIT Guwahati during Feb 20, 2014 - Feb 22, 2014.
- Third Belle Analysis Workshop at IIT Guwahati, during Feb 24, 2014 - Mar 4, 2014.

Apart from these I have presented the status report on my analysis online in various collaboration meetings and bi-weekly $\Upsilon(5S)$ group meetings.

Bibliography

[1] G. L. Kane, *Modern Elementary Particle Physics* (Addison-Wesley, 1987).

[2] F. Halzen and A. D. Martin, *Quark & Leptons: An Introductory Course in Modern Particle Physics* (John Wiley & Sons, 2008).

[3] B. Martin and G. Shaw, *Particle Physics*, vol. 45 (John Wiley & Sons, 2008).

[4] M. Herrero, arXiv: hep-ph/9812242 **3** (1998).

[5] S. Oggero, Ph.D. thesis, Amsterdam: Vrije Universiteit, LHCb collaboration (2013).

[6] E. Salvati, Open Access Dissertations p. 201 (2010).

[7] C. Caso, P. D. Group, et al., *Eur. Phys. J. C* (1998).

[8] D. Decamp et al. (ALEPH Collaboration), Phys. Lett. **B231**, 519 (1989).

[9] D. Decamp et al. (ALEPH Collaboration), Phys. Lett. **B235**, 399 (1990).

[10] M. Fukugita and T. Yanagida, Phys. Lett. **B174**, 45 (1986).

[11] L. Bergström, Rep. Progr. Phys. **63**, 793 (2000).

[12] Y. Fukuda, T. Hayakawa, E. Ichihara, et al., Phys. Rev. Lett. **81**, 1562 (1998).

[13] F. Lehner, Ph.D. thesis, Universitat Zurich, $D\phi$ collaboration (2005).

[14] S. L. Glashow, J. Iliopoulos, and L. Maiani, Phys. Rev. D **2**, 1285 (1970).

[15] L.-L. Chau and W.-Y. Keung, Phys. Rev. Lett. **53**, 1802 (1984).

[16] L. Wolfenstein, Phys. Rev. Lett. **51**, 1945 (1983).

[17] R. P. Bernhard, Ph.D. thesis, Universitat Zurich, $D\phi$ collaboration (2005).

[18] Y. Sato, Ph.D. thesis, Tohoku University, Belle collaboration (2013).

[19] G. Buchalla, A. J. Buras, and M. E. Lautenbacher, Rev. of Mod. Phys. **68**, 1125 (1996).

[20] A. J. Buras, in *Quantum Field Theory* (Springer, 2000), pp. 65–85.

[21] A. J. Buras and R. Fleischer, arXiv: hep-ph/9704376 (1997).

[22] A. J. Buras, arXiv: hep-ph/9806471 (1998).

[23] A. J. Buras, Nucl. Instrum. Meth. Phys. Res., Sect. A **368**, 1 (1995).

[24] M. E. Peskin and D. V. Schroeder, *An introduction to quantum field theory* (Westview, 1995).

[25] T. M. Pulliam, BABAR analysis document **670** (2002).

[26] A. Ali, G. Hiller, L. T. Handoko, and T. Morozumi, Phys. Rev. D **55**, 4105 (1997).

[27] M. Neubert, arXiv: hep-ph/9702375 (1997).

[28] W. Altmannshofer and D. M. Straub, JHEP **8**, 1 (2012).

[29] W. Altmannshofer, P. Paradisi, and D. M. Straub, JHEP **4**, 1 (2012).

[30] S. W. Bosch and G. Buchalla, JHEP **08**, 054 (2002).

[31] A. Ali, B. D. Pecjak, and C. Greub, Eur. Phys. J. C **55**, 577 (2008).

[32] P. Ball, G. W. Jones, and R. Zwicky, Phys. Rev. D **75**, 054004 (2007).

[33] J. Wicht, I. Adachi, H. Aihara, et al. (Belle Collaboration), Phys. Rev. Lett. **100**, 121801 (2008).

[34] Y. Amhis, S. Banerjee, R. Bernhard, et al., arXiv:1207.1158 (2012).

[35] R. Aaij et al. (LHCb Collaboration), Nucl. Phys. **B867**, 1 (2013), `1209.0313`.

[36] A. Ali and A. Y. Parkhomenko, Eur. Phys. J. C **23**, 89 (2002).

[37] M. Alam, I. Kim, Z. Ling, et al. (CLEO Collaboration), Phys. Rev. Lett. **74**, 2885 (1995).

[38] M. Misiak, H. Asatrian, K. Bieri, et al., Phys. Rev. Lett. **98**, 022002 (2007).

[39] M. Misiak and M. Steinhauser, Nucl. Phys. **B764**, 62 (2007).

[40] A. Gemintern, S. Bar-Shalom, and G. Eilam, Phys. Rev. D **70**, 035008 (2004).

[41] P. Colangelo, F. De Fazio, R. Ferrandes, and T. Pham, Phys. Rev. D **77**, 055019 (2008).

[42] L. Reina, G. Ricciardi, and A. Soni, Phys. Rev. D **56**, 5805 (1997).

[43] R. Mohanta and A. Giri, Phys. Rev. D **85**, 014008 (2012).

[44] A. Gemintern, S. Bar-Shalom, G. Eilam, and F. Krauss, Phys. Rev. D **67**, 115012 (2003).

[45] J. Brodzicka, T. Browder, P. Chang, et al., Prog. Theo. Expt. Phys. **1**, 04D001 (2012).

[46] URL `http://www.lns.cornell.edu/public/lab-info/upsilon.html`.

[47] M. Kobayashi and T. Maskawa, Prog. Theo. Phys. **49**, 652 (1973).

[48] S. Herb, D. Hom, L. Lederman, et al., Phys. Rev. Lett. **39**, 252 (1977).

[49] URL `http://history.fnal.gov/jyoh_docs/e288_internal_notes.html`.

[50] B. Barish, M. Chadha, S. Chan, et al. (CLEO Collaboration), Phys. Rev. Lett. **76**, 1570 (1996).

[51] D. Besson, J. Green, R. Namjoshi, et al. (CUSB Collaboration), Phys. Rev. Lett. **54**, 381 (1985).

[52] M. Artuso, C. Boulahouache, S. Blusk, et al. (CLEO Collaboration), Phys. Rev. Lett. **95**, 261801 (2005).

[53] A. Drutskoy, K. Abe, I. Adachi, et al. (Belle Collaboration), Phys. Rev. Lett. **98**, 052001 (2007. This result is obtained by Belle using 121.4 fb^{-1} of $\Upsilon(5S)$ data and the method described in this paper.).

[54] S. Esen, A. Schwartz, H. Aihara, et al. (Belle Collaboration), Phys. Rev. D **87**, 031101 (2013).

[55] R. Louvot, J. Wicht, O. Schneider, et al. (Belle Collaboration), Phys. Rev. Lett. **102**, 021801 (2009.This result is obtained by Belle using 121.4 fb^{-1} of $\Upsilon(5S)$ data and the method described in this paper.).

[56] S. Kurokawa and E. Kikutani, Nucl. Instrum. Meth. Phys. Res., Sect. A **499**, 1 (2003).

[57] Y. Kimura, in *11th International Conference on High-Energy Accelerators* (Springer, 1980), pp. 144–155.

[58] T. Abe, K. Akai, M. Akemoto, et al., in *Part. Accl. Conf., 2007. PAC. IEEE* (IEEE, 2007), pp. 27–31.

[59] A. Abashian, K. Gotow, N. Morgan, et al., Nucl. Instrum. Meth. Phys. Res., Sect. A **479**, 117 (2002).

[60] Z. Natkaniec, H. Aihara, Y. Asano, et al., Nucl. Instrum. Meth. Phys. Res., Sect. A **560**, 1 (2006).

[61] Y. Ohnishi et al., Belle Note **148**, 1996 (1996).

[62] H. Hirano, M. Akatsu, Y. Fujita, et al., Nucl. Instrum. Meth. Phys. Res., Sect. A **455**, 294 (2000).

[63] T. Iijima, I. Adachi, R. Enomoto, et al., Nucl. Instrum. Meth. Phys. Res., Sect. A **453**, 321 (2000).

[64] H. Kichimi, Y. Yoshimura, T. Browder, et al., Nucl. Instrum. Meth. Phys. Res., Sect. A **453**, 315 (2000).

[65] K. Miyabayashi, Nucl. Instrum. Meth. Phys. Res., Sect. A **494**, 298 (2002).

[66] R. Akhmetshin, M. Wang, R. Guo, et al., Nucl. Instrum. Meth. Phys. Res., Sect. A **455**, 324 (2000).

[67] M. Yamaga, A. Abashian, K. Abe, et al., Nucl. Instrum. Meth. Phys. Res., Sect. A **456**, 109 (2000).

[68] A. Abashian, K. Abe, K. Abe, et al., Nucl. Instrum. Meth. Phys. Res., Sect. A **449**, 112 (2000).

[69] Y. Ushiroda, A. Mohapatra, H. Sakamoto, et al., Nucl. Instrum. Meth. Phys. Res., Sect. A **438**, 460 (1999).

[70] T. Ziegler, R. Abe, T. Abe, et al., Nucl. Sc., IEEE Trans. **51**, 1852 (2004).

[71] S. Nagayama, *Panther Users guide, version 3.0* (1997).

[72] Y. Ohnishi et al., *Panther - User's manual, reference manual and primer*, Belle Notes **130**, **131** and **132**.

[73] H. Ozaki, *Mini - DST tables v0.0*, Belle Note **146**.

[74] B. Casey, *Hadron B*, Belle Note **390**.

[75] J. R. Klein and A. Roodman, Annu. Rev. Nucl. Part. Sci. **55**, 141 (2005).

[76] P. Harrison, Journal of Phys.-Bristol-G Nucl. And Part. Phys. **28**, 2679 (2002).

[77] D. J. Lange, Nucl. Instrum. Meth. Phys. Res., Sect. A **462**, 152 (2001).

[78] S. Agostinelli, J. Allison, K. Amako, et al., Nucl. Instrum. Meth. Phys. Res., Sect. A **506**, 250 (2003).

[79] R. Brun, R. Hagelberg, M. Hansroul, and J. Lassalle, CERN Rep. CERN-DD-78-2 (1978).

[80] R. Brun, F. Bruyant, and M. Marie, Appl. Software Group, CND.-1994 (1995).

[81] K. Hanagaki, H. Kakuno, H. Ikeda, et al., Nucl. Instrum. Meth. Phys. Res., Sect. A **485**, 490 (2002).

[82] P. Koppenburg, *An improved* π^0 *and* η *veto*, Belle Note **665**.

[83] S. Villa, *Search for the decay* $B^0 \to \gamma\gamma$, Belle Note **831**.

[84] S. Villa, *Search for the* $B^0 \to \gamma\gamma$ *decay in the presence of off-time QED background*, Belle Note **811**.

[85] G. C. Fox and S. Wolfram, Phys. Rev. Lett. **41**, 1581 (1978).

[86] L. I. Kuncheva, *Combining pattern classifiers: methods and algorithms* (John Wiley & Sons, 2004).

[87] *The NeuroBayes User's Guide, version April 6, 2010.*

[88] C. M. Bishop et al., *Neural networks for pattern recognition* (Clarendon press Oxford, 1995).

[89] M. Feindt and U. Kerzel, Nucl. Instrum. Meth. Phys. Res., Sect. A **559**, 190 (2006).

[90] A. Höcker, P. Speckmayer, J. Stelzer, F. Tegenfeldt, H. Voss, and K. Voss, arXiv: 0703039 (2007).

[91] M. Prim, Ph.D. thesis, Karlsruher Institut Für Technologie, Belle collaboration (2010).

[92] R. J. Barlow, *Statistics: a guide to the use of statistical methods in the physical sciences*, vol. 29 (John Wiley & Sons, 1989).

[93] R. J. Barlow, R. Cahn, G. Cowan, et al., BABAR analysis document **318** (2002).

[94] W. R. Leo, *Techniques for nuclear and particle physics experiments: a how-to approach* (Springer, 1994).

[95] W. Verkerke and D. Kirkby, *RooFit Users Manual v2. 91*, Document version (2008).

[96] B. John, C.-H. Cheng, U. E. Ral, et al., BABAR analysis document **18** (2001).

[97] F. James and M. Roos, Comp. Phys. Comm. **10**, 343 (1975).

[98] F. James and M. Winkler, *Minuit users guide*, CERN (2004).

[99] F. James et al., Function Minimization and Error Analysis, Version **94** (1994).

[100] A. Lazzaro and L. Moneta, in *Journal of Phys.: Conf. Series* (IOP Publishing, 2010), vol. 219, p. 042044.

[101] S. Esen, *Branching fraction measurement of* B_s^0 *decays to* $D_s^{(*)+}D_s^{(*)-}$ *with 121.4* fb^{-1}, Belle Note **1203**.

[102] S. Esen (Belle Collaboration), PoS **ICHEP2010**, 197 (2010), `1107.0298`.

[103] H. Kim, *Study of high energy photon detection efficiency using radiative Bhabha*, Belle Note **499**.

[104] B. Bhuyan, *High* $\mathrm{P_T}$ *Tracking Efficiency Using Partially Reconstructed* D^* *Decays*, Belle Note **1165**.

[105] H. Albrecht, R. Gläser, G. Harder, et al. (ARGUS Collaboration), Phys. Lett. **B241**, 278 (1990).